Master Thesis

Measurement and Geant4 simulation of Cherenkov radiation using an electron monochromator

Masterarbeit

zur Erlangung des akademischen Grades Master of Science (M.Sc)

eingereicht bei der Naturwissenschaftlich-Technischen Fakultät

Naturwissenschaftlich-Technische Fakultät

der Universität Siegen

Author:	Daniel Berker 1436314
Date of submission:	03.09.2025
1st Supervisor: 2nd Supervisor:	Prof. Dr. Ivor Fleck Prof. Dr. Markus Risse

Universität Siegen

HEP Experimental High Energy Physics

CPPS Center for Particle Physics Siegen

Version of October 23, 2025

Diese Arbeit wurde am 3. September 2025 als Masterarbeit an der Naturwissenschaftlich-Technischen Fakultät der Universität Siegen eingereicht und angenommen. Bei dieser vorliegenden Version handelt es sich um eine leicht abgeänderte Version. Der wissenschafltiche Inhalt der Arbeit ist unverändert.

This thesis was submitted and accepted as master thesis at the School of Science and Technology of the University of Siegen on 3rd September 2025. This version includes some small changes, but the scientific content is unchanged.

Abstract

The utilization of radioactive tracers requires the proper detection of their emitted gamma radiation. This is limited to energies below 1 MeV due to the current detection techniques. The Cherenkov-Compton camera under construction at the University of Siegen offers a novel approach to detect gamma photons in the low MeV range. The photon is reconstructed based on the created Compton electron and the scattered photon. For a successful reconstruction, a determination of the electron is unavoidable. These electrons are high energetic.
This thesis presents a first proof of principle of the detection of high-energy electrons with energies around 1 MeV and above using an electron monochromator. An electron monochromator is calibrated and prepared for measuring electrons emitted by a Strontium-90 source, which simulates Compton electrons. Furthermore, a Geant4 model is motivated and tuned to validate the experiment.

Contents

1. Introduction

Nowadays, radioactivity plays an important role in various fields, such as medical diagnostics or biological research. Here, a commonly used method is the injection of radioactive tracers, which, depending on the tracers, are absorbed by specific cells. This allows the investigation of a certain tissue or dynamic processes. These radioactive tracers emit gamma photons, which can then be detected with gamma cameras. However, current detection and imaging techniques are inefficient for gamma energies above 1 MeV, thereby limiting the use of isotopes that emit gamma radiation above this energy. One promising idea is the Compton camera, which aims to measure photon energies in the low MeV range after undergoing a Compton scattering. This concept requires the precise determination of the resulting Compton electron. This thesis aims to test the concept of an electron monochromator to investigate high-energy electrons with energies above 1 MeV.
Chapter 2 provides the theoretical background that is necessary in the scope of this thesis, mainly focusing on the interactions of particles in matter. It also includes a list of sources, which are used in this work. Afterwards, a brief overview of the simulation toolkit Geant4 is given in Chapter 3. In Chapter 4, the working principle of the Compton camera is explained, and also the novel approach of the Cherenkov-Compton camera at the University of Siegen. It is followed by the introduction of the electron monochromator in Chapter 5. Besides an explanation of the working principle, it also includes the experimental setup as well as the basic setup for the Geant4 simulations. The following Chapter 6 is about the theoretical prediction of electron trajectories inside the electron monochromator using numerical calculations.
The following chapters are about experimental preparations for the electron monochromator. Chapter 7 addresses the preparations for the electron monochromator experiment. It consists of simulations about the expected energy resolution. It is followed by the experimental detector calibration for the electron monochromator, described in Chapter 8. This calibration will be important to resolve the energies of electron after their separation. This is also required for the investigation of the background in Chapter 9.
The last few chapters discuss the tuning of the Geant4 simulations using experimental observations. At first, the Geant4 setup is modified in Chapter 10, before comparing simulations with experimental data in Chapter 11. Based on these results, the magnetic field is investigated more in detail in Chapter 12.
At last, a conclusive summary of the most important results, as well as an outlook on the next steps, are given in Chapter 13.

2. Theoretical background

This chapter provides a brief overview of important physical concepts necessary for the experiments in this thesis.

2.1. Interactions of charged particles with matter

2.1.1. Ionisation

While traversing a material, any charged particle interacts with the material's atoms, causing an energy transfer. The atoms will either be excited or ionized. These interactions are stochastic processes; the resulting mean energy loss (normalized by the material's density ρ) of these interactions can be described by the Bethe-Bloch equation [KW20]

$$-\left\langle \frac{\mathrm{d}E}{\mathrm{d}x} \right\rangle = K \frac{Z}{A} \frac{z^2}{\beta^2} \left(\frac{1}{2} \ln \frac{2m_e c^2 \beta^2 \gamma^2 T_{\max}}{I^2} - \beta^2 - \frac{\delta(\beta\gamma)}{2} - \frac{C(\beta\gamma, I)}{Z} \right) \tag{2.1}$$

with $\mathrm{K} = 0.307\,\mathrm{MeVcm}^2/\mathrm{mol}$, which depends on both the incident particle's (β, γ and charge number z) and the target material's (ρ, Z, A and mean excitation energy I) properties. $\delta(\beta\gamma)$ is a high-energy correction due to the density effect, $\frac{C(\beta\gamma, I)}{Z}$ denotes a 'shell correction' for low energetic particles, while $T_{\max}$ is the maximum energy transfer of the particle with mass M onto a shell electron in a single collision given by [KW20],

$$T_{\max} = \frac{2m_e c^2 \beta^2 \gamma^2}{1 + 2\gamma \frac{m_e}{M} + \frac{m_e^2}{M^2}} \,. \tag{2.2}$$

A scheme of the ionisation energy loss as a function of the particle's velocity is depicted in Figure 2.1.1. The energy loss for velocities below the minimum ionisation at $\beta\gamma \approx 3 - 4$ behaves like $1/\beta^2$. The proportionality $\frac{\mathrm{d}E}{\mathrm{d}x} \approx \ln \gamma$ above the minimum leads to a plateau at high energies. If the energy loss is at a minimum, the particle is called a 'minimum ionizing particle'. This state depends on the particle's mass and requires higher kinetic energies for heavier particles. This is represented in Figure 2.1.2.

Unlike hadrons and heavier leptons, the Bethe-Bloch equation in Eq. 2.1 cannot accurately describe the energy losses due to ionization for electrons and positrons. On the one hand, bremsstrahlung already becomes important for low energies due to the low masses of the particles involved. On the other hand, interactions between an electron and a shell electron lead to additional interference effects, since they can mix up. Furthermore, the spin configurations also need to be taken into account. [KW20]

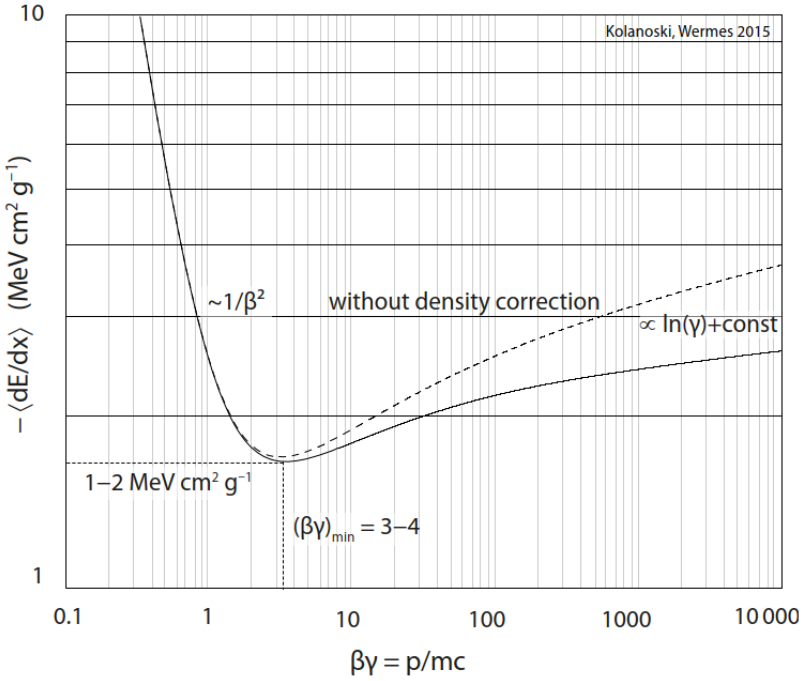

Figure 2.1.1.: Illustration of the ionisation energy loss of charged particles as a function of velocity [KW20].

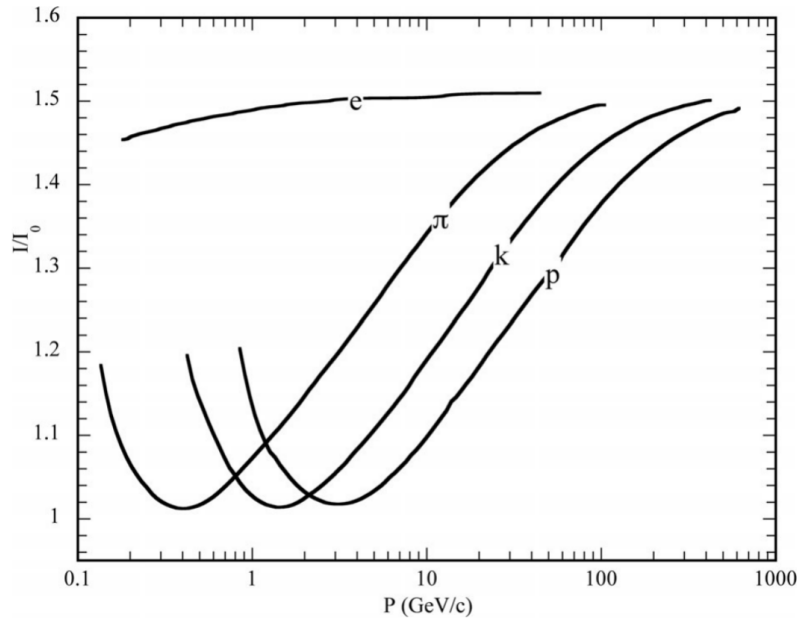

Figure 2.1.2.: Mean ionization loss for different particles as a function of the particle momentum [Sau14].

2.1.2. Bremsstrahlung

Bremsstrahlung refers to the emission of photons caused by the interaction of a fast charged particle with the Coulomb field of a nucleus. The resulting deceleration of the particle leads to an energy loss in the form of an emitted photon. Figure 2.1.3 shows a simple scheme of the bremsstrahlung, representing the bremsstrahlung's process as a

combination of a Rutherford scattering of a charged particle at a nucleus with atomic number Z and a photon emission. Here, the electron is assumed to keep its momentum direction. Introducing the radiation length X_0, solely based on the interacting material, the particle's remaining energy after a path length x due to bremsstrahlung is given by [KW20]

$$E(x) = E_0 \exp\left(-\frac{x}{X_0}\right) \ . \tag{2.3}$$

If $x = X_0$, the particle will loose $1/e \approx 63\,\%$ of its initial energy E_0.
There is an inverse proportionality between the energy loss and the incoming particle mass m_p [KW20]

$$-\frac{\mathrm{d}E}{\mathrm{d}x} \propto Z^2 \ \frac{E}{m_p^2} \ , \tag{2.4}$$

so that bremsstrahlung becomes dominant for light particles such as electrons, and for larger nuclei. The energy E_c, at which radiation losses due to bremsstrahlung are equal to the energy loss due to ionization losses, is called the 'critical energy'. This energy can be estimated with

$$E_c \approx \frac{610\,\mathrm{MeV}}{Z + 1.24} \tag{2.5}$$

for solid materials and liquids, and

$$E_c \approx \frac{710\,\mathrm{MeV}}{Z + 0.92} \tag{2.6}$$

for gases [KW20]. This approximation only depends on the state of aggregation and the atomic number Z. If a charged particle traverses aluminum ($Z = 13$), the critical energy is $E \approx 43\,\mathrm{MeV}$. Above E_c, bremsstrahlung needs to be considered. This work examines electrons with energies below $2.5\,\mathrm{MeV}$ that strike light materials such as scintillators and aluminum; therefore, bremsstrahlung does not contribute significantly, since the critical energy is not exceeded.

2.1.3. Multiple Coulomb scattering

Besides the deceleration and creation of bremsstrahlung, charged particles also undergo multiple scattering processes in the Coulomb field of nuclei. The difference is that no radiation is emitted, but the electron is scattered at a tiny angle θ_i for each scattering. Multiple scattering in a row leads to a significant change in the particle's path. If a particle undergoes multiple scattering by traversing a material with thickness x, the distribution of scattering angle is Gaussian-like. The corresponding deviation angle θ_ms then can be calculated by the 'Highland formula' [KW20]

$$\theta_\mathrm{ms}(x) = \frac{13.6\,\mathrm{MeV/c}}{p\beta} z \frac{x}{X_0}\left(1 + 0.0038 \ \ln\frac{x}{X_0}\right) \ . \tag{2.7}$$

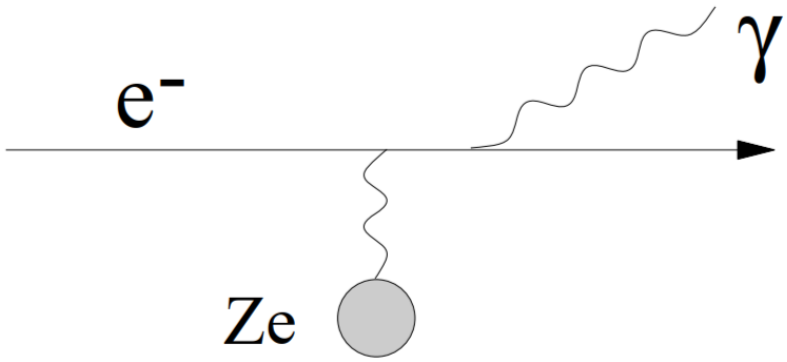

Figure 2.1.3.: Illustration of bremsstrahlung. A photon is emitted after the interaction of a charged particle with the Coulomb field of a nucleus with atomic number Z [KW20].

2.1.4. Cherenkov effect

The Cherenkov effect describes the phenomenon of light emitted after a charged particle with velocity $v = \beta c$ traverses a medium with refractive index n faster than the phase velocity of light in that medium,

$$v > \frac{c_0}{n} \ , \tag{2.8}$$

where c is the vacuum speed of light. Furthermore, it is required that the size of the medium is larger than the wavelength of the corresponding Cherenkov radiation [KW20].
In contrast to low velocities $v < \frac{c}{n}$, where a symmetrical polarization happens, the particle causes an unsymmetrical polarization of the surrounding atoms along its trajectory (Figure 2.1.4). Those atomic dipoles then superimpose, leading to a non-zero dipole moment and thus, photon emissions at an angle θ_{Ch}, given by [KW20]

$$\cos\theta_{\mathrm{Ch}} = \frac{1}{\beta n} \ , \tag{2.9}$$

where $\beta = \frac{v}{c}$ is the normalized velocity. The maximal Cherenkov angle

$$\theta_{\mathrm{Ch}}^{\mathrm{max}} = \frac{1}{n} \tag{2.10}$$

is achieved for ultra-relativistic particles and is purely medium-dependent. On the other side, the lowest possible emission angle $\theta_{\mathrm{Ch}} = 0° \iff \cos\theta_{\mathrm{Ch}} = 1$ corresponds to the Cherenkov photons produced by particles having the minimal velocity

$$\beta_{\mathrm{th}} = \frac{1}{n} \ . \tag{2.11}$$

Using the relation with the Lorentz factor γ, this leads to the threshold energy

$$\frac{E_{\mathrm{th}}}{m\ c^2} = \gamma_{\mathrm{th}} = \frac{1}{\sqrt{1-\beta_{\mathrm{th}}^2}} = \frac{1}{\sqrt{1-\frac{1}{n^2}}} = \frac{n}{\sqrt{n^2-1}} \ , \tag{2.12}$$

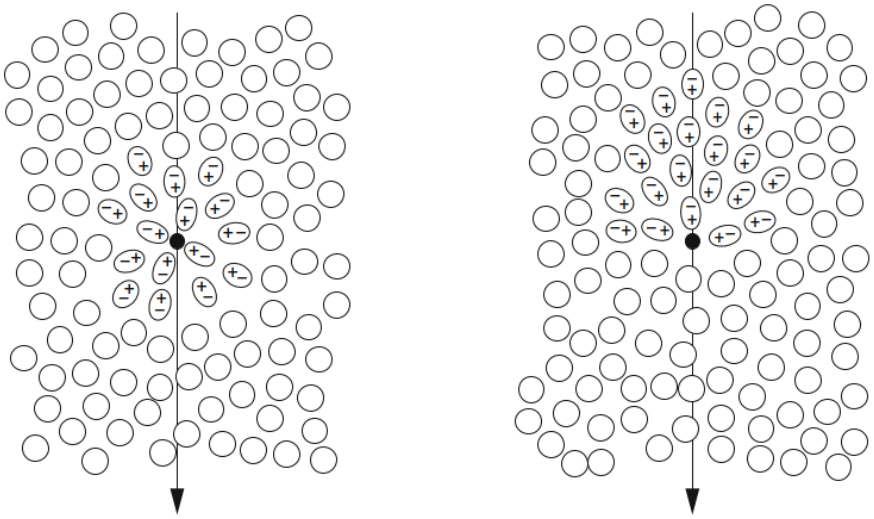

Figure 2.1.4.: Creation of atomic dipoles in a medium with refractive index n by a traversing charged particle with velocity v. Left: symmetrical arrangement of atomic dipoles for $v < \frac{c_0}{n}$. Right: unsymmetrical arrangement of atomic dipoles for $v > \frac{c_0}{n}$ [KW20].

which also only depends on n.

The intensity of the Cherenkov radiation per frequency interval and path length is given by the Frank-Tamm formula [KW20]

$$\frac{d^2E}{d\omega dx} = \frac{z^2e^2}{4\pi\varepsilon_0 c^2}\ \omega\ \left(1\ -\ \frac{1}{\beta^2 n^2(\omega)}\right) = \frac{z^2e^2}{4\pi\varepsilon_0 c^2}\ \omega\ \sin^2\theta_c(\omega)\ . \tag{2.13}$$

Dividing Eq. 2.13 by the photon energy and converting the frequency into wavelength leads to the number of produced Cherenkov photons per path per wavelength interval [KW20]

$$\frac{\mathrm{d}^2N}{\mathrm{d}\lambda\mathrm{d}x} = \frac{2\pi z^2\alpha}{\lambda^2}\ \sin^2\theta_c(\lambda)\left(1 - \frac{1}{\beta^2 n^2(\lambda)}\right) \tag{2.14}$$

with the fine structure constant α. The majority of the produced Cherenkov photons are emitted in the UV range (Figure 2.1.5). Cherenkov photons cannot have wavelengths below $100\,\mathrm{nm} - 150\,\mathrm{nm}$ due to anomalous dispersion effects, in which $n^2 < \frac{1}{\beta^2}$ [KW20].

2.2. Photon interactions with matter

2.2.1. Photoelectric effect

The photoelectric effect is the dominant effect for low-energy photons and refers to the process

$$\gamma + \mathrm{atom} \rightarrow (atom)^* + e^-\ , \tag{2.15}$$

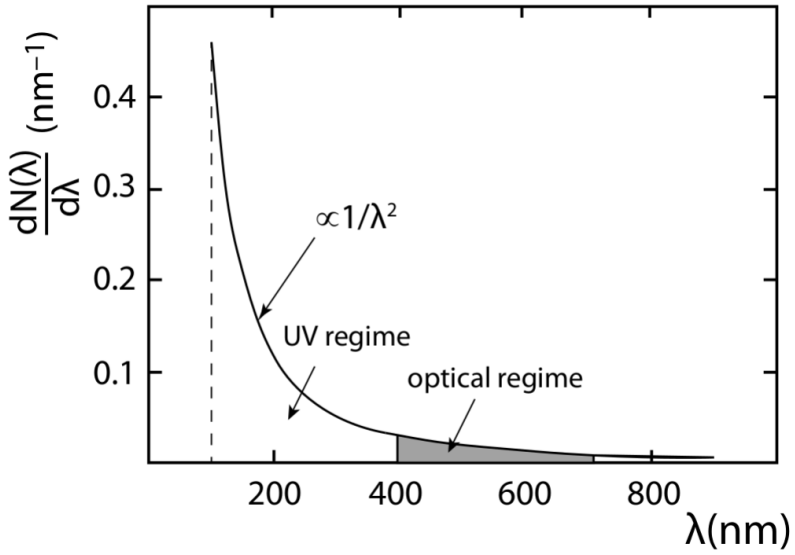

Figure 2.1.5.: Cherenkov photon spectrum as a function of the wavelength. The dotted line marks the lower wavelength limit due to anomalous dispersion [KW20].

in which a photon is completely absorbed by a shell electron. This effect only occurs if the binding energy E_B of the electron is lower than the photon energy E_γ, and results in an emission of a shell electron with kinetic energy

$$T_e = E_\gamma - E_\mathrm{B} \tag{2.16}$$

and an ionized atom [KW20]. The resulting recoil energy from the electron emission is absorbed by the atomic nucleus. Although the photoelectric effect can appear in all electron shells, the majority (about 80 %) takes place in the K-shell. This is because of its close distance to the nucleus [GS08].
If an atom consists of multiple electron shells, the photoelectric effect can further initiate a secondary process. The hole created in the K shell can be filled by an electron from the neighboring L shell. In this case, the energy difference results in the emission of a photon. If the photon energy is high enough, its energy can be transferred to an electron of the M shell or above, and this electron leaves the shell as an Auger electron. [GS08]

2.2.2. Compton effect

The Compton effect denotes the scattering of a photon by an electron. One has to distinguish between coherent and incoherent scattering. Coherent scattering occurs if the target electron is a shell electron whose binding energy E_B is not significantly lower than the photon energy E_γ. In this case, the photon loses a negligible fraction of its energy, absorbed by the atomic nucleus, and only changes its direction [KW20]. The incoherent Compton scattering instead occurs either for free electrons or shell electrons with $E_\mathrm{B} \ll E_\gamma$, in which the photon transfers a part of its energy to the electron. A shell electron will leave the electron shell.
The kinematics of an incoherent Compton effect is depicted in Figure 2.2.1. It can be assumed as a quasi-elastically scattering process while the electron is at rest. After the scattering, one obtains a scattered photon with energy E'_γ, while the energy of the

electron is E'_e. Using energy conservation

$$E_\gamma + m_e c^2 = E'_\gamma + E'_e \tag{2.17}$$

and momentum conservation, the scattered photon's energy can be calculated by [KW20]

$$E'_\gamma = \frac{E\gamma}{1 + \frac{E\gamma}{m_e c^2}(1 - \cos\theta_\gamma)} , \tag{2.18}$$

or, rearranged for the Compton angle,

$$\cos\theta_\gamma = 1 - m_e c^2 \left(\frac{1}{E'_\gamma} - \frac{1}{E_\gamma}\right) \tag{2.19}$$

with the energy of the incident photon E_γ.

$$T = E_\gamma - E'_\gamma . \tag{2.20}$$

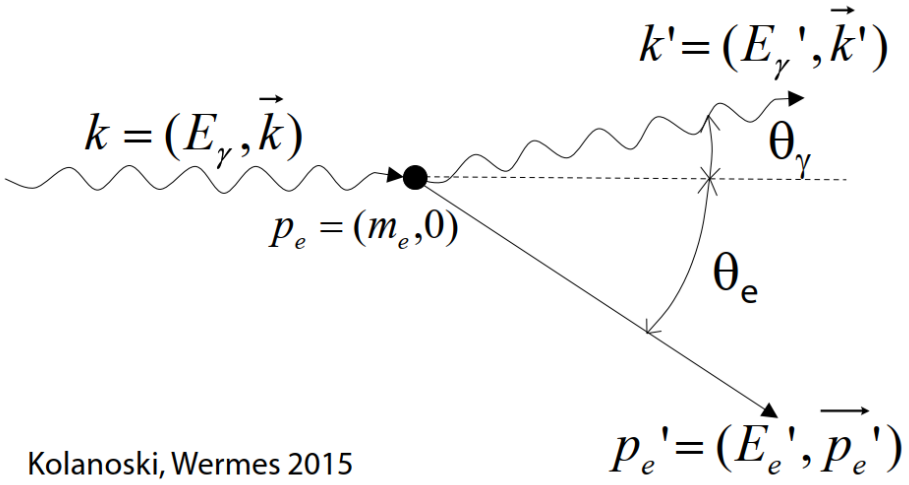

Figure 2.2.1.: Kinematics of an incoherent Compton process [KW20].

2.3. Radioactive decays

All nuclei long for being in the lowest energy state possible. If a nucleus can transform into a lower energy state, it will decay and emit energy as radiation, without requiring external energy. There are different decay processes possible:

α decay

The α decay denotes the splitting off of an α particle ($^4_2\mathrm{He}_2$):

$$^{\mathrm{A}}_{\mathrm{Z}}X_N \longrightarrow {}^{\mathrm{A-4}}_{\mathrm{Z-2}}Y_{\mathrm{N-2}} + {}^4_2\mathrm{He}_2 + \Delta E \tag{2.21}$$

The emitted alpha particle has a discrete energy spectrum.

β^+ and β^- decay

Both β decays are based on the weak force and create an isobaric isotope. While a β^+ decay converts a proton into a neutron, the β^- decay does it the other way around. Furthermore, due to charge conservation and lepton number conservation, an electron and an antielectron neutrino are produced in the β^- decay (positron and electron neutrino in the β^+ decay, respectively). The resulting nucleus conversions are

$$ {}^{\mathrm{A}}_{\mathrm{Z}}X_{\mathrm{N}} \xrightarrow{\beta^-} {}^{\mathrm{A}}_{\mathrm{Z+1}}Y_{\mathrm{N\text{-}1}} + e^- + \bar{\nu}_{\mathrm{e}} + \Delta E \text{ and} \tag{2.22} $$

$$ {}^{\mathrm{A}}_{\mathrm{Z}}X_{\mathrm{N}} \xrightarrow{\beta^+} {}^{\mathrm{A}}_{\mathrm{Z\text{-}1}}Y_{\mathrm{N+1}} + e^+ + \nu_{\mathrm{e}} + \Delta E. \tag{2.23} $$

β decays are referred to as three-body decays, since the final state consists of three particles, which will get a fraction of the released energy as kinetic energy. The beta particles (electron, positron) are therefore emitted in a continuous energy spectrum.

Electron capture

The electron capture (EC) denotes the process in which a shell electron is captured by its nucleus. A proton, in combination with that electron, is then converted into a neutron:

$$ {}^{\mathrm{A}}_{\mathrm{Z}}X_{\mathrm{N}} + e^- \longrightarrow {}^{\mathrm{A}}_{\mathrm{Z\text{-}1}}Y_{\mathrm{N+1}} + \nu_{\mathrm{e}} + \Delta E. \tag{2.24} $$

After the replacement of the created hole in the electron shell by an electron from an outer shell, a photon with a defined energy is emitted. Electron capture is a process that competes with β^+ decay.

γ radiation

After a radioactive decay, the nucleus can be in an excited state. It will emit a γ photon with a determined energy to enter its ground state.

2.3.1. Used sources

All used sources in the scope of this thesis and their corresponding activity are listed in Table 2.1. The activity is calculated by

$$ A(\Delta t) = A_0 \cdot 2^{-\frac{\Delta T}{T_{1/2}}} \tag{2.25} $$

with half-time $T_{1/2}$.

Bismuth-207

The isotope ^{207}Bi decays into ^{207}Pb dominantly via electron capture with a branching ratio BR(EC) = 99.962 %. Another decay channel is β^+-decay with BR(EC) = 0.038 %. The daughter nucleus is produced in different excited states, which decay either by emission of a photon or through internal conversion. The decay scheme of ^{207}Bi is shown in Figure 2.3.1. The most dominant decay channel is the excited state with $J^p = 13/2^+$, which emits a γ with an energy of 1063.656 keV. Alternatively, it can also create a conversion electron. In this case, a K-shell conversion electron has an energy of 975.651 keV, or a

Source	Initial activity A_0	Date of purchase	$T_{1/2}$ (a)	Activity 01.04.2025 (kBq)
Bismuth-207	37 kBq	21.01.2008	31.55	25.4
Caesium-137	370 kBq	01.07.2005	30.13	234.8
Cobalt-60	370 kBq	01.07.2005	5.27	27.5
Sodium-22	40.7 MBq	12.03.1998	2.60	29.9
Strontium-90	370 kBq	01.09.2018	28.81	315.8

Table 2.1.: Used sources and their activity. Activity is calculated in full days, initial activities are taken from [Sie].

1047.795 keV L-shell conversion electron. Further decay modes are the excited states $J^p = 5/2^-$ (lowest state with (BR = 8.9 %, decay dominated by the emission of an 569.698 keV photon) and $J^p = 7/2^-$, which decays in a 1770.228 keV photon. The most intense decays are listed in Table 2.2. In addition, atomic transitions can cause the emission of photons in the X-ray range. These transitions are not included in Table 2.2.

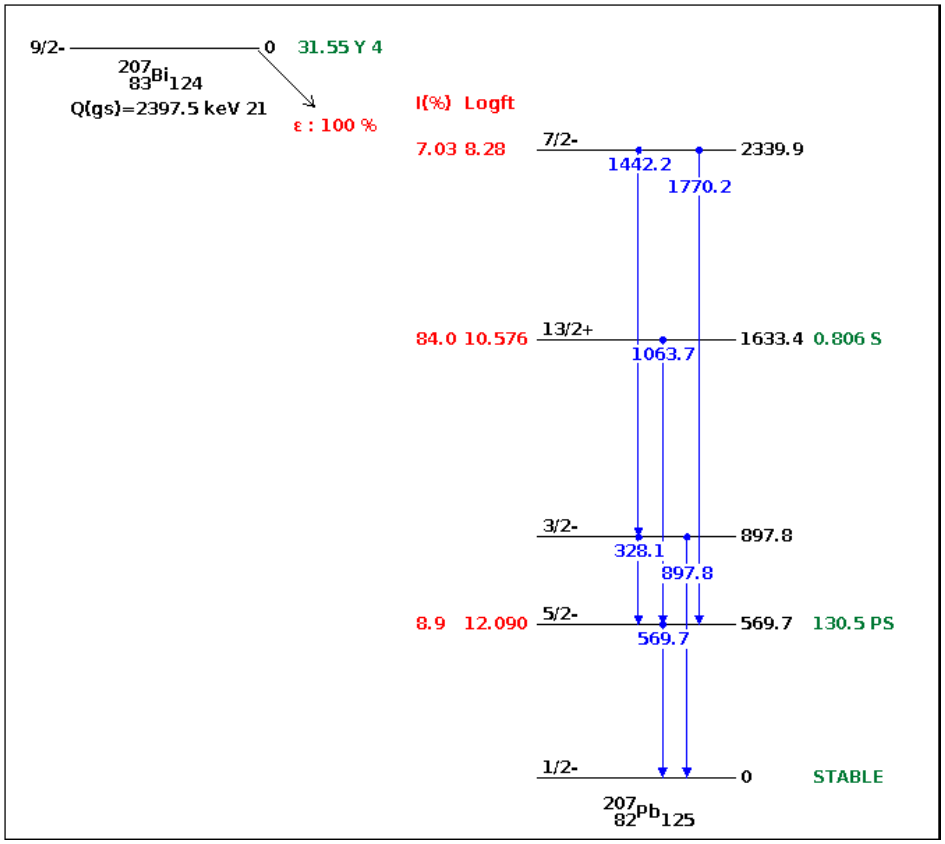

Figure 2.3.1.: Decay scheme of ^{207}Bi [KL11].

Caesium-137

The isotope ^{137}Cs decays into ^{137}Ba exclusively via β^--decay. The beta electrons have an main energy of 187.1 keV. The daughter nucleus ^{137}Ba is mainly created in the excited state $J^p = 11/2^-$ (BR = 94.7 %), which dominantly de-excites under emission of a 661.657 keV photon. Another de-excitation opportunity is the creation of conversion electrons, whereby the K-shell conversion electron has

Type	Energy (keV)	Intensity (%)
CE K	481.694	1.54
CE L	553.837	0.44
γ	569.698	97.75
CE K	975.651	7.08
CE L	1047.795	1.84
γ	1063.656	74.50
γ	1770.228	6.87

Table 2.2.: Most intense radiation of ^{207}Bi. X-rays are not listed here. Data taken from [KL11].

an energy of 624.216 keV. The decay scheme of ^{137}Cs is depicted in Figure 2.3.2 and an overview of the most intense radiations of the ^{137}Cs decay can be found in Table 2.3.

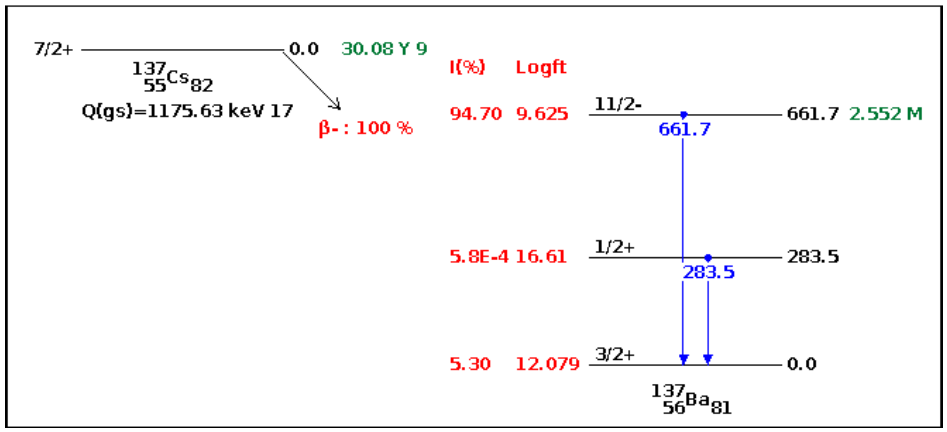

Figure 2.3.2.: Decay scheme of ^{137}Cs [BT07].

Type	Energy (keV)	Intensity (%)
β^-	$\bar{E} = 187.1$	100.00
γ	661.657	85.10
CE K	624.216	7.40

Table 2.3.: Most intense radiation of ^{137}Cs and its daughter nucleaus ^{137}Ba. X-rays are not listed here. Data taken from [BT07].

Cobalt-60

The isotope ^{60}Co decays into ^{60}Ni exclusively via β^--decay. The beta electrons have a main energy of 96.41 keV. The daughter nucleus ^{60}Ni is mainly created in the excited state $J^p = 4^+$ (BR = 99.88 %). The most dominant decay of the $J^p = 4^+$ state is the emission of a 1173.217 keV gamma and leads to the $J^p = 2^+$ state. In this excited state, a 1332.492 keV gamma is mainly emitted. Afterwards, ^{60}Ni is in the ground state. The decay scheme of ^{137}Cs is depicted in Figure 2.3.3 and an overview of the most intense radiations of the ^{137}Cs decay can be found in Table 2.4.

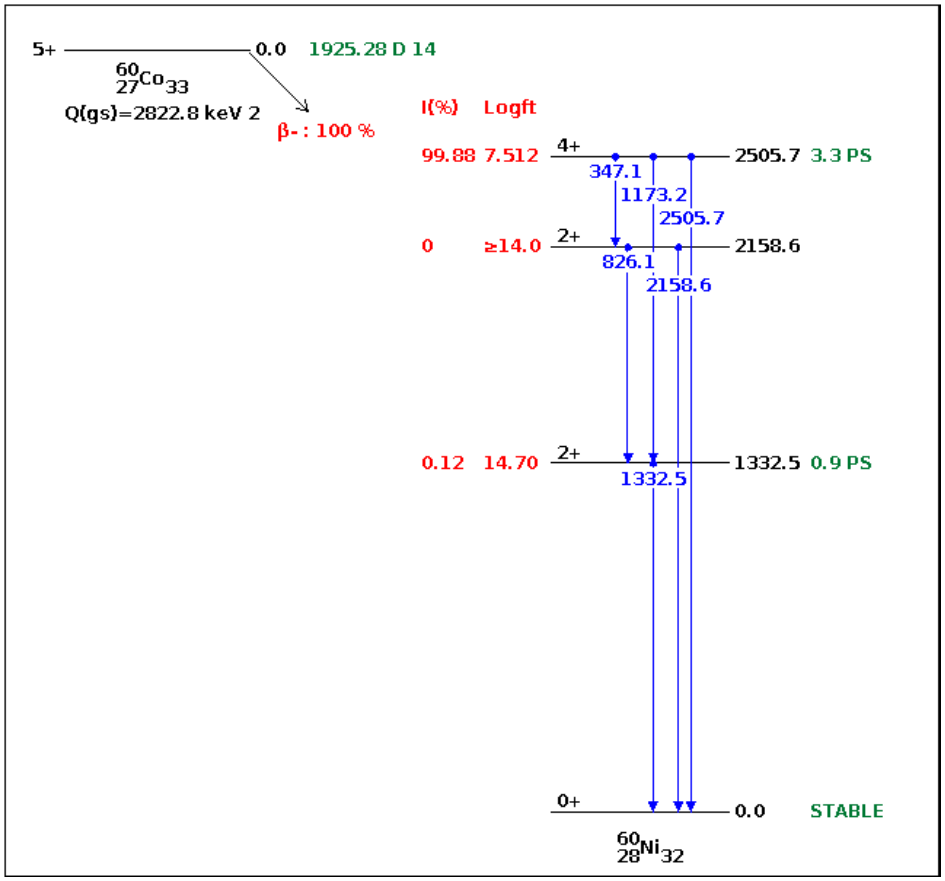

Figure 2.3.3.: Decay scheme of ^{60}Co [BT13].

Type	Energy (keV)	Intensity (%)
β^-	$\bar{E} = 96.41$	100.00
γ	1173.217	99.85
γ	1332.492	99.98

Table 2.4.: Important radiation of ^{60}Co. Data taken from [BT13].

Sodium-22

The isotope ^{22}Na decays into the stable isotope ^{22}Ne mainly via β^+-decay with a branching ratio BR = 89.96 %. The mean energy of the resulting positrons is 216.012 keV. Each positron leads to the production of two photons with an energy of 511 keV each due to electron-positron annihilation. The other 10.04 % decays via electron capture. In 99.94 % of all ^{22}Na decays, the daughter isotope ^{22}Ne is excited and de-excites to the ground state by emitting a 1274.537 keV photon. The decay scheme of ^{22}Na is depicted in Figure 2.3.4 and the important decays are listed in Table 2.5.

Strontium-90

The isotope ^{90}Sr is a beta emitter and decays into ^{90}Y exclusively via β^--decay. The beta electrons are distributed up to 545.9 keV and have a main energy of

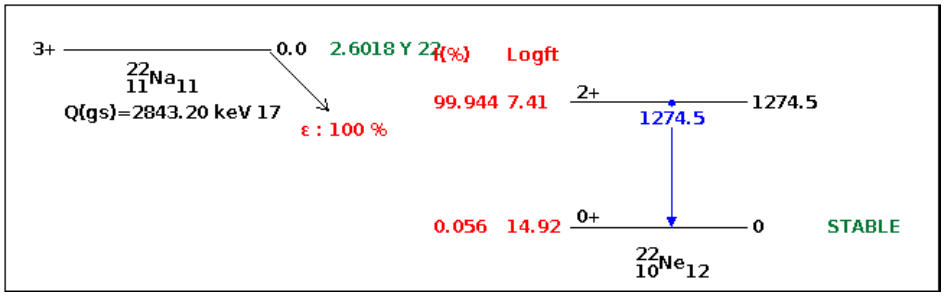

Figure 2.3.4.: Decay scheme of ^{22}Na [Sha15].

Type	Energy (keV)	Intensity (%)
β^+	$\bar{E} = 216.4$	89.96
γ	511	179.91
γ	1274.54	99.94

Table 2.5.: Important radiation of ^{22}Na. Data taken from [Sha15].

96.41 keV. The daughter nucleus ^{90}Y itself is also a beta emitter and decays to the stable isotope ^{90}Zr via β^--decay. The main of the beta particles of ^{90}Y have a main energy of 932.4 keV, but can reach above 2 MeV. The decay scheme of ^{90}Sr is depicted in Figure 2.3.5 and an the important decays of ^{90}Sr and its daughter nucleaus ^{90}Y are listed Table 2.6.

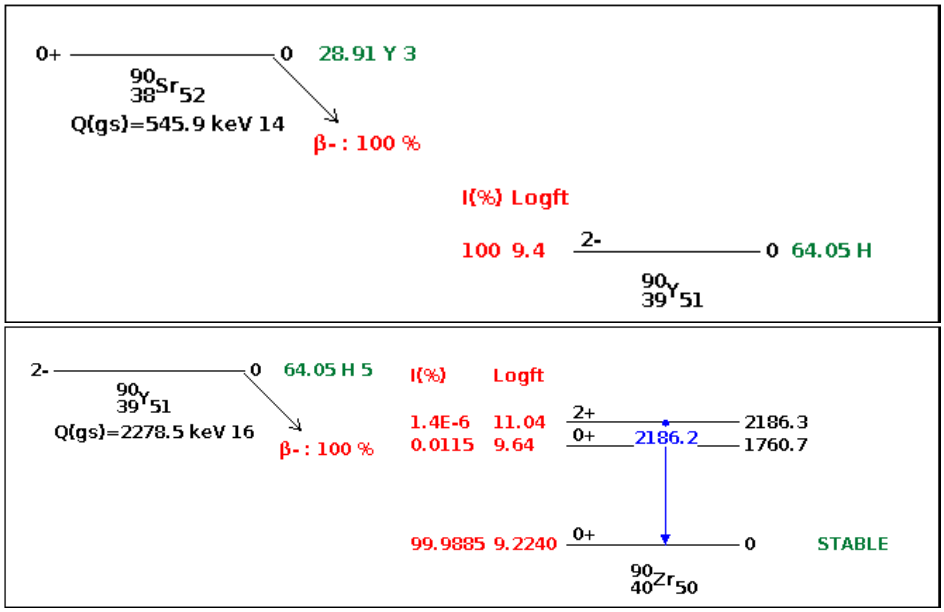

Figure 2.3.5.: Decay scheme of ^{90}Sr and ^{90}Y [BM20].

Type	Energy (keV)	Intensity (%)
β^-	$\bar{E} = 195.7$	100.00
β^-	$\bar{E} = 932.3$	100.00

Table 2.6.: Important radiation of ^{90}Sr and its daughter isotope ^{90}Y. Data taken from [BM20].

3. Geant4

This chapter gives a short overview of the simulation program Geant4 in general, which is used for the detector simulations. All given information is taken from the official Geant4 website [Gea] and the 'Book For Application Developers' [Gea25] (Geant4 manual). No explicit references are provided below, except for other sources.
Geant4 is a free, powerful simulation toolkit, based on C++, to simulate interactions of particles and radiation with matter. Formerly developed as the successor of Geant3 for high-energy physics experiments at CERN, it is nowadays an indispensable tool in detector simulations and is used in different fields, for example in nuclear physics or in medical physics for the investigation of medical applications. Geant4 provides a variety of abstract classes that can be overridden to create customized simulation files for different complexities. A simulation is started by executing the main file of the simulation.
The primary particles, initialized by the particle gun, are called events. Geant4 considers one particle after another, shown in Figure 3.0.1. A new event is only initialized after all previous particles, including secondary particles, have been deleted. A particle is deleted if its kinetic energy falls below the defined cut energy. The trajectory of a particle is updated in discrete steps, which connect two points, where either the particle undergoes a physical process or hits a volume boundary. The first point of a step (pre-step point) contains the particle's quantities before the physical interaction, while the end point (post-step point) contains the updated information. The production of secondary particles is provided in the post-step point. The totality of all events is called a run, which corresponds to one simulation.

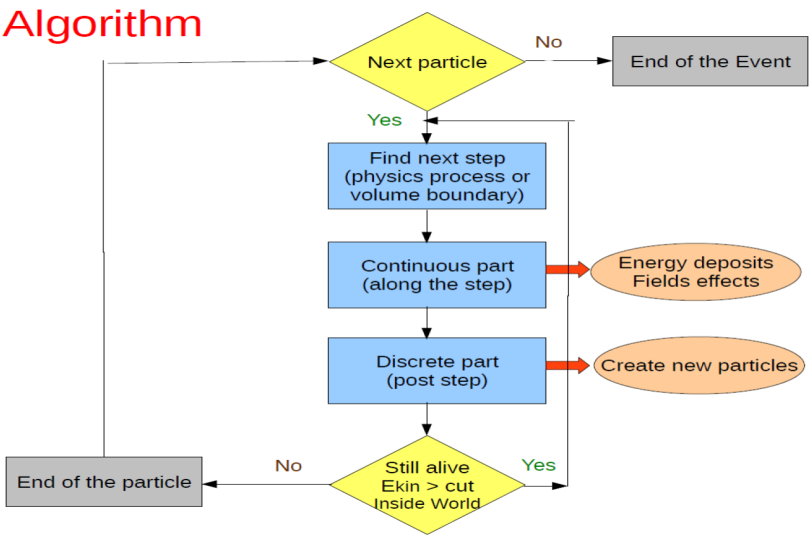

Figure 3.0.1.: Scheme of the event algorithm. Events are generated one after another if all particles, including secondary particles, are deleted [PR16].

The structure of Geant4 is object-oriented; hence, a simulation typically consists of

multiple files, whose compilation is organized by CMake. Besides the main file, which is the executable file of a simulation, each simulation must include the following four classes:

G4RunManager
: The G4RunManager class defines the run manager, which coordinates the overall simulation. To do so, it requires information about the number and type of produced particles. All other managers exist only after the run manager is instantiated; hence, the explicit instantiation of the run manager in the main file is the very first action of each simulation. The run manager further initializes the detector geometry and the physics list.

Action initilisation
: The ActionInitialization class ensures smooth simulation runs. This class is in charge of the particle gun, which produces the initial particles. It also instantiates all kinds of action managers, such as 'EventManager' and 'RunManager'.

Construction class
: The Construction class is a customized class that contains information about the geometry of the setup. Each single volume is defined by a geometrical shape and a material. The material itself has to be built up, and its most important ability is the density, since the density influences the interaction probability with particles. For optical interactions, such as Cherenkov radiation, optical properties have to be defined specifically. On the other hand, the Construction class includes a function called 'ConstructSDandField()', in which selected volumes can be defined as a sensitive detector for investigations and particle tracking. This function also provides a declaration of magnetic fields.

PhysicsList class
: The customized PhysicsList class provides the list of physical interactions. Only interactions, whether hadronic or electromagnetic interactions that are listed in this class are taken into account. The default list 'EM Opt0' already provides multiple electromagnetic interactions. It is also possible to create your own physics lists; however, there are many free parameters that one has to specify: interaction type, particle type, energy range etc. In case of optical interactions, such as Cherenkov radiation, one has to ensure that the corresponding volume has defined optical properties.

4. Compton camera

Radioactive isotopes used for clinical treatments emit gamma radiation in the range from hundreds of keV up to a few MeV. For energies below $\approx 600\,\text{keV}$, photons can be resolved using single-photon emission computed tomography (SPECT) or positron emission tomography (PET). SPECT is a collimator-based technique, using scintillators to create scintillation light, which is then registered by multiple photo detectors, i.e. PMTs. The mechanical collimators are necessary to ensure that only photons parallel to the openings (within an angular spread) can strike the scintillator. Its spatial resolution is limited by the photon energy, since high-energy photons traverse the collimator material easily and create additional scintillation light. On the other hand, the photons in PET have a defined energy of 511 keV due to the annihilation process, initiated by administered positron emitters. New techniques were therefore required to use isotopes with gamma energies above 600 keV. The concept of a Compton camera was proposed in 1974 [TNE74] to detect γ radiation regarding medical diagnosis. Nowadays, Compton cameras are used in various fields, not only in medical imaging, but also in astrophysics and nuclear safety.

4.1. Working principle

As the name suggests, the working principle of a Compton camera is based on the Compton effect (see section 2.2.2). Its purpose is the reconstruction of the origin of the incoming photon by coincidental measurements. The basic idea, shown in Figure 4.1.1, is as follows: The Compton camera consists of two layers: one scattering layer and one absorption layer. If an incident γ travels to the scattering layer, it can undergo Compton scattering. The interaction probability depends on the thickness of the scattering layer. Afterwards, the scattered photon is absorbed in the absorption layer. The spatial coordinates of the interaction points are determined for both at the scattering ($x_s,\ y_s$ and z_s) and the absorption layer ($x_a,\ y_a$ and z_a), as well as the energy E'_γ of the absorbed photon. These interaction locations are important since they provide the axis that encloses the Compton angle θ with the trajectory of the incoming gamma. As a result, one obtains the Compton ellipse, which defines all the possible locations of the radiation source that emitted the initial photon. The coincidental detection at the scattering layer and the absorption layer also works as a natural background rejection. An input is automatically assigned as a background event if a hit is only registered in one layer.
In case of knowing E_γ, one can calculate the Compton angle θ_γ according to equation 2.19. If the energy of the incident γ is unknown, its energy can be calculated considering the recoil energy

$$T = E_\gamma - E'_\gamma \tag{4.1}$$

which corresponds to the total kinetic energy of the electron, leading to

$$\cos\theta_\gamma = 1 - m_e c^2 \left(\frac{1}{E'_\gamma} - \frac{1}{E_\gamma} \right) \tag{4.2}$$

$$= 1 - \frac{m_e \ c^2 \ T}{E'_\gamma (E'_\gamma + T)} \tag{4.3}$$

after substituting in 2.19. This allows, for example, dose monitoring in proton therapy, which causes photon emission of different energies.

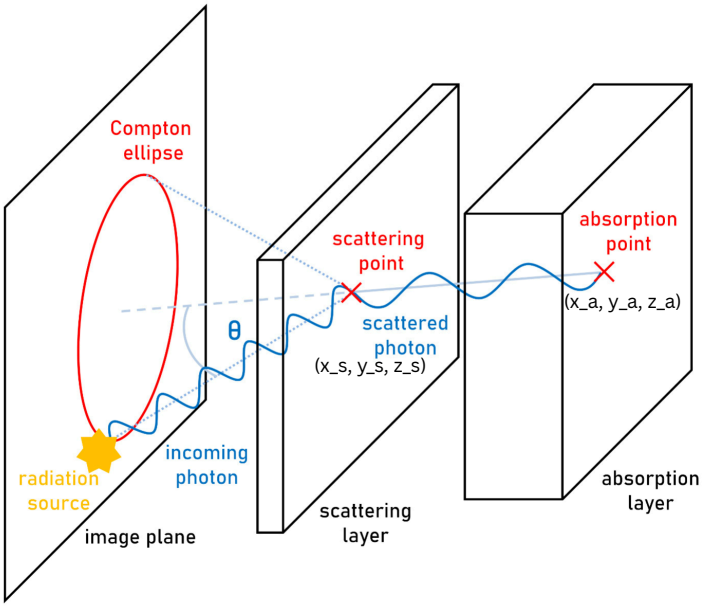

Figure 4.1.1.: Basic theoretical setup of a Compton camera. Edited version from [Lar25].

Each reconstructed photon creates a Compton ellipse in the image plane. This limits the source position on the ellipse's contour. The detection of many photons leads to overlapping ellipses (Figure 4.1.2). In the optimal case, all ellipses intersect at the same point, shown on the left side. Since all photons originate from the same point, the intersection point, represented as a red circle, can be identified as the source location. However, in reality, each reconstruction has its uncertainties. Suppose the position detection in the scattering layer and the absorption layer has a reconstruction uncertainty. This causes a displacement, and not all Compton ellipses will intersect at one point (right side of Figure 4.1.2). A similar problem occurs if the energies of the outgoing particles have a large measurement uncertainty.

4.2. Cherenkov-Compton camera

In the last couple of decades, several Compton camera variations were developed. Most of them only focus on the photon part, neglecting the Compton electron, limiting the usage to known monoenergetic sources. The other Compton cameras, denoted as 'Electron Tracking Compton camera' (ECCT), pursue the extraction of additional information about the Compton electron. The downside of those current systems is the thin

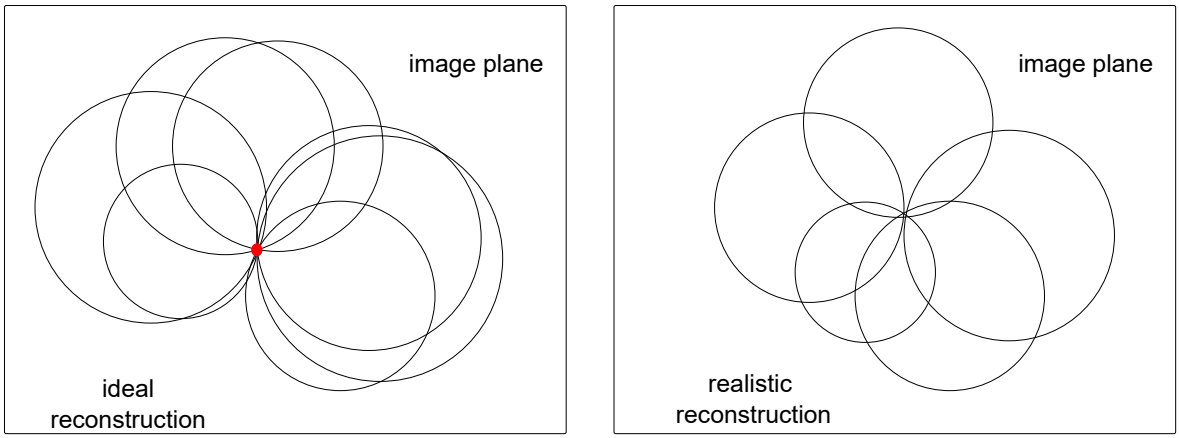

Figure 4.1.2.: Illustration of a source reconstruction using Compton overlapping Compton ellipses. The point with the most intersections is determined as the source position. Left: Idealistic reconstruction for a point source and a monoenergetic gamma beam. All ellipses intersect at one point (red circle). Right: Multiple ellipses are reconstructed, but not intersecting at one point, but slightly misplaced. The uncertainty for the source localisation increases.

detector layers. The developed semiconductor-based in [Yos+17] consists of an absorption layer of 8 scintillator array of Gadolinium Aluminium Gallium Garnet (GAGG), each with dimensions of $3 \times 10 \times 10\,\mathrm{mm}^3$. Although good in spatial resolution, they only allow the detection of gamma rays between 100 keV and 300 keV. Photons with higher energies will traverse the scintillator without depositing all of their energy inside the detector.

The Cherenkov-Compton camera, proposed in [PBW12], represents a novel approach to investigating Compton electrons using transparent materials for the scattering layer. After its creation, the Compton electron's energy is high enough to produce Cherenkov photons in the scattering layer. The electron energy can then be reconstructed by detecting the number of produced Cherenkov photons, while information about the momentum direction can be extracted from the Cherenkov cones themself. Studies in [Bay20] simulated Compton electrons up to 2.3 MeV using a ^{90}Sr source. Measurements showed that Cherenkov photons are produced in transparent materials, like polymethyl methacrylate (PMMA). Due to the wavelength of Cherenkov photons, the PMMA needs to be UV-transparent. Cherenkov photons were successfully detected by coincidence measurements using an 8×8 silicon photomultiplier (SiPM) array.

For the Cherenkov-Compton camera, the desired scattering layer consists of a UV-transparent PMMA (refractive index $n = 1.49$), coupled to a SiPM matrix. Since the energy range is designated in the low MeV range, the electrons can be considered ultra-high relativistic with velocities $\beta \approx 1$, so that the Cherenkov photons are emitted under an angle of 47.8°. For the absorption layer, a similar design of existing Compton cameras is considered, based on a combination of scintillator crystals and SiPMs.

Exploiting the Cherenkov effect allows the determination of Compton electrons above 1 MeV, and hence, the reconstruction of incoming photons in the low MeV region. However, this faces some challenges. Since the electrons undergo multiple scattering in the PMMA, each Compton electron produces multiple overlayed Cherenkov cones with slight offsets from each other. Only the first created Cherenkov cone after reaching the scattering layer allows the extraction of momentum information, but all photons hit

the SiPM with time differences in the range of ps, which means that the Cherenkov cones can no longer be distinguished based on the detection times. This challenge is currently being investigated using AI, which computes the initial Cherenkov cone using the spatial distribution of the Cherenkov photons. Another issue is the assignment of the detected number of Cherenkov photons to the corresponding energy. A detection of all created photons is impossible, because of the photon detection efficiency of detectors, but also their structure. A SiPM matrix allows a spatial resolution, but includes dead spaces between each single SiPM. This effect can be compensated for if the expected amount of detected photons is known. Therefore, an investigation of the mean number of Cherenkov photons produced for different electron energies inside PMMA is necessary.
All in all, the Cherenkov effect offers a promising way to improve the concept of the Compton camera and extend its scope of application in the MeV range.

5. Electron monochromator

As already mentioned, the novel approach of the Cherenkov Compton camera involves the Compton electrons created in the scattering layer. This requires a detailed investigation of such electrons. The electron monochromator refers to an application in which emitted electrons are filtered by their energies, resulting in a 'monochromatic' electron beam with a narrow energy width.
Electron monochromator applications play a crucial part in creating low-energy electrons for mass spectroscopy, see [Lar+96]. In contrast to [Lar+96], our aim is the generation of a monochromatic electron beam with energies between hundreds keV to a few MeV, like in [Arf+15]. This beam will be used to validate Geant4 simulations regarding the production of Cherenkov photons by Compton electrons within the scattering layer of the Cherenkov Compton camera.

5.1. Working principle of an electron monochromator

The principle of the electron monochromator can be seen in Figure 5.1.1. The emitted electrons of a ^{90}Sr source traverse a magnetic field, causing a bending. Electrons with a specific energy will exit the electron collimator, depending on the applied field. This resulting monochromatic electron beam can then be used for spectroscopy experiments or the production of Cherenkov radiation.

5.2. Experimental setup of the electron monochromator

The laboratory electron monochromator experiment consists of a customized vacuum chamber (Figure 5.2.1) made of aluminum. The chamber can be divided into three main areas:

Source chamber

At first, there is the source chamber. It is the biggest chamber part with a volume of 300 mm × 100 mm × 100 mm and contains the source holder, shown in Figure 5.2.2. The source is placed on the sledge on top of the holder. A 200 mm long motorized LTM80P linear stage, manufacturized by OWIS, forms the basis of the holder, allowing a translational source placement along the y-axis with a positioning error up to 25 µm per 100 mm and a bidirectional repeatability of less than 15 µm [OWI20]. All parts of the source holder are mechanically connected to the linear stage, ensuring linear movement. A DMT65 rotary stage provides the rotational alignment with a repeatability of 0.02° [OWI22]. Above the rotary stage, a plate is fixed, on which a sledge with the radioactive source is placed.

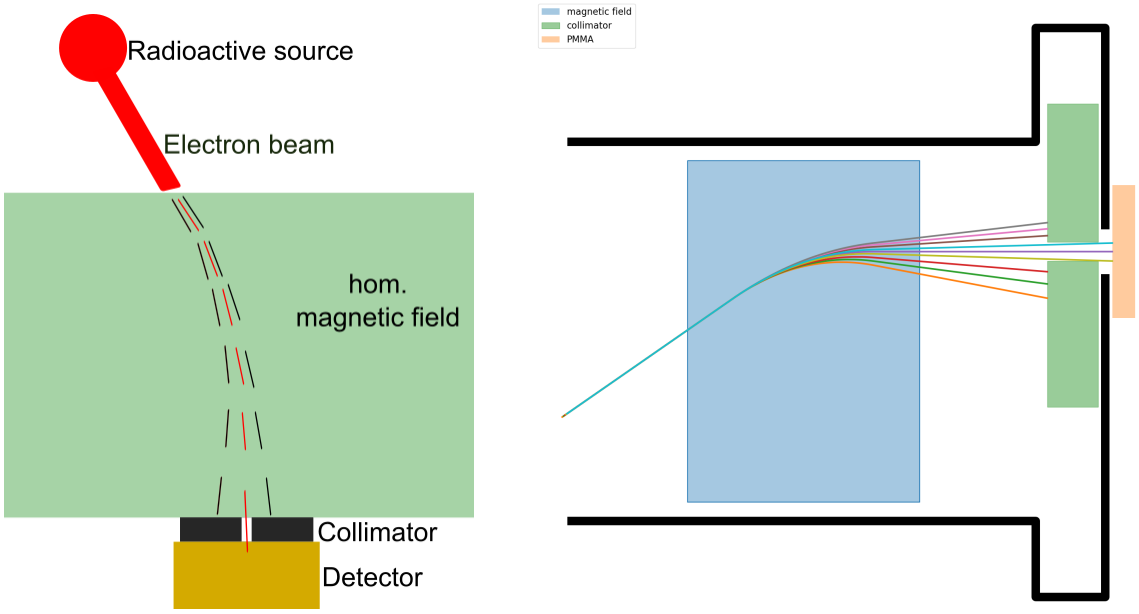

Figure 5.1.1.: General scheme of an electron monochromator. Left: general principle of an electron monochromator. Electrons will be separated while traversing a homogeneous magnetic field. Right: Electrons are fanned out inside due to the magnetic field.

The pivot point, which is crucial for the angular orientation of the source, is located inside the magnet chamber at the beginning of the homogeneous magnetic field section by using two bars. This is necessary to minimize the uncertainty in determining the source position. A rectangular Mu metal tube (5.2 mm height, 13.9 mm width, 86 mm length) is fixed on top to shield the electrons from inhomogeneous fields.

Magnet chamber

The source chamber is followed by the magnet chamber, in which the path of the electrons will be bent. A surrounding dipole electromagnet, made of an iron yoke and two copper coils, 234 windings each, provides a homogeneous magnetic field of $6 \times 6\,\mathrm{cm}^2$ along the z-axis [Koo23]. Detailed studies about the behavior of the standing-alone magnet, for example, the magnetic field profile for the stand-alone magnet, can be found in [Koo23]. A detailed investigation about the magnetic field inside the vacuum chamber will be discussed in the chapters 11 and 12. Multiple fans are used for cooling down the magnet, while the magnet's temperature is constantly monitored with an attached PT100 temperature sensor to prevent overheating. A permalloy is placed behind the homogeneous part to shield electrons from inhomogeneous fields.

Collimator chamber and detector

At the end, there is the collimator chamber, housing the used collimator. The collimator has a total length of 22 mm and can be opened up to 5.5 mm. It consists of 3 different layers (PVC, aluminum, and lead) to stop not only any stray or scattered electrons, but the lead layer also shields against the produced γ radiation in the PVC or aluminum by bremsstrahlung, caused by electrons. The exit of the collimator chamber is open. Depending on the respective measurement,

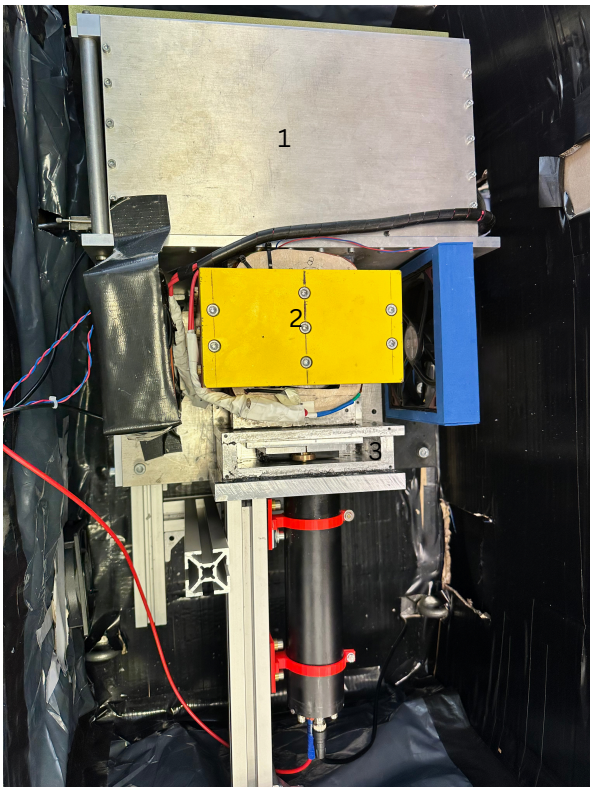

Figure 5.2.1.: Experimental setup (top view), consisting of three connected parts. Part 1: source chamber; contains the source holder with the source. Part 2: magnet chamber, surrounded by the electromagnet (yellow); emitted electrons will bend here. Length: 170 mm. Part 3: collimator chamber, containing collimator. The detector (here: BC-408 scintillator and PMT) is attached to the collimator chamber.

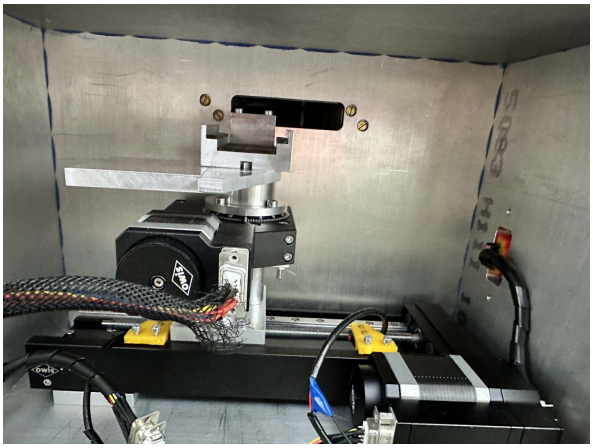

Figure 5.2.2.: Source holder, positioned via two stepping motors, inside the source chamber.

either an additional detector chamber part has to be connected or the chamber is closed by a scintillator material.

Additional information, especially about the vacuum chamber and the magnet's characterization, can be found in [Koo23].

5.3. Implementation in Geant4

The basic setup of our electron monochromator in Geant4 can be seen in Figure 5.3.1. The particle gun (red circle) is defined as a point-like electron source and is attached to Mu metal, whose position and angle are variable along the y-axis. After leaving a Mu metal, the electrons are bent in a 6 cm long magnetic field. Afterwards, a collimator selects the desired electrons. The outgoing electrons will produce Cherenkov radiation within a PMMA layer. Resulting photons are detected by several SiPM arrays behind the PMMA. The entire simulation environment is filled with an air mixture, based on a 7:3 carbon-oxygen mixture.
This implementation serves two purposes. The first goal is to study the effect of the remaining gas inside the chamber to set mandatory measurement conditions for the experimental setup. The second aim is the investigation of the electron energy resolution after the collimator at the PMMA, which will then be compared with experimental data.

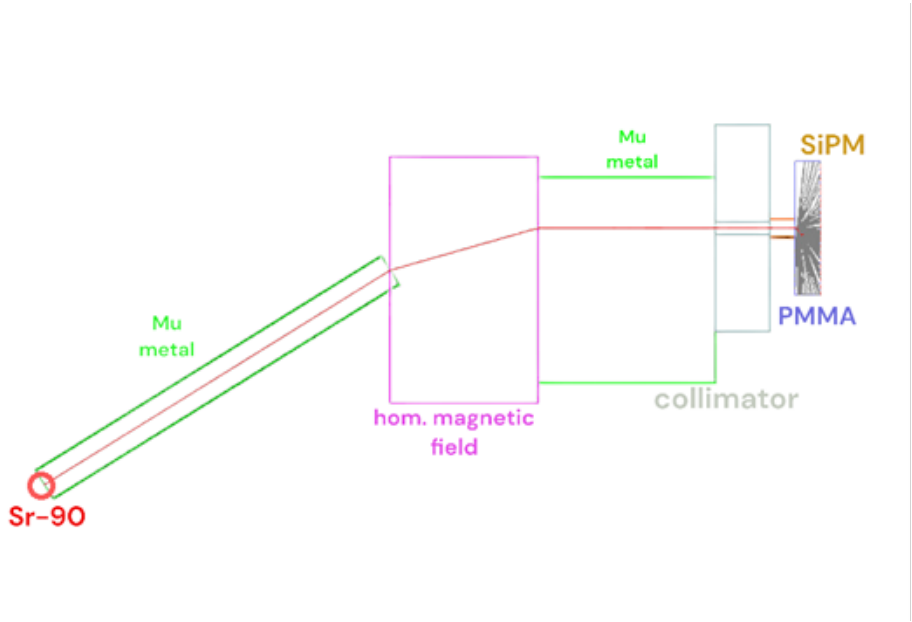

Figure 5.3.1.: Geant4 setup for the electron monochromator. Produced electrons from a simulated ^{90}Sr source (red circle on the left) are selected by a combination of a homogeneous magnetic field and a collimator. The outgoing particles enter the PMMA to produce Cherenkov radiation, represented as white lines, which are detected by SiPM arrays. The red line indicates an electron trajectory.

6. Numerical calculations

The electron trajectories mainly depend on the applied magnetic field and their energies, causing a variable source position. Only those electrons that traverse through the collimator in parallel and arrive at the detector perpendicularly are the ones of interest, while all the other electrons reduce the energy resolution. Therefore, to ensure a perpendicular arrival of electrons at the detector, numerical calculations are required to determine the source position and angular direction for a given electron energy and applied field.

Although Geant4 is capable of determining the respective source position during simulations, this is not optimal and requires lots of computational resources.

6.1. Numerical calculation for source position

Calculating the source position is a crucial step in making accurate measurements. For this, a C++ script is written, which iteratively calculates the electron trajectory for a given magnetic field and electron energy by solving the Newtonian equation of motion

$$\vec{F} = \dot{\vec{p}}\,, \tag{6.1}$$

whereby $\vec{F}$ denotes the total external force on the electron and $\dot{\vec{p}}$ the electron's temporal momentum change. The geometry is the same as for the Geant4 simulations.
This numerical calculation takes the following assumptions into account:

- Electrons with the desired energy will traverse right through the collimator center and hit the PMMA perpendicularly.
- The source is point-like and emits electrons only in one direction, meaning that the opening of the collimated source is infinitesimally small. This implies that for each setting, only one trajectory is computed.

Since the only considered external force is the Lorentz force $\vec{F}_\mathrm{L}$ within the magnetic field section, it is

$$\vec{F} = \begin{cases} 0 & \text{outside magnetic field area,} \\ \vec{F}_\mathrm{L} = q \cdot \left(\vec{v} \times \vec{B}\right) & \text{inside magnetic field area.} \end{cases} \tag{6.2}$$

The particles are emitted in the xy plane, while the magnetic field is aligned to the negative z-axis. The origin of the coordinate system is placed in the center of the magnetic field.

The algorithm is time-based, which means each iteration step i corresponds to a time step dt. This iteration time is set to 1×10^{-15} s, corresponding to a travel distance of roughly tens of micrometers per iteration. During each iteration, the particle moves by a distance $\mathrm{d}\vec{r} = (\mathrm{d}x,\ \mathrm{d}y,\ \mathrm{d}z)$.
Each iteration consists of the following steps:

1. calculate the particle's acceleration $\vec{a}_{\mathrm{i}}$ by solving equation 6.1
2. determine new velocity vector: $\vec{v}_{\mathrm{i}} = \vec{v}_{\mathrm{i\text{-}1}} + \vec{a}_{\mathrm{i}} \cdot \mathrm{dt}$
3. calculate traveled distance: $\vec{dr}_{\mathrm{i}} = \vec{v}_{\mathrm{i}} \cdot \mathrm{dt}$
4. calculate new position: $\vec{r}_{\mathrm{i}} = \vec{r}_{\mathrm{i\text{-}1}} + \vec{dr}_{\mathrm{i}}$
5. calculate bending angle $\varphi_{\mathrm{i}} = \arctan\left(\frac{\mathrm{dy}}{\mathrm{dx}}\right)$

At the beginning of the calculation, the electron is located right in the center of the collimator at position $\vec{r}_0$, and its momentum direction is set along the negative x-axis. The corresponding velocity's absolute value is calculated via special relativity based on the electron's kinetic energy $E_{\mathrm{kin}} = (\gamma - 1)m_e c^2$ by

$$v_0 = \sqrt{1 - \frac{1}{\gamma^2}} \cdot c = \sqrt{1 - \frac{1}{\left(\frac{E_{\mathrm{kin}}}{m_e \cdot c^2} + 1\right)^2}} \cdot c \quad . \tag{6.3}$$

The final source position is defined by the length of the small mu metal, since it lies between the start of the homogeneous field and the source. There is no fixed x-coordinate for the source, due to the angle-dependency of the trajectory.
Since this calculation procedure solves the general Newtonian equation without making any assumptions about the applied magnetic field, a modification for inhomogeneous fields is possible. It is also easily adjustable in terms of geometrical changes, such as changes of the first Mu metal. However, these calculations only predict the source position for a perfect monochromatic beam, neglecting angular distributions and stochastic physical interactions. Therefore, some deviations between the numerical calculations and simulations are to be expected; however, the resulting positions provide a suitable starting point for the investigations.

6.2. Source position calculation and verification

Figure 6.2.1 illustrates the resulting trajectories for electrons between 0.8 MeV and 2.2 MeV in a 40 mT field to hit the PMMA perpendicularly. As expected, lower energies lead to larger angles. Bending only occurs inside the magnetic field area. Electrons with energies of 0.8 MeV and below will bend too much and hit the chamber. These electrons need a lower applied magnetic field. Furthermore, high-energy electron trajectories are much closer together than low-energy electrons. The results for 40 mT are summarized in Table 6.1. For a first check, the velocity's absolute value $|\vec{v}_0|$ is compared with the resulting velocity after the calculation $|\vec{v}_{\mathrm{end}}|$. The absolute value can increase during an iteration, and the bigger the iteration time, the greater the deviation from $|\vec{v}_0|$, and the less precise the calculation. All deviations are below 0.1 %, confirming that the chosen iteration time is adequate. The x and y positions correspond to the source coordinates in the Geant4 coordinates, where the origin is defined as the center of the magnetic field, and φ is the bending angle to the x-axis. The coordinate x depends on the angle φ, and thus can vary.

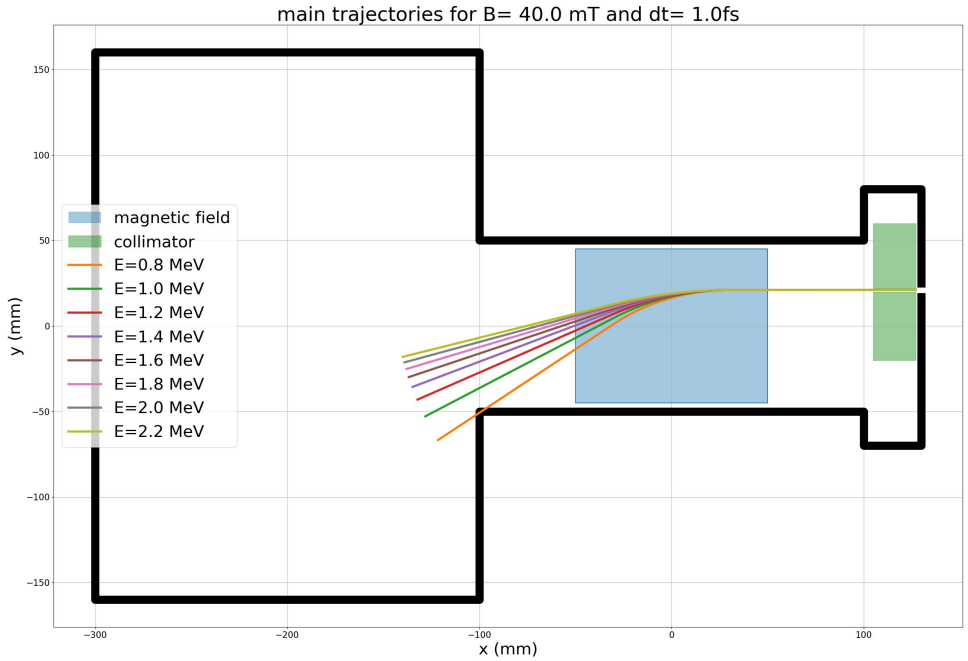

Figure 6.2.1.: Electron trajectories for 40 mT homogeneous field.

Energy (MeV)	$\lvert\vec{v}_0\rvert$ ($\times 10^8 \frac{m}{s}$)	$\lvert\vec{v}_{\text{end}}\rvert$ ($\times 10^8 \frac{m}{s}$)	x_{pos} (mm)	y_{pos} (mm)	Angle φ (°)
0.8	2.761	2.761	-162.50	-97.17	36.58
1.0	2.821	2.821	-172.32	-78.79	30.40
1.2	2.861	2.861	-178.12	-65.64	26.14
1.4	2.889	2.889	-181.98	-55.68	23.00
1.6	2.909	2.909	-184.48	-47.85	20.57
1.8	2.924	2.924	-186.37	-41.51	18.62
2.0	2.935	2.935	-187.78	-36.27	17.02
2.2	2.944	2.944	-188.86	-31.85	15.68

Table 6.1.: Numerical results for dt $= 1 \times 10^{-15}$ s for 40 mT homogeneous magnetic field for the starting position and angular orientation. The total difference between the final calculated velocity $\lvert\vec{v}_{\text{end}}\rvert$ and the initial velocity $\lvert\vec{v}_0\rvert$ is less than 0.1 % and validates the step size dt. The origin of the coordinate system for the calculated positions is set to the center of the magnetic field. The x position x_{pos} is the position of the source along the x-axis. This position depends on the angle φ.

One can validate these results by using them in the simulations. While the particle gun's location is defined by the coordinates (no movement in z direction, meaning z=0), the angle φ is required for the angular alignment of the first Mu metal as well as the main direction for the emitted electrons. To minimize electron interactions with surrounding gas molecules, the vacuum quality is maximized (low pressure). These settings replicate the numerical calculations, as all physical effects except for the bending within the magnetic field region are neglected. The resulting trajectory for a main energy of 1.4 MeV is depicted in Figure 6.2.2. The electrons pass the 0.1 mm wide

collimator opening, verifying the correctness of the numerical calculations.

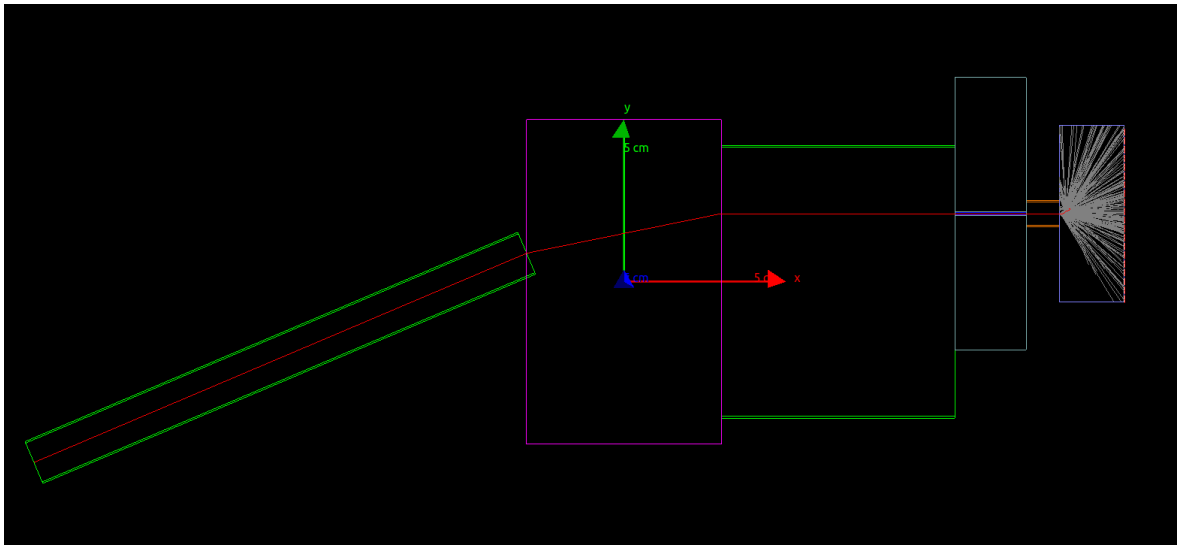

Figure 6.2.2.: Trajectory (red line) for a 1.4 MeV electron beam in Geant4, using the calculated source position. The electron passes through the 1 mm collimator opening and creates Cherenkov photons (grey lines).

6.3. Estimation for energy resolution

Electrons with different energies bend differently, causing an energy spread after passing the magnetic field, as shown in Figure 6.3.1. As long as the used source does not provide monoenergetic particles, an energy spread is unavoidable. Low-energy electrons will bend more than higher-energy ones since they are affected longer in the magnetic field region.

The numerical script cannot only determine the source positions but also numerically estimate the energy spread for an ideal monoenergetic pencil beam by starting at the calculated positions. Since the numerical calculations are based on time iteration, adding a minus sign will reverse the travel direction. The electron spread will then depend on the collimator opening and the applied magnetic field.
Table 6.2 lists the energy limits for 40 mT. The considered energy range is $E_{\text{main}} \pm 0.4\,\text{MeV}$ with energy steps of 1 keV. The resulting energy spread after passing the collimator opening is calculated by taking the relative error

$$\sigma_E = \frac{\max(|E_{\text{main}} - E_{\text{limit}}|)}{E_{\text{main}}} \,. \tag{6.4}$$

E_{limit} denotes either E_{min} or E_{max}, depending on the maximum absolute difference to E_{main}. The calculated energy spread for a 5 mm collimator lies below 10 %. Increasing the magnetic field yields a better resolution. Pivot tables about the energy resolution for different collimator apertures can be found in Appendix A.1.

Note: The energy distributions given here merely estimate the absolute energy difference between the desired (main) electrons and the energy of those electrons that

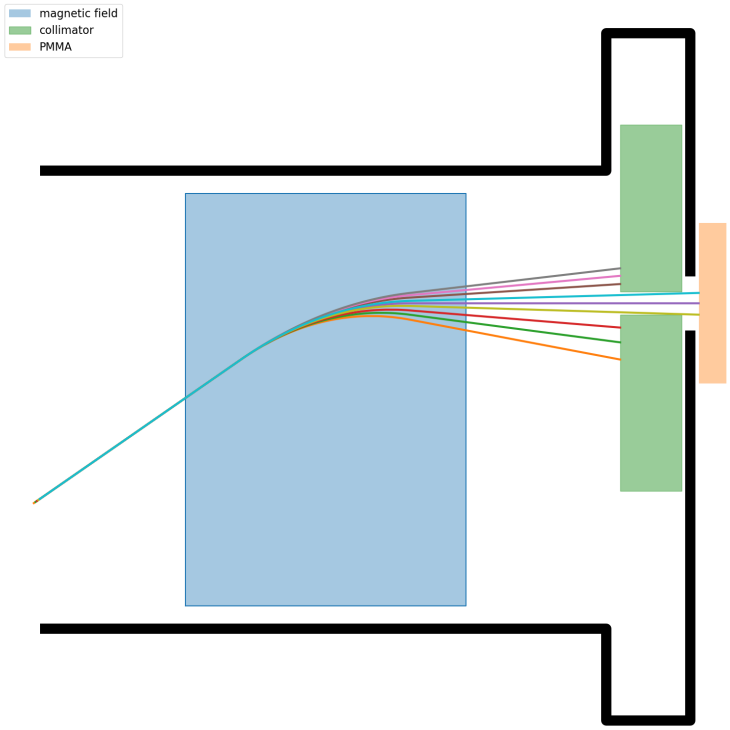

Figure 6.3.1.: Visualization of the electron selection. The electrons are fanned out in the magnetic field. (blue). The collimator (green) limits the electrons that can pass to the detector/PMMA.

E_{main} (MeV)	E_{min} (MeV)	E_{max} (MeV)	σ_E (%)
0.8	0.766	0.837	4.6
1.0	0.951	1.053	5.3
1.2	1.135	1.272	6.0
1.4	1.316	1.493	6.6
1.6	1.496	1.717	7.3
1.8	1.674	1.943	7.9
2.0	1.850	2.172	8.6
2.2	2.024	2.404	9.3

Table 6.2.: Energy spread for pencil-like electron beam for 5 mm collimator opening and 40 mT.

still pass through the collimator. These estimates are calculated differently from the Geant4 energy resolutions in the following chapters (e.g. Chapter7), in which a Gaussian distribution is used.

7. Quantitative parameter estimation using Geant4

A series of parameter studies is performed in order to evaluate the distribution of the electron energies after passing the collimator. The big benefit of using Geant4, compared to classic numerical calculations, is the inclusion of several physical interactions, such as particle interactions with matter. Using Geant4 is a proper way to simulate and verify the physical behavior. For the first studies about the quantitative behavior of the electron monochromator, the following three parameters are investigated: vacuum quality, collimator aperture, and the applied magnetic field. All primary electrons follow a ^{90}Sr spectrum distribution, an example is shown in Figure 7.0.1. The source position in each simulation is set in that way so that electrons with an energy of 1.4 MeV will ideally pass through the collimator center and hit the PMMA perpendicularly. The vacuum quality is fixed on a temperature $T = 288\,\mathrm{K}$ and pressure $P = 10\,\mathrm{mbar}$, except for the simulations in section 7.1. Furthermore, unless otherwise specified (Chapter 7.3), a homogeneous magnetic field of 40 mT is assumed in all simulations. Since a collimated source is used, there are some angular restrictions for the electron emission. Electrons with an emission angle outside the defined range are rejected.

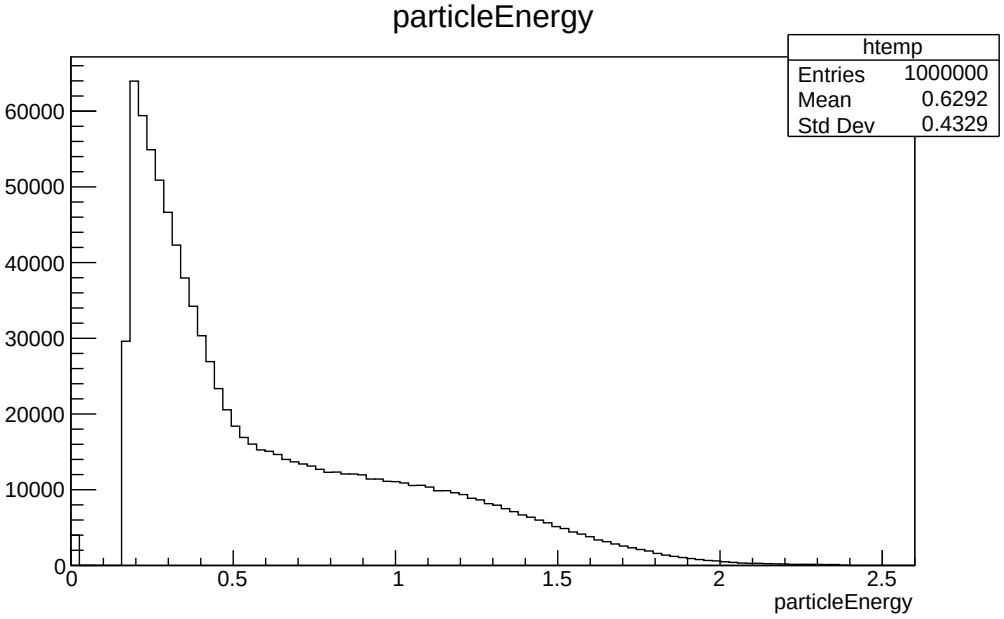

Figure 7.0.1.: Example of an energy distribution of primary electrons in Geant4 simulations. The distribution follows a ^{90}Sr beta spectrum.

7.1. Vacuum quality

The first simulation series is about the effect of the vacuum quality by changing the pressure. Geant4 determines all material properties based on the density; therefore, the density ρ has to be determined as a function of the pressure P and temperature T. Its relation can be derived by using the ideal gas equation

$$PV = nRT \ , \tag{7.1}$$

with the universal gas constant R, volume V and amount of substance n. n can be expressed as a ratio of the overall mass of the vacuum gas m and the molar mass M_{mol}, which can be rewritten in terms of the density

$$n = \frac{m}{M_{\text{mol}}} = \frac{\rho V}{M_{\text{mol}}} \ . \tag{7.2}$$

After inserting equation 7.2 in 7.1 and solving for ρ, one obtains the following relation

$$\rho\,(P,T) = \frac{P M_{\text{mol}}}{RT} \ . \tag{7.3}$$

In all simulations, the temperature was fixed to 288 K, and for the vacuum gas, the molar mass of dry air at sea level, $M_{\text{mol}} = 28.96\,\frac{\text{g}}{\text{mol}}$, was used. The collimator opening is set to 3 mm.
Figure 7.1.1 presents the energy distribution of electrons after passing the collimator for different vacuum pressures for no angular spread. All diagrams show a Gaussian-like distributed energy spectrum, whose width reduces for lower pressures, meaning a better vacuum quality. Additionally, the energy peak shifts to lower energies for higher pressures due to the resulting increase in the vacuum density. More gas molecules cause more interactions with electrons and hence more energy transfer from the electrons to molecules, which must be prevented. Even at 20 mbar, the electrons loose around 100 keV, while for 10 mbar, which currently is the limit for the experimental setup, the peak energy differs by 5 keV from the desired energy, and the energy resolution within the 1σ region $\frac{\sigma_E}{E}$ is determined to be 4.3 %. Improving the pressure to 1 µbar can push the resolution even below 3 %, but this is currently not practicable in the experimental setup. Therefore, 10 mbar is used for the following simulations.

In the simulations above, a pencil-like beam is assumed, but since the source emits beta particles isotropically, there will be angular deviations. After adding an angular spread of $\pm 10°$, the electron distribution at the PMMA significantly broadens for all settings (Figure 7.1.2). The source now does not emit a pencil-like beam anymore. The best obtained resolution is $\sigma_E = 19.8\,\%$. Besides the reduction of the energy resolution, a significant energy shift of more than 100 keV can also be observed. This can be explained by the source's emission spectrum, where electrons are emitted at lower energies more likely than electrons above 1.5 MeV. This is due to many electrons at too large or too small angles, respectively. The 5.2 mm × 13.9 mm cross section of the 115 mm long mu metal allows a maximum angular spread

$$\Delta\varphi = \arctan \frac{\sqrt{(5.2/2)^2 + (13.9/2)^2}}{115} = 3.7°. \tag{7.4}$$

at the corner of the mu metal. Since the mu metal is included in the simulation, the angular spread of the electrons that can enter the magnetic field is the calculated spread

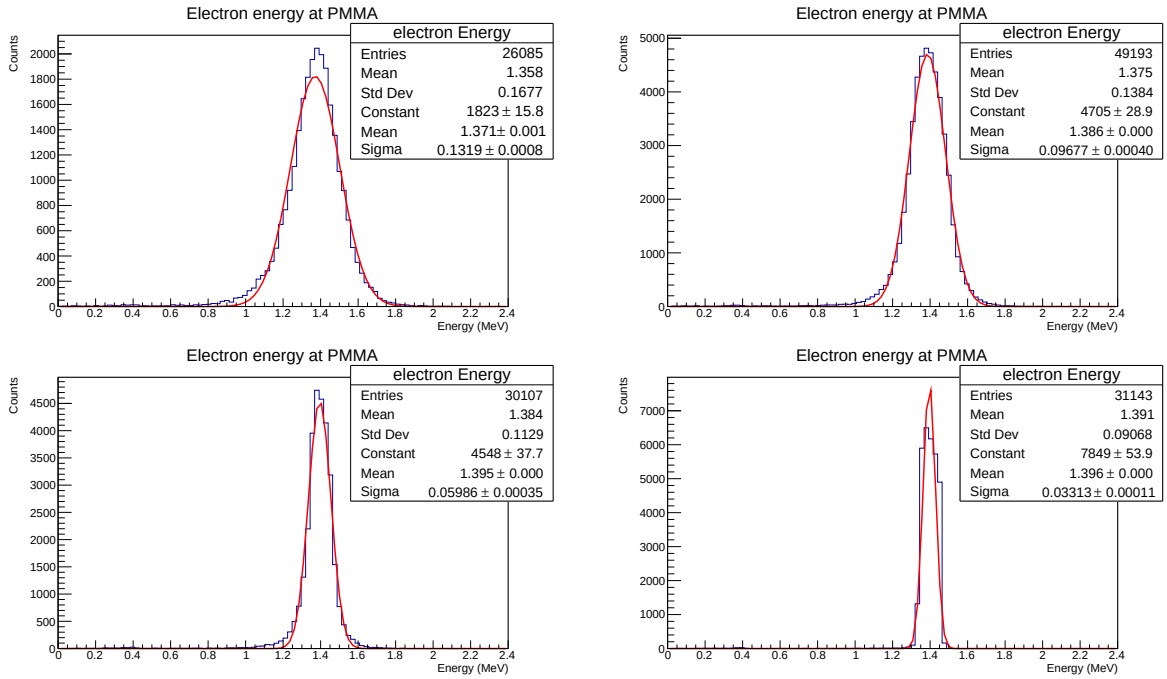

Figure 7.1.1.: Energy distribution of electrons hitting the PMMA for different pressures after passing 3 mm collimator opening. From left to right: first row: 50 mbar and 20 mbar; second row: 10 mbar and 1 µbar. Without angular distribution.

above. Applying this spread in the simulations ensures that all momentum directions for the electrons, which can enter the magnetic field region, are covered, assuming that the source is placed centrically at the mu metal's tube opening. Shortening the mu metal length increases the angular spread. If the mu metal above is cut to a length of 86 m, the maximal angular dispersion is 9.8° An overview of all energy resolutions, obtained after a Gaussian fit, is listed in Table 7.1. This shows that, for a large angular spread, the contribution from the vacuum is small.

	1 µbar	10 mbar	20 mbar	50 mbar
Without angular spread	2.4	4.3	7.0	9.6
With angular spread	19.7	19.8	20.8	21.1

Table 7.1.: Energy resolutions in % for different vacuum quality. The collimator opening is 3 mm and the field is 40 mT. The energy resolution refers to the 1σ region.

7.2. Collimator opening

Another geometry parameter is the collimator opening. For this, simulations are done for openings of 1, 3, and 5 mm at 10 mbar. The collimator itself is not round. Therefore, the values above correspond only to the y-axis, while the height remains the same (32 mm).
The resulting energy distributions for all three conditions above, including a 10° angular spread, are shown in Figure 7.2.1. The energy resolution improves inversely proportional to the collimator opening, while the number of hits is proportional to

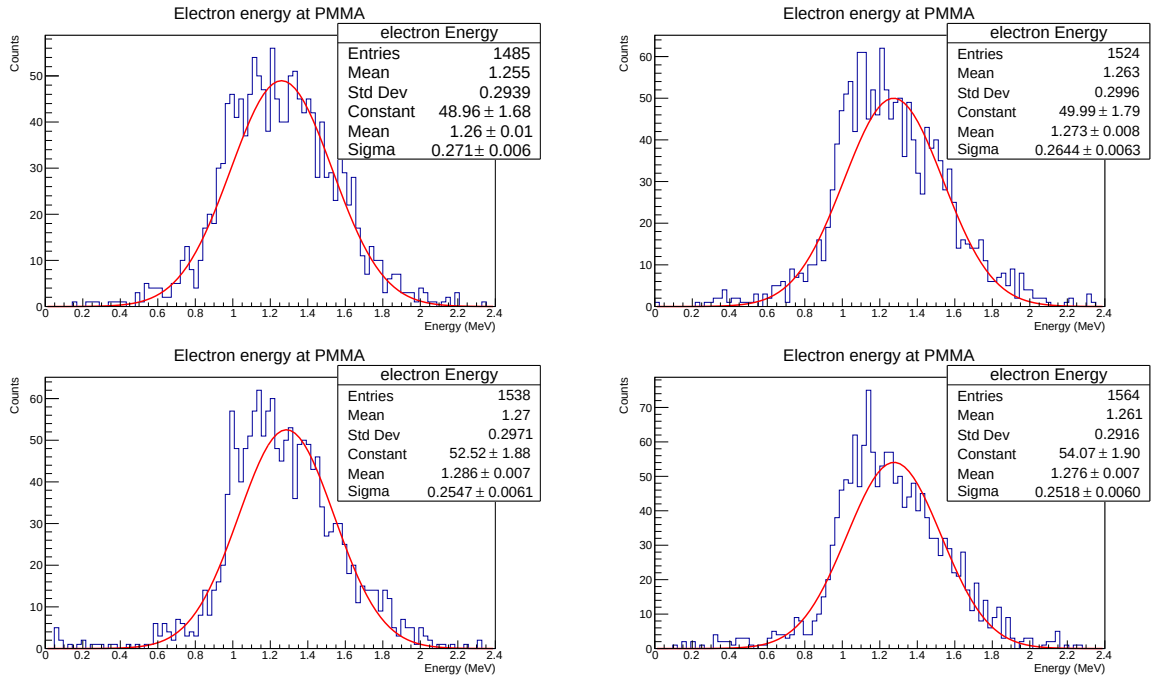

Figure 7.1.2.: Energy distribution of electrons hitting the PMMA for different pressures after passing 3 mm collimator opening, including an angular spread.. From left to right: first row: 50 mbar and 20 mbar; second row: 10 mbar and 1 µbar.

the opening. Similar to the vacuum quality, a significant energy shift can be further observed. The overall fit results are listed in Table 7.2. The best energy resolution in these simulations, including an angular spread, is 18.5 % for the 1 mm opening. Reducing the opening even further might improve the energy resolution. The angular spread dominates the energy spread, similar to the vacuum quality.

	1 mm	3 mm	5 mm
Without angular spread	3.1	4.3	5.7
With angular spread	18.5	19.8	21.1

Table 7.2.: Energy resolutions in % for different collimator openings. The pressure is fixed on 10 mbar and the magnetic field is 40 mT. The energy resolution refers to the 1σ region.

7.3. Magnetic field

The last examined parameter is the magnetic field strength, tested with a 40 and 60 mT field, whose energy distributions at the PMMA are depicted in Figure 7.3.1. A stronger magnetic field leads to a smaller energy spread. Additionally, the 60 mT field counteracts the additional energy spread more efficiently than the 40 mT field, which can be seen in the second row. However, the influence of the angular spread is too much to create a monoenergetic-like electron beam with the current fields. The energy resolutions are listed in Table 7.3. The energy resolution for a 60 mT applied magnetic field is 14.9 %.

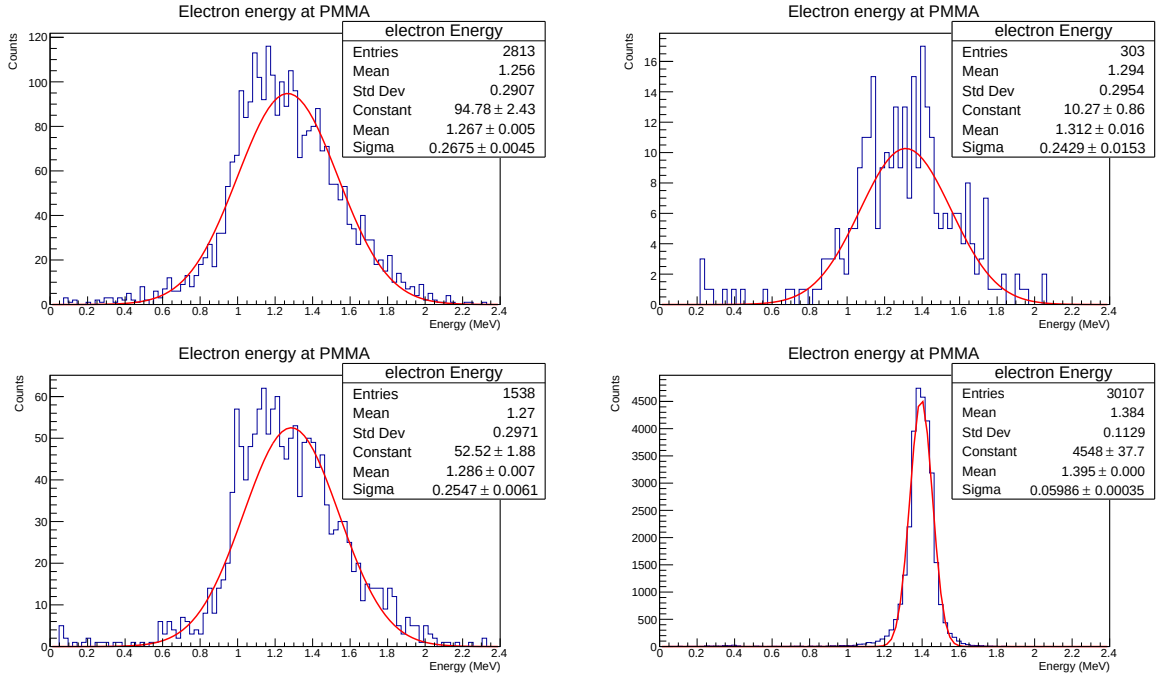

Figure 7.2.1.: Energy distribution of electrons hitting the PMMA for different collimators, including an angular spread. From left to right: first row: 5 mm and 1 mm; second row: 3 mm and 3 mm without angular spread.

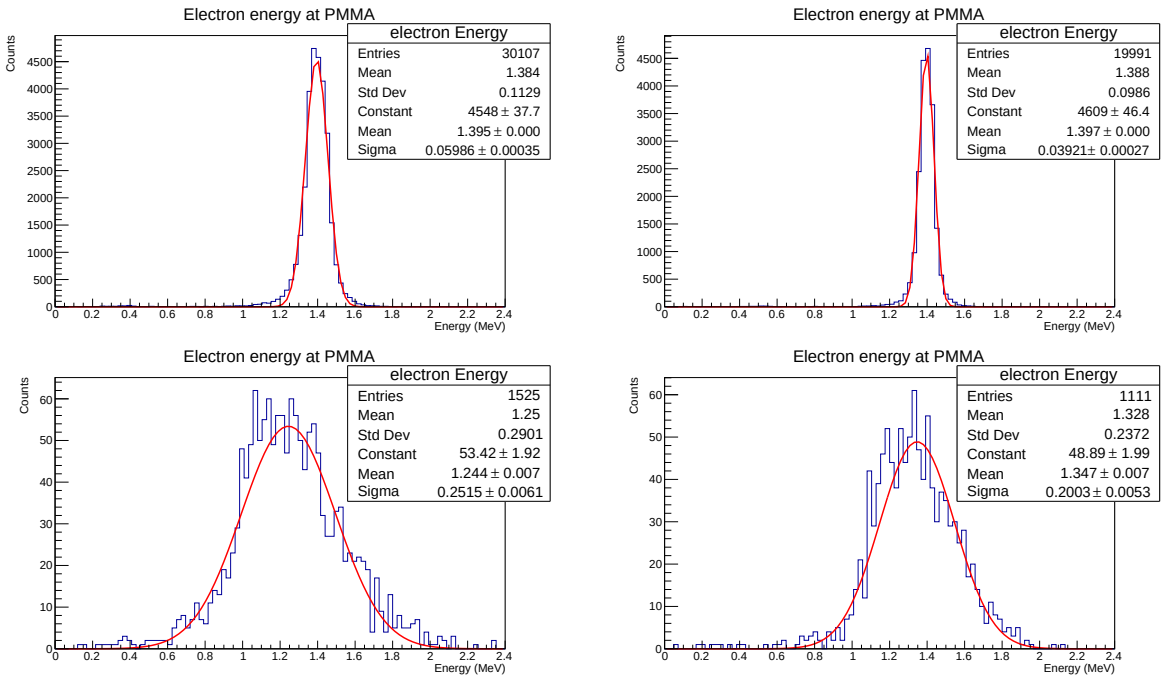

Figure 7.3.1.: Energy distribution of electrons hitting the PMMA for magnetic fields. From left to right: first row without angular spread: 40 mT and 60 mT. Second row with 10° angular spread: 40 mT and 60 mT.

7.4. Conclusion of the Geant4 simulations

The simulations above point out that a low vacuum of 10 mbar is sufficient for the electron monochromator to prevent a significant energy loss due to electron interactions

	40 mT	60 mT
Without angular spread	4.3	2.8
With angular spread	20.2	14.9

Table 7.3.: Energy resolutions in % for different magnetic fields. The collimator opening is 3 mm and the field is 40 mT. The energy resolution refers to the 1σ region.

with the gas molecules. As expected, the energy selection is optimal for a magnetic field as high as possible. While keeping the collimator aperture small limits the energy distribution, it also reduces the amount of passing electrons, and therefore the statistics.
However, despite optimizing these parameters, the quality of the energy distribution is mainly influenced by the source collimation itself. Additionally, it can cause an energy shift. The dispersion of the source must be reduced by optimizing its collimation.
In the experimental setup, the source is placed inside a housing that prevents uncontrolled radiation from escaping into the environment. Emitted beta particles can only leave this housing through a small collimated aperture; hence, the angular spread depends on its dimensions. Therefore, the components of the experimental setup must be categorized in detail to optimise the energy resolution.

8. Calibration of readout system for experimental setup

While Geant4 simulations allow investigating simultaneously the incoming electron spectrum at the PMMA layer and the corresponding distribution of detected Cherenkov photons, it is experimentally impossible, but needs to be separated into two different steps, i.e.

1. the determination of electron energy distribution behind the collimator and
2. the detection of Cherenkov photons produced by the PMMA layer.

The main experiment is conducted in step two; however, without a proper analysis of the incoming electrons, one cannot assign a resulting Cherenkov photon distribution to a specific electron energy. As already observed in Geant4 simulations in chapter 7, an energy selection can only be obtained up to a certain precision. The resolution is limited by the setup properties, e.g., the collimated opening of the source, which causes angular dispersion. Additionally, stochastic scattering processes with remaining air molecules also lead to energy losses.
For the electron energy distribution for step one, the following three different detector systems were tested:

- Si(Li) pin detector
- BC-408 plastic scintillator with PMT
- sodium iodide scintillator with PMT

The resulting detector signals are then processed with a multichannel analyzer (MCA) after being amplified by a main amplifier. The MCA can analyze positive signals only; therefore, the unipolar output of the main amplifier is used. For the semiconductor detector, an additional preamplifier is required. Figure 8.0.1 shows the readout setup.

The MCA analyzes incoming signals via pulse-height analysis (PHA). PHA is a common method used in spectroscopy to measure an energy spectrum. It is a counting method where an input pulse is assigned to an MCA channel by its amplitude, resulting in an energy spectrum. The lower-level and upper-level discriminators (LLD and ULD, respectively) set the amplitude range in which signals are converted. An additional threshold voltage (THD) marks the upper noise limit, which is usually set slightly above the baseline. Noise, which corresponds to low signals, can be minimized by setting a threshold voltage (THD) above the signal's baseline. The THD not only inhibits noise-triggered signal conversion but also works as a safety mechanism against pile-up. As long as the signal stays above the THD, no new conversion is triggered. The conversion is done during the falling edge, if the peak does not exceed the ULD. Figure 8.0.2 illustrates the internal PHA principle. [Com].

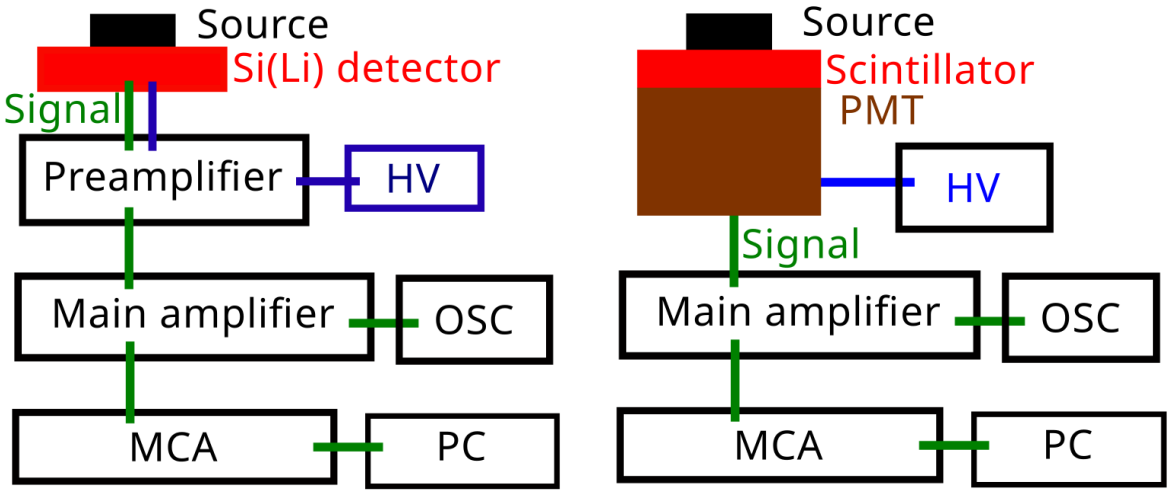

Figure 8.0.1.: Left: readout system using Si(Li) pin detector. Right: readout system using scintillator and PMT. The detector signals are split after the main amplifier to analyze at the MCA and to observe the signal on the oscilloscope (OSC) simultaneously.

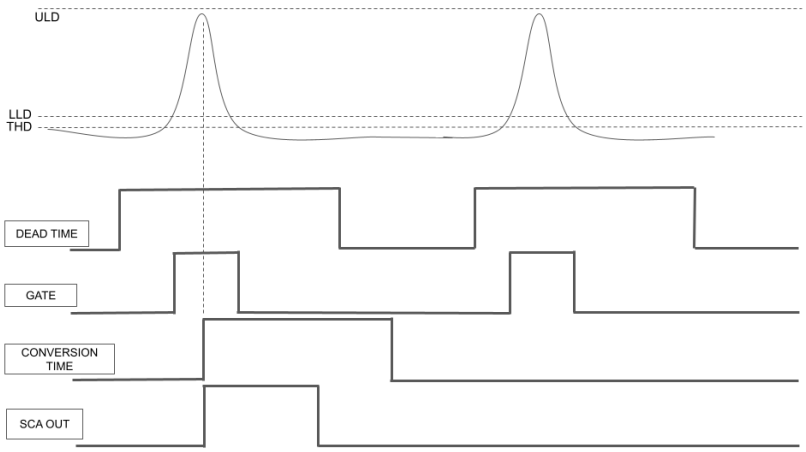

Figure 8.0.2.: Internal principle of pulse-height analysis. A signal is analyzed, defined by the falling edge, if its amplitude lies between UHLD and LLD. Adapted from [Com].

All radioactive sources which are used for the calibration measurements are described in Section 2.3.1.

8.1. Linearity of MCA

Before starting the investigation with the detectors, the MCA is first checked for its behavior regarding incoming signals. For this, a signal generator [1] sent 10 µs signals with amplitudes between 0.5 and 7 V in 500 mV steps to the MCA (Table 8.1). These values can be fitted to check the behavior of the MCA for incoming signals, presented in Figure 8.1.1. It showed that the MCA behaves linearly to the amplitude of incoming signals.

[1] Agilent 33250A

Signal amplitude (V)	MCA channel
0.5	551
1.0	1099
1.5	1661
2.0	2228
2.5	2799
3.0	3373
3.5	3930
4.0	4503
4.5	5078
5.0	5653
5.5	6231
6.0	6807
6.5	7386
7.0	7966

Table 8.1.: MCA channels for different signal amplitudes

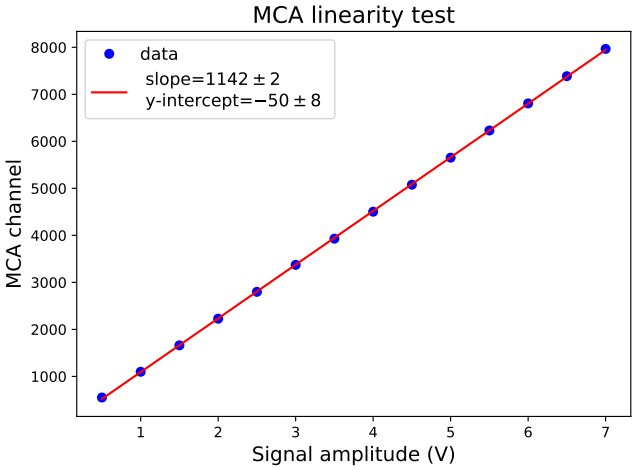

Figure 8.1.1.: MCA linearity check for MCA. The MCA shows a linear behavior.

8.2. Silicon lithium pin detector

The Silicon lithium (Si(Li)) pin detector, shown in Figure 8.2.1, is a semiconductor-based detector, sensitive to charged particles. The detector has a 3 mm thick intrinsic layer and a total sensitive area of 1250 mm^2 [Fle]. For this calibration, ^{207}Bi is used.

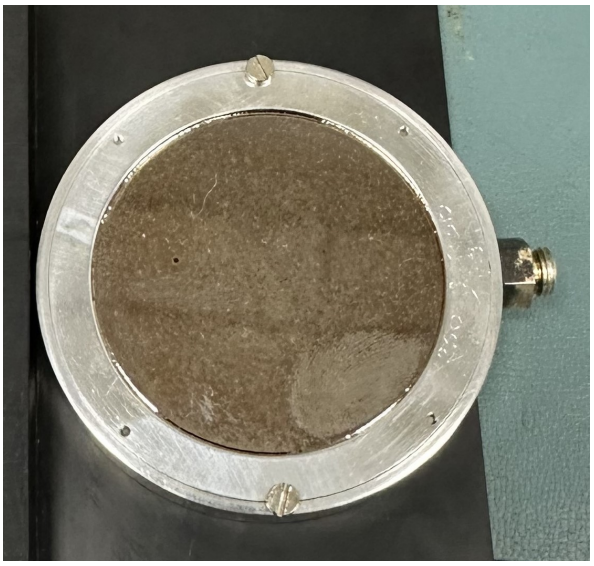

Figure 8.2.1.: Si(Li) pin detector

The calibration curve is based on ^{207}Bi and is validated with ^{137}Cs. An example of a recorded ^{207}Bi spectrum, including fitting, is shown in Figure 8.2.2. Two double peaks can be identified, which can be assigned to the K and L-shell conversion electrons of the first two gamma transitions. Therefore, for both fits, a combination of two double

Gaussians (peak position μ_i and standard deviation σ_i) with a linear background (slope m, y-intercept b),

$$f(x;\mu_1,\sigma_1,\mu_2,\sigma_2,m,b) = \sum_{i=1}^{2} \frac{1}{\sqrt{2\pi\sigma_i^2}} \exp\left(\frac{(x-\mu_i^2}{2\sigma_i^2}\right) + mx + b \ , \tag{8.1}$$

is chosen. This results in a total of 4 usable points for a calibration fit.

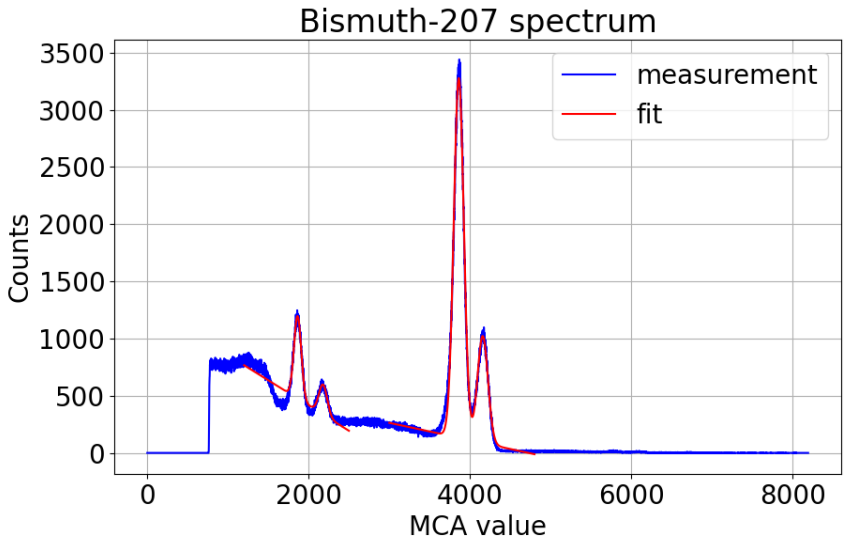

Figure 8.2.2.: ^{207}Bi spectrum, recorded with Si(Li) pin detector.

In contrast, while all peaks of ^{207}Bi are easily distinguishable, the recorded ^{137}Cs spectrum only shows one larger bump, which is slightly deformed. This implies that both conversion K and L-conversion electrons need to be taken into consideration. Figure 8.2.3 illustrates one fitted ^{137}Cs spectrum.

Multiple ^{207}Bi measurements are taken into account, whose fit parameters are listed in Table 8.2. The mean values of the peak positions correspond to the MCA values for the respective conversion electrons, resulting in the linear calibration fit depicted in Figure 8.2.4. The calibration fits with

$$\text{slope: } m = (2.46 \pm 0.06) \times 10^{-4} \tag{8.2}$$

$$\text{y-axis intercept: } b = 0.022 \pm 0.006 \tag{8.3}$$

agrees well with the mean values of the two measured conversion electrons of ^{137}Cs, summarized in Table 8.3. Using the calibration function, one obtains for the ^{137}Cs conversion electron energies

$$\text{K-shell: } \mathrm{CE}(\bar{\mu}_1) = (620 \pm 22)\,\mathrm{keV} \tag{8.4}$$

$$\text{L-shell: } \mathrm{CE}(\bar{\mu}_2) = (656 \pm 23)\,\mathrm{keV} \ . \tag{8.5}$$

The corresponding literature values $\mathrm{CE_K} = 624.216\,\mathrm{keV}$ and $\mathrm{CE_K} = 655.668\,\mathrm{keV}$ agree within the 1σ region.

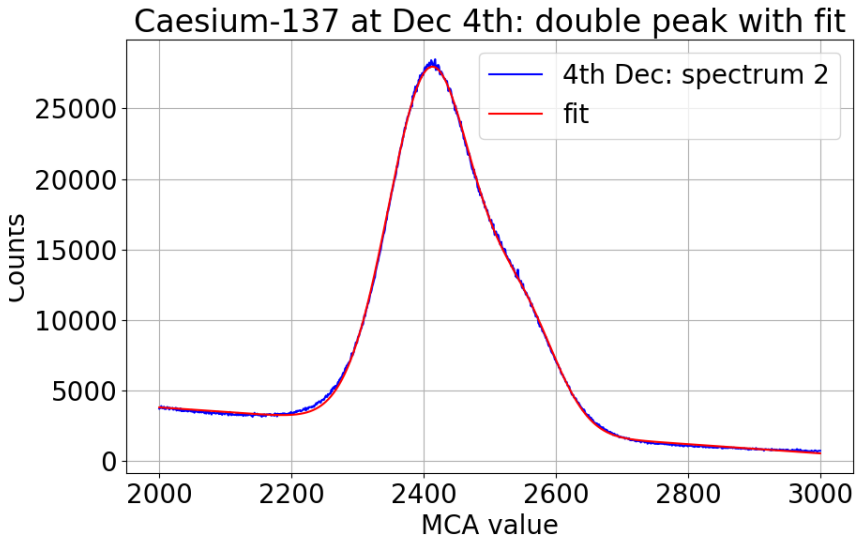

Figure 8.2.3.: Example of a measured ^{137}Cs spectrum including double Gaussian fit + linear background.

Fitted peak parameter for ^{207}Bi (MCA channel)							
Peak 1		Peak 2		Peak 3		Peak 4	
μ_1	σ_1	μ_2	σ_2	μ_3	σ_3	μ_4	σ_4
1871 ± 1	59 ± 2	2184 ± 11	72 ± 15	3865 ± 1	87 ± 1	4159 ± 1	83 ± 1
1861 ± 1	46 ± 1	2174 ± 4	52 ± 5	3855 ± 1	64 ± 1	4151 ± 1	65 ± 1
1869 ± 1	46 ± 1	2185 ± 5	53 ± 6	3872 ± 1	63 ± 1	4168 ± 1	66 ± 1
1857 ± 1	55 ± 1	2169 ± 8	61 ± 11	3841 ± 1	80 ± 1	4134 ± 1	79 ± 1
1834 ± 1	58 ± 1	2145 ± 7	62 ± 9	3802 ± 1	87 ± 1	4099 ± 1	76 ± 1
1863 ± 1	45 ± 1	2179 ± 4	52 ± 5	3860 ± 1	62 ± 1	4157 ± 1	65 ± 1
Mean peak values (MCA channel)							
$\bar{\mu}_1 = 1859 \pm 12$		$\bar{\mu}_2 = 2173 \pm 14$		$\bar{\mu}_3 = 3849 \pm 24$		$\bar{\mu}_4 = 4151 \pm 25$	

Table 8.2.: Fitted Peak values of recorded ^{207}Bi spectra.

Fitted peak parameter for ^{137}Cs (MCA channel)			
Peak 1		Peak 2	
μ_1	σ_1	μ_2	σ_2
2388 ± 1	74 ± 1	2533 ± 1	56 ± 1
2446 ± 1	82 ± 1	2599 ± 2	65 ± 1
2454 ± 1	78 ± 1	2605 ± 2	60 ± 1
2417 ± 1	65 ± 1	2555 ± 1	54 ± 1
Mean peak values (MCA channel)			
$\bar{\mu}_1 = 2426 \pm 26$		$\bar{\mu}_2 = 2573 \pm 31$	

Table 8.3.: Fitted Peak values of recorded ^{137}Cs spectra.

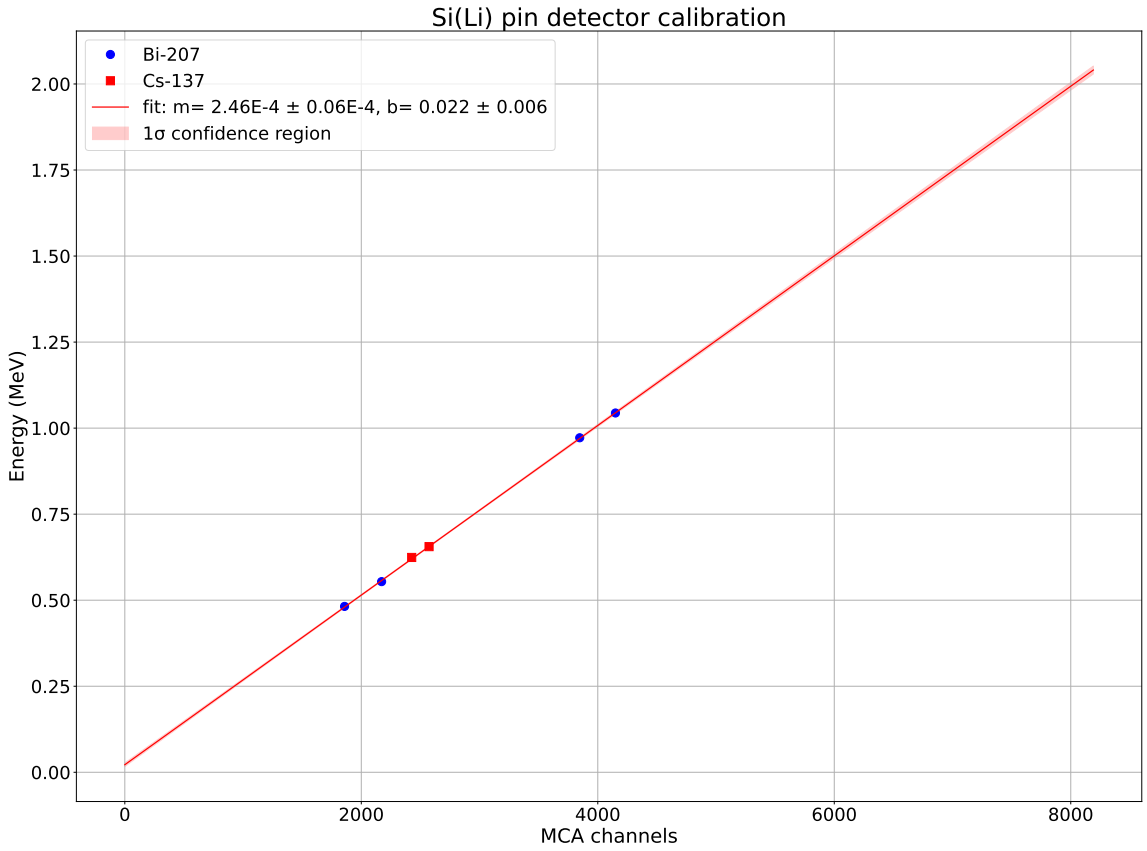

Figure 8.2.4.: MCA-Energy calibration for the Si(Li) pin detector using ^{207}Bi and validation with measured ^{137}Cs conversion electrons.

Although Si(Li) pin detectors are designed to work under vacuum conditions, since their detection principle operates independently of the surrounding medium, this detector does not seem to be vacuum operable. Figure 8.2.5 shows two different ^{90}Sr straight measurements using the vacuum chamber. Although the conditions and settings were identical, the spectrum behaves differently; the subsequent measurement on the right side seems to be compressed. Therefore, the investigated Si(Li) cannot be used for the main measurements.

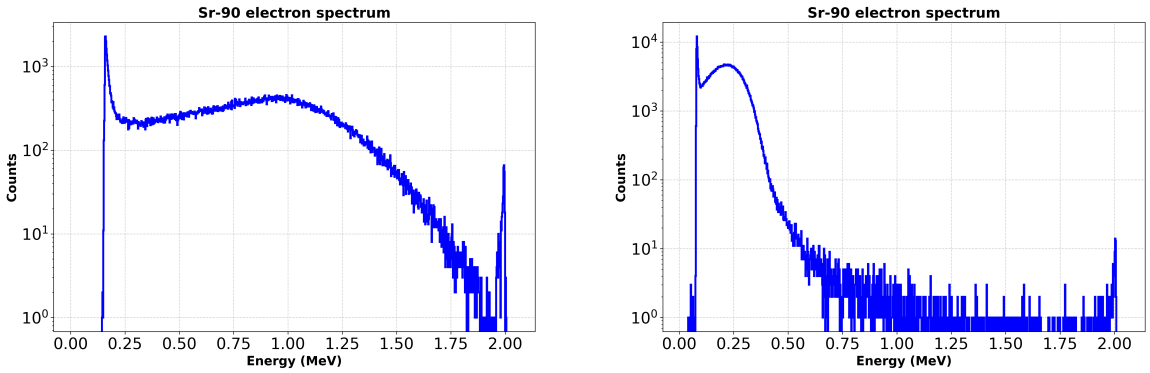

Figure 8.2.5.: ^{90}Sr spectra recorded by Si(Li) pin detector in vacuum. Left: measurement from March 2025. Right: measurement from May 2025.

8.3. Sodium iodide scintillator and PMT

Talium-doped sodium iodide crystals (NaI(Tl)) are commonly used as scintillator materials, whereby their doping with talium improves the energy resolution compared to pure sodium iodide scintillators. Due to its hygroscopic ability, NaI(Tl) can absorb water from the air, which leads to its decomposition. Therefore, this scintillator requires being hermetically packed to ensure a flawless operation. The used scintillator system consists of a cylindrical aluminum housing (56 mm diameter and 60 mm length) and is depicted in Figure 8.3.1. For scintillation light detection, the scintillator's back side is sealed not with aluminum, but with a light-guiding material, directly attached to the PMT.

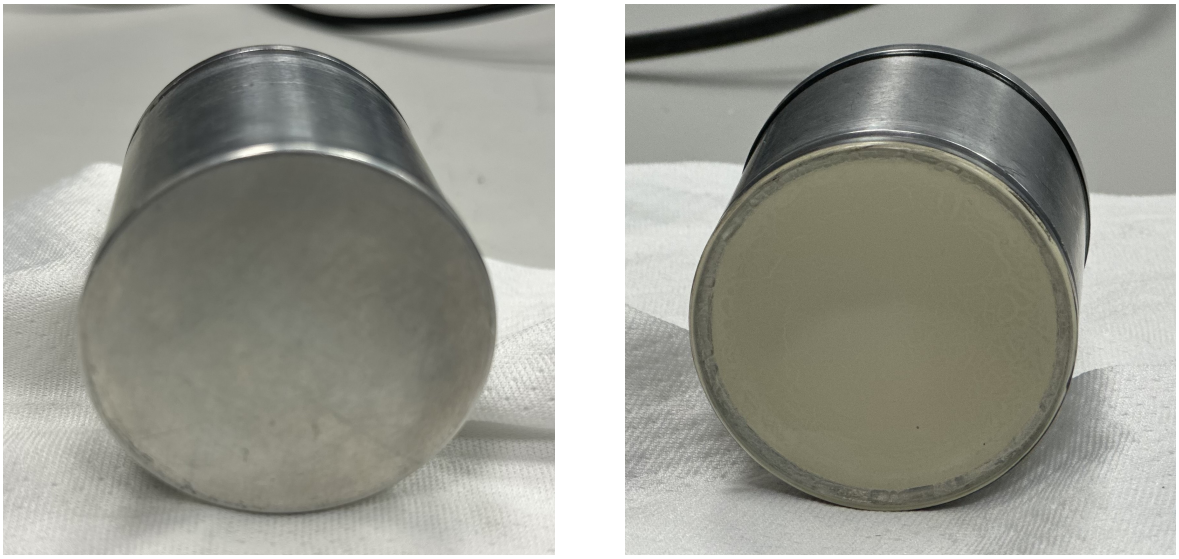

Figure 8.3.1.: NaI(Tl) scintillator with its housing. Left: front side. Right: back side.

The PMT is powered with a bias voltage of 2 kV, the amplification factor at the main amplifier is 2.5. A recorded, coarser binned and fitted ^{207}Bi spectrum is pictured in Figure 8.3.2. In contrast to the Si(Li) pin detector, which resolved the conversion electrons for the first two gamma lines, the first two gamma peaks themself are detected due to the higher detection efficiency of gammas, which also are the most intense radiations for ^{207}Bi. Further measurements are done for ^{137}Cs and ^{22}Na as well as ^{60}Co. Just as in the Bismuth spectrum, only gamma peaks can be identified, while no conversion electrons are detectable. All fitted peak results lead to a linear MCA-energy calibration curve with the fit parameters

$$\text{slope: } m = (3.6 \pm 0.3) \times 10^{-4} \tag{8.6}$$

$$\text{y-axis intercept: } b = -0.08 \pm 0.05 \ , \tag{8.7}$$

shown in Figure 8.3.3. The settings cover an energy range up to almost 3 MeV. The region of interest for ^{90}Sr is limited to 6500 MCA channels. The uncertainties on the slope are one magnitude bigger than the uncertainties for the Si(Li) detector calibration. Table 8.4 summarizes all measured peaks with their corresponding literature values E_{lit}, and the calculated energies E_{meas} using the calibration function are added in the last column. All E_{meas} agree well with the literature values. The calculated

uncertainties are mainly affected by the uncertainty of the y-axis intercept and might be overestimated.

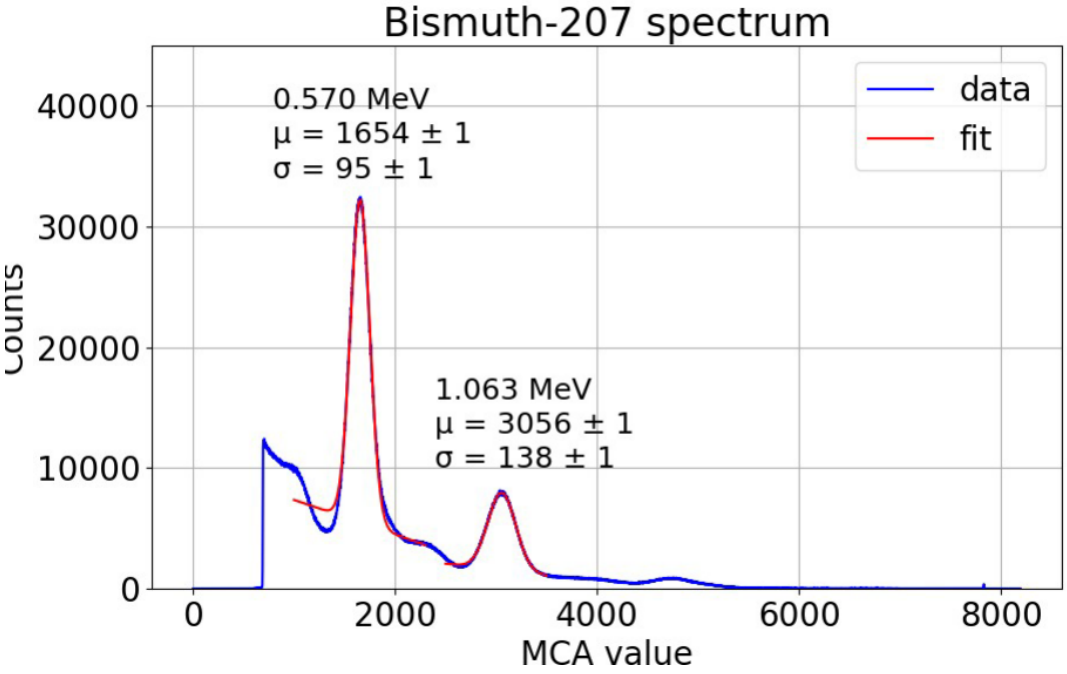

Figure 8.3.2.: Recorded ^{207}Bi spectrum using NaI(Tl) scintillator and PMT

Source	Fit parameters (MCA channel) Peak μ	Width σ	Literature energy E_{lit} (keV)	Calculated energy E_{calc} (keV)
^{207}Bi	1654 ± 1	95 ± 1	569.698	516 ± 71
^{207}Bi	3056 ± 1	138 ± 1	1063.656	1020 ± 110
^{137}Cs	2076 ± 1	114 ± 1	661.657	667 ± 80
^{22}Na	1545 ± 1	91 ± 1	511.000	476 ± 69
^{22}Na	3801 ± 1	144 ± 1	1274.540	1290 ± 130
^{60}Co	3478 ± 1	136 ± 1	1173.217	1170 ± 120
^{60}Co	3935 ± 1	132 ± 1	1332.492	1340 ± 130

Table 8.4.: Fitted Gamma peaks of recorded spectra of ^{207}Bi, ^{137}Cs, ^{22}Na and ^{60}Co for sodium iodide scintillator. The last column lists the calculated energies E_{calc} using the calibration function. For the literature values E_{lit}, see Chapter 2.3.1.

As already mentioned above, a recording of conversion electrons with the used detector is barely possible, although sodium iodide is also sensitive to charged particles. The back side, consisting of the light guide material, must be attached to the PMT so that the aluminum side seals the collimator chamber. Consequently, the conversion electrons have to traverse the aluminum before hitting the NaI(Tl) crystal. The electrons lose a fraction of their energy inside the aluminum due to radiation losses. Figure 8.3.4 presents the energy loss of electrons in aluminum as a function of the electron energy. Conversion electrons with energies around 1 MeV are not able to hit the scintillator

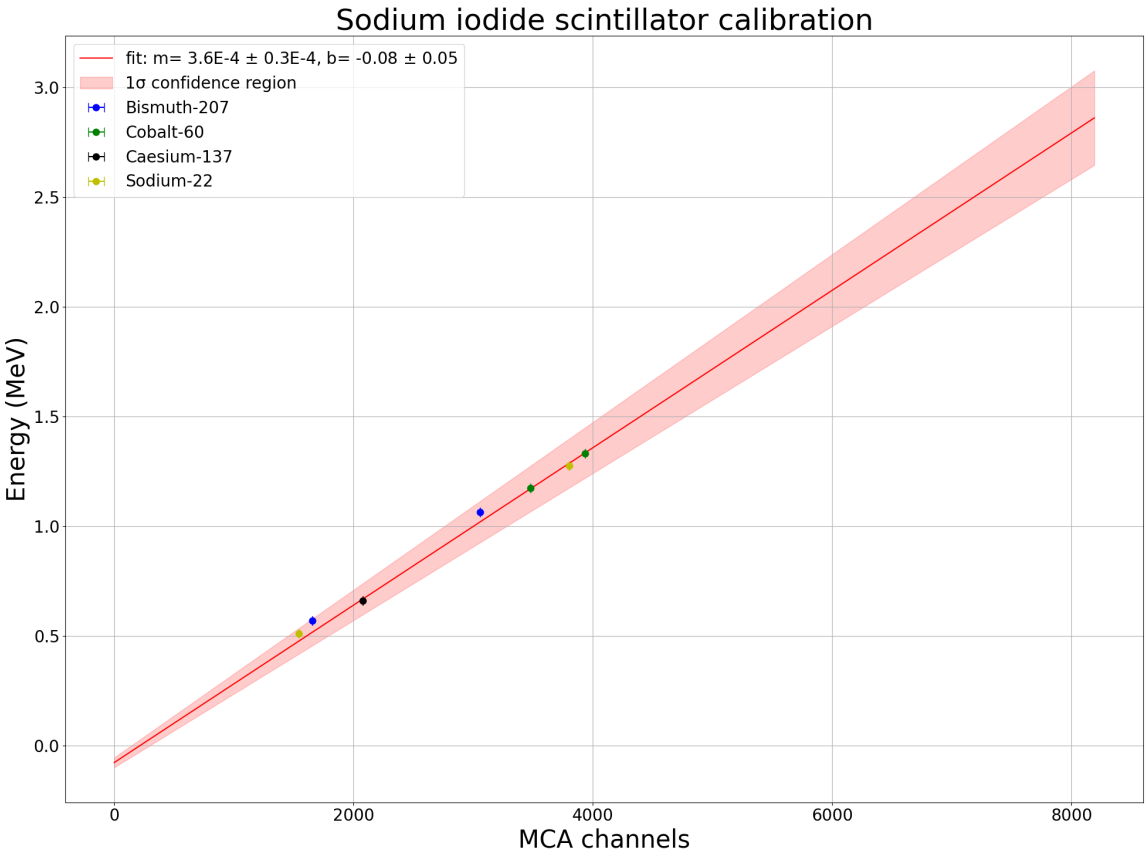

Figure 8.3.3.: MCA-energy calibration for sodium iodide scintillator.

for aluminum thicknesses greater than 2.5 mm. Hence, the aluminum shielding significantly reduces the energy of incoming electrons, disqualifying this NaI(Tl) scintillator for investigation of the beta spectrum of ^{90}Sr.

8.4. BC-408 and PMT

At last, another calibration was performed using BC-408, a polyvinyltoluene-based plastic scintillator by Saint-Gobain with a density of 1.032 g/cm^3. It is sensitive to charged particles, suitable for beta spectroscopy. In contrast to a sodium iodide scintillator, whose sensitivity is optimized for gammas, BC-408 is only sensitive to low-energetic photons below 100 keV, and operable in vacuum [Sai16]. This scintillator, shown in Figure 8.4.1, has a diameter of 57.15 mm and a thickness of 1 cm and fits perfectly on the PMT. It allows an electron detection with kinetic energies up to 1.86 MeV [2]. This does not cover the whole range of the ^{90}Sr beta spectrum, but the important energies. Since the scintillation light is emitted isotropically, the side surface is covered with polytetrafluoroethylene (PTFE) to reduce photon escapes.

[2] This estimation is based on a stopping power of 1.802 MeVcm^2/g for 1.8 MeV electrons, based on ESTAR database [Ber+].

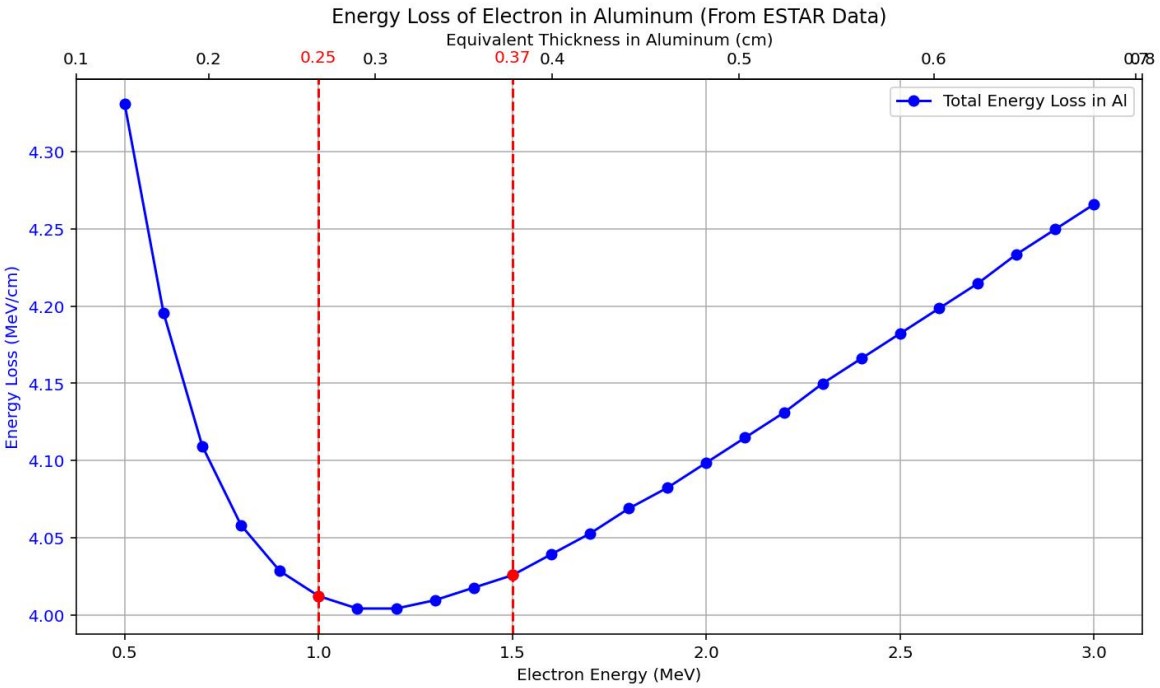

Figure 8.3.4.: Energy loss of electrons in aluminum. The required stopping power is extracted from the ESTAR database [Ber+, ESTAR].

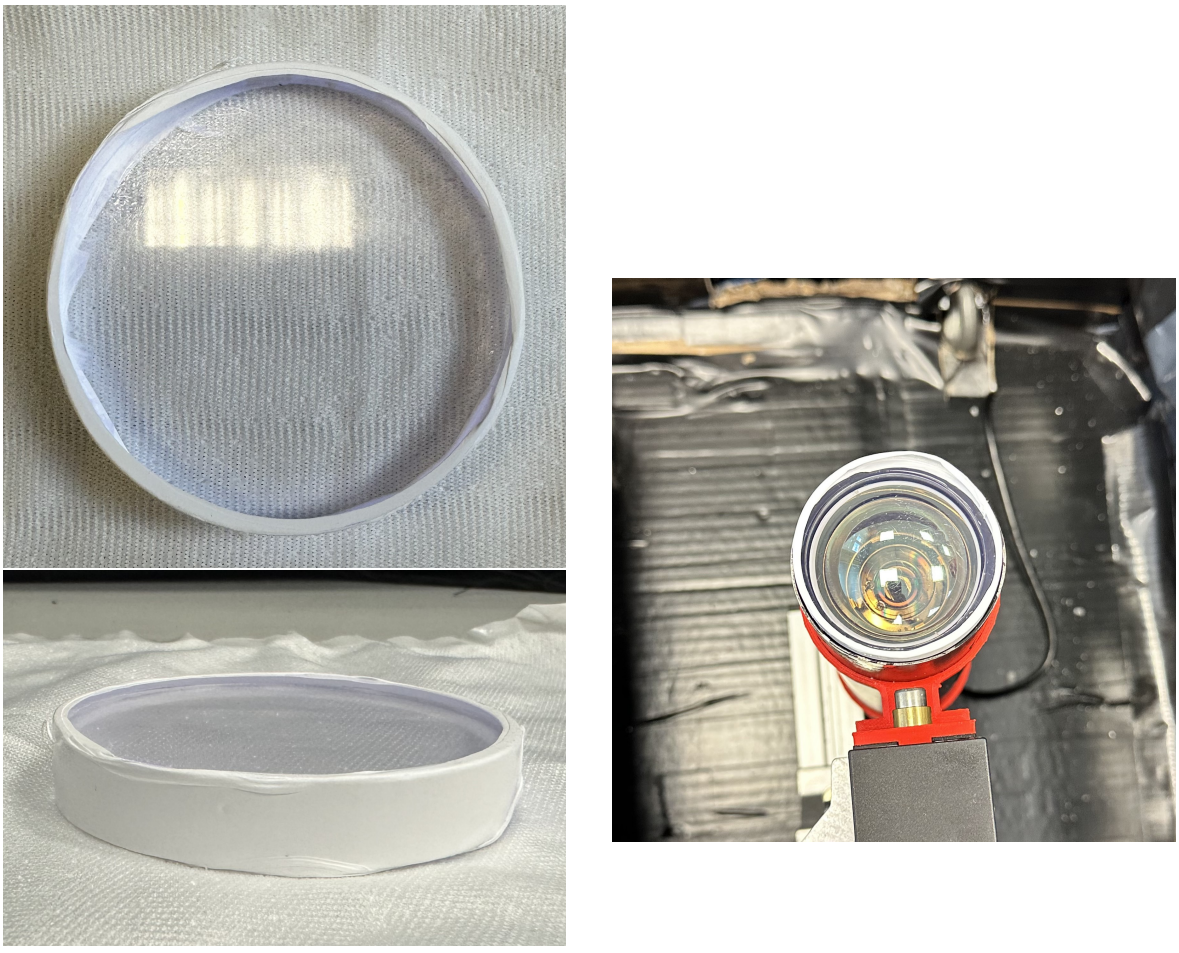

Figure 8.4.1.: BC-408 scintillator. Left: front and side view. Right: placement on PMT.

The bias voltage applied to the PMT is still 2 kV, but a higher gain factor (6.5 instead of 2.5) is set for the BC-408 measurement. There are three peaks visible when recording a ^{207}Bi spectrum, depicted in Figure 8.4.2. The first (second) peak corresponds to the K-shell (L-shell) conversion electron of the first gamma line, having a characteristic energy of 481.7 keV (553.8 keV). These two peaks are fitted together with a double Gaussian with a linear background. The third peak corresponds to the 975.7 keV K-shell conversion electron of the 1063.7 keV gamma line (975.7 keV and 1047.8 keV). Hence, one obtains a linear fit shown in Figure 8.4.3. The uncertainties are in the same magnitude as for the sodium iodide scintillator. The fit parameters are

$$\text{slope: } m = (2.45 \pm 0.10) \times 10^{-4} \tag{8.8}$$

$$\text{y-axis intercept: } b = 0.16 \pm 0.03 \ . \tag{8.9}$$

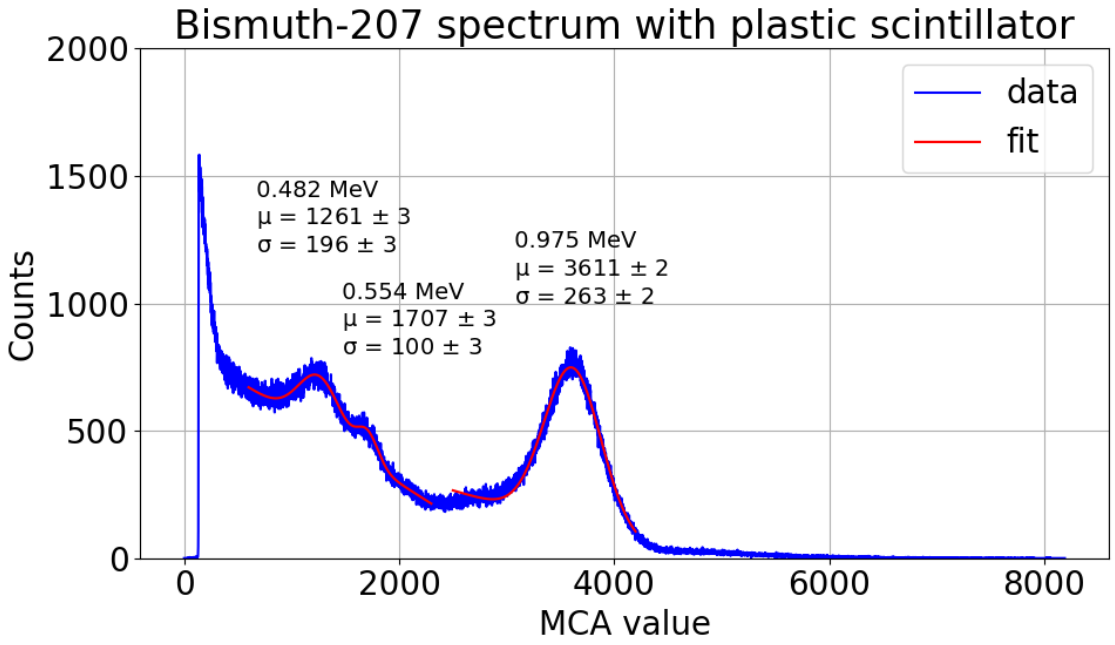

Figure 8.4.2.: ^{207}Bi spectrum using BC-408 scintillator, including fits.

Besides ^{207}Bi, spectra were also recorded for ^{60}Co and ^{22}Na. Although there are low-energy conversion electrons for ^{60}Co below100 keV, they are not detected; instead, Compton edges can be identified (see Figure 8.4.4). These energies can be calculated by

$$E_c = 1 - \frac{1}{1 + \dfrac{2E_\gamma}{m_e c^2}} \tag{8.10}$$

and occur when the emitted photons with energy E transfer the maximum possible energy E_c to an electron; hence, there is a characteristic drop behind a Compton edge. The Compton edge is fitted using a combination of a Gaussian function and the

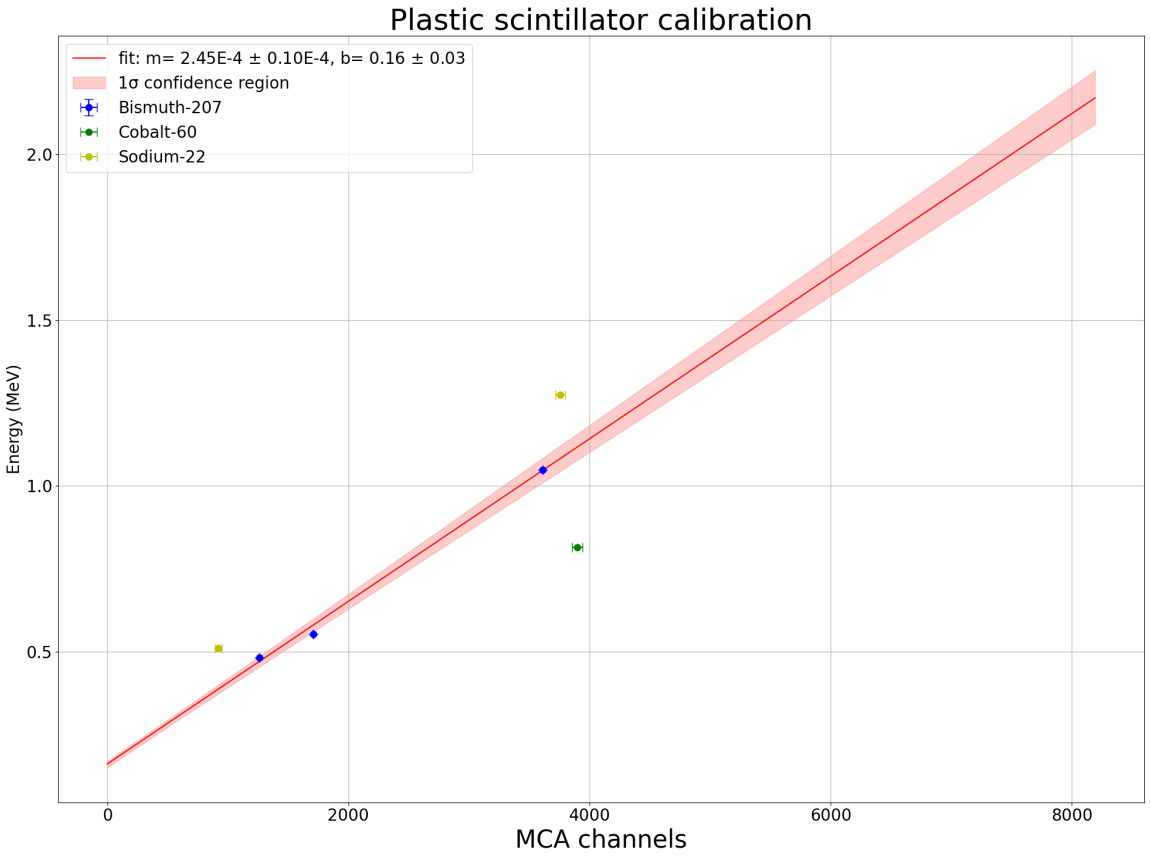

Figure 8.4.3.: MCA-Energy calibration for BC-408 scintillator.

complementary error function [SDA20]

$$f(E) = \alpha_1 \cdot \mathrm{erfc}\left(\frac{E - E_{\mathrm{CE}}}{\sqrt{2}\sigma}\right) + \beta_1 \exp\left[\frac{(E - E_{\mathrm{CE}})^2}{2\sigma^2}\right] \ , \tag{8.11}$$

with

$$\alpha_1(E) = \frac{1}{2}\left[a(E^2 + \sigma^2) + bE + c\right] \ , \tag{8.12}$$

$$\beta_1(E) = \frac{-\sigma}{\sqrt{2\pi}}\ a(E + E_{\mathrm{CE}}) + b) \tag{8.13}$$

and the complementary error function

$$\mathrm{erfc}(E) = 1 - \frac{2}{\sqrt{\pi}} \int_x^E \exp(-x^2)\,\mathrm{d}x \ . \tag{8.14}$$

The fit parameters are $a,\ b,\ c,\ \sigma$ and the Compton edge energy E_{CE}. The same function is used for ^{22}Na. However, despite having low fit uncertainties, they strongly depend on the fitted interval region and vary too much. Therefore, all Compton edges are excluded and only ^{207}Bi contributes to the MCA calibration. The fitted peak values of the Compton edges (^{60}Co and ^{22}Na) also do not agree with the calibration fit (Figure 8.4.3).

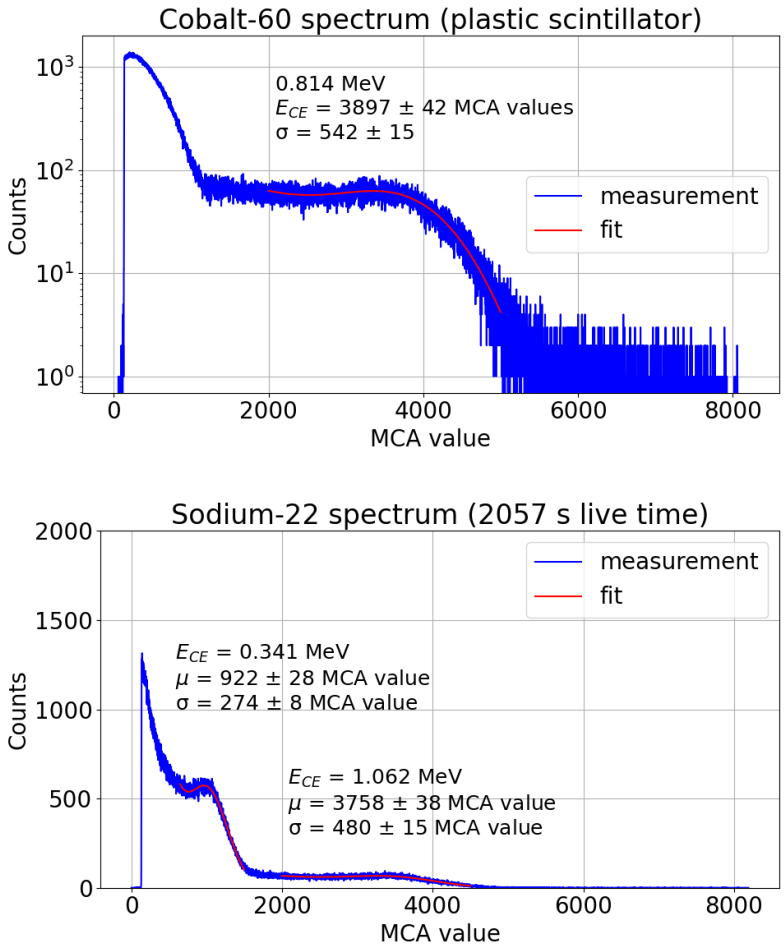

Figure 8.4.4.: ^{60}Co (top) and ^{22}Na (bottom) spectrum using BC-408 scintillator, including fits for Compton edges.

8.5. Conclusion of the MCA-energy calibration

The MCA exhibits a linear dependence on the incoming signal amplitude, whose correlation with the energy of detected particles leads to a linear conversion function between the MCA channel and energy. Three different detectors verified this. The investigation of the Gaussian peaks shows the energy resolution

$$R = \frac{\mathrm{FWHM}}{E} = \frac{2\sqrt{2\ln 2}\,\sigma}{E} \tag{8.15}$$

for the Si(Li) pin detector (between 3.6 and 7.3 %), followed by the NaI(Tl) scintillator with resolutions between 7.8 and 13.9 %. The BC-408 detected conversion electrons only with resolutions below 13.9 %. Although having the best energy resolution, the investigated Si(Li) pin detector cannot be used for the following ^{90}Sr measurements. Furthermore, a proper detection of beta particles with the NaI(Tl) scintillator is unfeasible due to its aluminum-made front side, which significantly reduces the energy of electrons passing through. Therefore, the BC-408 scintillator, despite having the worst energy resolution of all three detectors, is chosen for the upcoming determination of beta electrons inside the vacuum chamber.

9. Dark measurements and background estimation

After selecting the BC-408 plastic scintillator with PMT as the most appropriate detector system for the setup, the consistency and influence of background signals are examined as the next step. This is important to create a background model to extract the net signals.

9.1. Dark measurements and consistency

Since both the BC-408 scintillator and the PMT are placed behind the collimator chamber, they are covered with a black blanket to reduce the noise by surrounding light sources. The applied high voltage of the PMT is identical to calibration measurements (2000 V), and the baseline of the receiving signals is checked using an oscilloscope to identify the threshold conditions. The baseline ends at an amplitude of approximately 100 mV, which also agrees with the baseline during the calibration. Therefore, the MCA threshold is set to 0.120. All measurements lasted 600 s.

Dark measurements are performed under four different light conditions:

- Ceiling lights on and blinds open
- Ceiling lights on and blinds closed
- Ceiling lights off and blinds open
- Ceiling lights off and blinds closed.

All global spectra follow a similar pattern. The influence of light dominates in the low channel region. The ceiling lights continuously create light with a higher intensity than the incoming daylight. Additionally, the daylight depends on the respective weather conditions. Therefore, the ceiling lights cause the most noise, resulting also in higher count rates (Table 9.1) and higher uncertainties due to the Poisson-like character of the counting experiment.

Light condition	Count rate N/s (counts/s)	Count rate error $\sqrt{N}/s$ (counts/s)
Lights on + blinds open	294	18
Lights on + blinds closed	180	14
Lights off + blinds open	15	4
Lights off + blinds closed	5 till 6	3

Table 9.1.: Livetime dark count rates for different light conditions for a small BC-408 plastic scintillator. Applied bias voltage to PMT: 2000 V.

The influence of external light explains the low-channel background, whose respective energies lie below the threshold energy required to produce Cherenkov photons later in PMMA. Hence, this part can be neglected in future measurements.
However, there are additional signals within the whole range. One reason is the influence of cosmic particles. These particles can deposit a tiny fraction of their energies in the scintillator, leading to additional scintillation light.
Table 9.2 contains the dark count rate for a round BC-408 scintillator with a diameter of 57.15 mm, taken on different days. The average dark count rate does not significantly increase above 8.7 ± 0.1 counts per second, compared to the smaller scintillator (5 to 6 counts per second). The background is stable, providing a good base for reproducible measurements.

Livetime (s)	Total counts	Count rate (counts/s)
113	880	7.79 ± 0.27
106	790	7.45 ± 0.27
600	5551	9.25 ± 0.13
600	5176	8.63 ± 0.12
Weighted mean count rate: (8.7 ± 0.1) counts/s		

Table 9.2.: Dark measurements with the big BC-408 scintillator, no lights and blinds down. Applied bias voltage to PMT: 2000 V.

9.2. Determination of background level

For the determination of the background level, the dark measurement has to be approximated by creating an appropriate fit function. Since the recorded noise does not behave like a known distribution, a polynomial approach

$$f(x) = \sum_{\mathrm{k}=0}^{\mathrm{n}} c_{\mathrm{k}}\, x^{\mathrm{k}} \tag{9.1}$$

of order n with constant coefficients c_{k} is assumed. The fit is then processed using the function '*polyfit*' from Python's NumPy library. Afterwards, the mean squared error (MSE) and the R^2 value are calculated to compare the quality of the fits with each other. Fluctuations are crucial for the background estimation. The MCA consists of 8192 channels and can process inputs between 0 and 10 volts. This implies that one MCA channel covers a range of 1.2 mV and can cause fluctuations, especially in the low-energy region, where the most noise appears. Therefore, weights w_{i} are included using the inverse standard deviations σ_{i} of the data points, which is the square root of the counts for a Poisson distribution, and hence

$$w_{\mathrm{i}} = \frac{1}{\sigma_{\mathrm{i}}} = \frac{1}{\sqrt{N_{\mathrm{i}}}}\ . \tag{9.2}$$

The energy region below 0.75 MeV contains the most noise, and thus the background has to be determined properly in this region. For energies above 0.75 MeV, the dark

counts do not significantly contribute anymore. The noise increases again at the high-energy end, corresponding to the highest MCA channel, which is the overflow bin. Figure 9.2.1 shows the background modeling for polynomials of 2nd to 8th degree for four different binnings. The MCA values are converted into energy by using the MCA-energy calibration parameters from the Equations 8.8 and 8.9 for the BC-408 scintillator in Chapter 8.4. In the top left, there is the unbinned data. This is a fluctuation-dominated distribution that cannot be properly modeled below 1 MeV. A bin width of 16, as shown in the diagram above right, looks promising for the fourth-, the seventh-, and the eighth-degree polynomial fits. Both R^2 values lie above 86 % and have the best description in the low-energy end, while the seventh-degree polynomial underestimates that noise. A better approximation for this region is done using a fourth-degree polynomial and a bin width of 32, presented in the bottom left, despite having a lower R^2 value. There are bigger deviations for energies above 2 MeV, but since such energies cannot be investigated with the BC-408 due to its small thickness (see Chapter 8.4), this can be neglected. One can also use a binning of 64, which also describes the low-energy background well using a polynomial of fourth order. Some higher polynomials (6th, 7th, and 8th order) have slightly better fit values, but they can tend to overfit the background. Compared to 32 data points per bin, there is no significant improvement. A rougher binning is not recommended, since it can cause information loss.

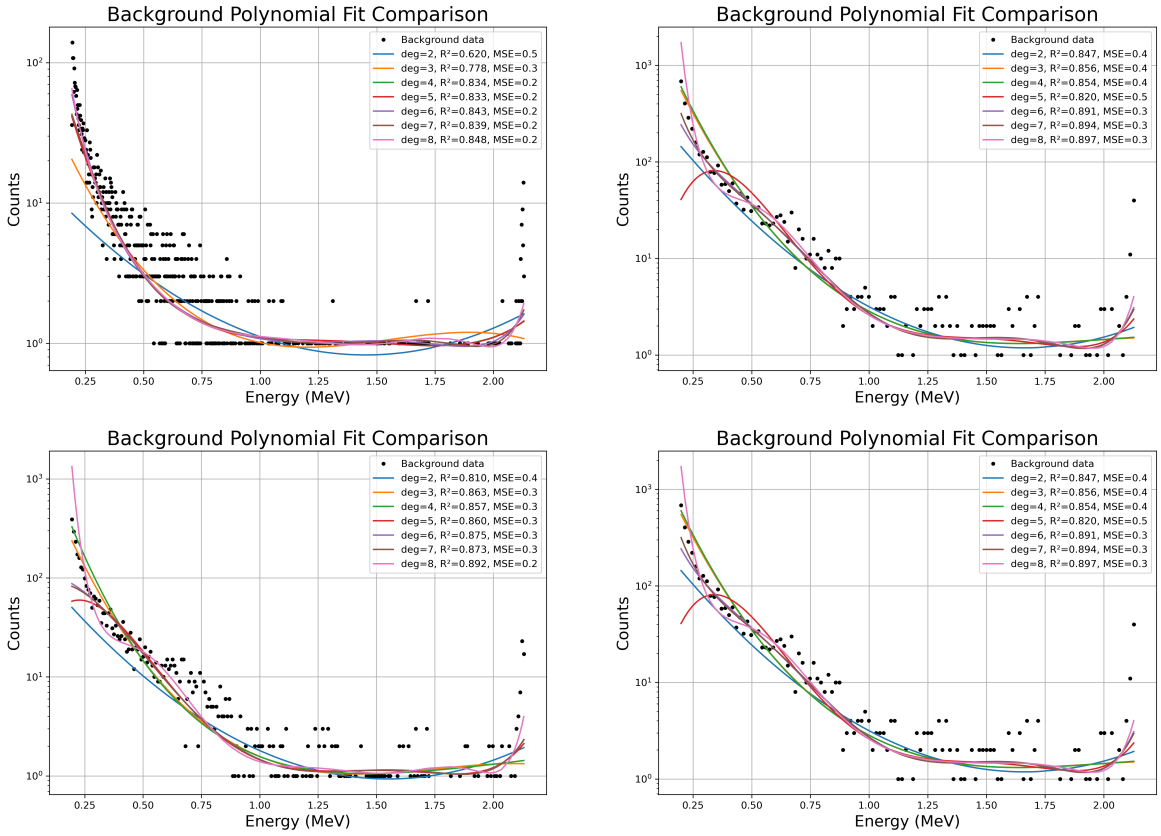

Figure 9.2.1.: Background modeling using different polynomial functions for different bin sizes. Top left: unbinned data, top right: 16 MCA channels per bin. Bottom left: 32 MCA channels per bin, bottom right: 64 MCA channels per bin.

After selecting the fit model, the net signal can be obtained. In the case of the above data set, a bin width of 32 and a fourth-order polynomial result in the net data presented in Figure 9.2.2. The net spectrum ends slightly above 1.75 MeV, which matches the detection limit of the used detector, so that the peak above 2 MeV can be verified as additional noise. The net spectrum agrees with the beta spectrum of ^{90}Y (Figure 9.2.3). The contribution below 0.52 MeV cannot be absolutely assigned to the ^{90}Sr part, since according to 9.2.3, ^{90}Sr provides smoother falling edge below 0.5 MeV. Some ^{90}Sr betas may be recorded, but the background is underestimated. This underestimation is then influenced by fluctuations. Another measurement series shows no big peak below 0.25 MeV, which reinforces the assumption that this peak is noise-dominated.

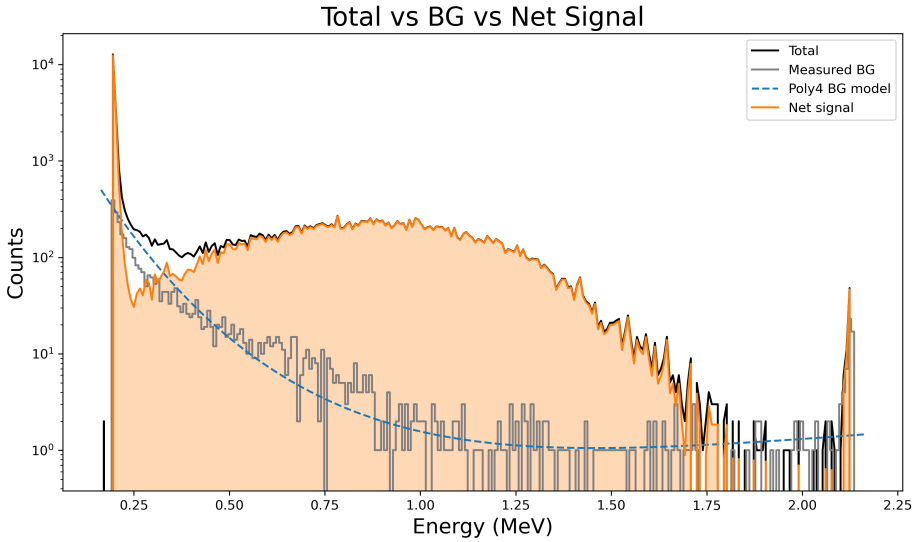

Figure 9.2.2.: Example of the background subtraction and resulting net spectrum.

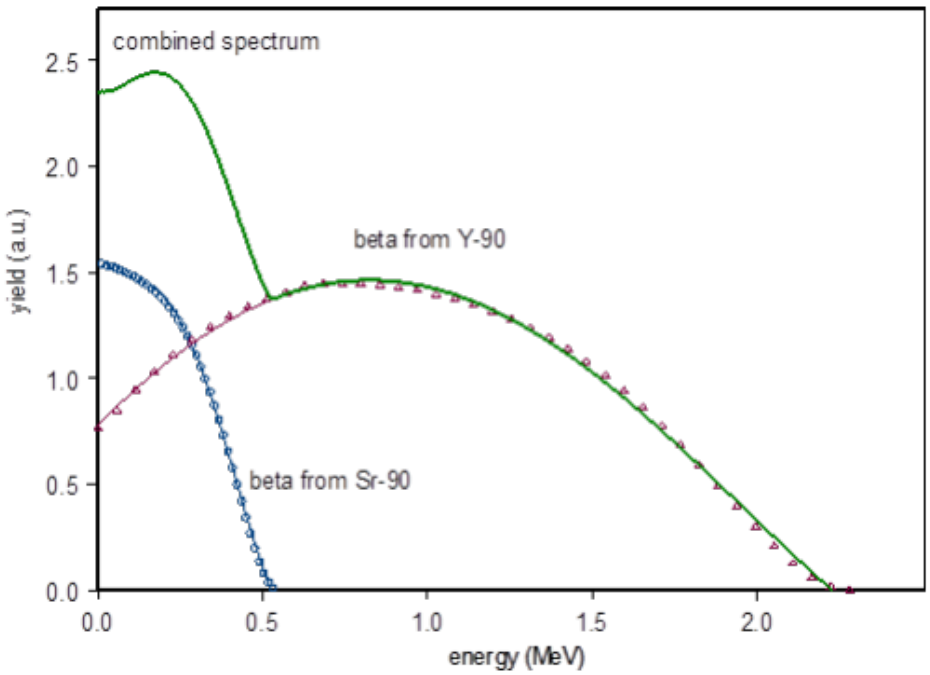

Figure 9.2.3.: Combined beta spectrum of ^{90}Sr and its daughter nucleus ^{90}Y [Arf+15].

10. Geometrical modifications of the Geant4 setup

The Geant4 configuration used in Chapter 7 describes the experiment only in simplified form. In this section, the Geant4 simulation will be modified by investigating the experimental setup in more detail.

10.1. Determination of the magnetic field inside the vacuum chamber

A real dipole magnet not only creates a homogeneous magnetic field in the area between both coils, but also an additional inhomogeneous magnetic field around the homogeneous section. Previous measurements already investigated the profile for 40 mT and 60 mT fields, see [Koo23, Chapter 4.2.3]. However, these measurements were taken outside the vacuum chamber, and hence, potential influences of the aluminum walls as well as the mu metals are neglected.
Therefore, the magnetic field inside the magnet chamber was checked with a tangential probe and read out by a microvoltmeter, both manufactured by Elwe Didactic GmbH. The resolution of the voltmeter is 0.1 mT. Since the probe's stalk is shorter than the magnet chamber, it is not possible to measure the whole field from the source chamber's side. For measurements from the source chamber's side, the probe is fixed on the source holder, while the probe was fixed on a tripod when doing measurements from the other side. Due to the need for manual positioning, the misplacement of the probe sensor is estimated to be ±1 mm. The step size is 3 mm when using the stepping motor, otherwise 5 mm. The small mu-metal attached to the source holder's arm is neglected in these measurements, but will be considered in the extrapolation. Afterwards, the measured voltages are converted into millitesla by using the following calibration curve of the voltmeter:

$$\frac{B}{\mathrm{mT}} = 1.044 \cdot \frac{U}{\mathrm{mV}} \ . \tag{10.1}$$

Here, the error on B is $\sigma_B[\mathrm{mT}] = 1 \pm 1.5\,\%$.

The measured field map for 20 mT, including a linear interpolation for visualization, is shown in Figure 10.1.1. Further magnetic field measurements for 10, 30, 40 and 60 mT are included in appendix A.2. In case of the 10 mT magnetic field, it was not measured but calculated using the linear behavior between the bias current for the magnet and the homogeneous field region. For this approximation, the mean of all other magnetic fields was calculated. The coordinate system used matches the coordinate system used in the Geant4 simulations (xy plane, with the origin at the center of the magnet). By considering a magnetic field as homogeneous for deviations less than 10 %, all fields

are indeed homogeneous around the center. But contrary to simulations, a significant surrounding rest field is measurable, since the used mu metal tubes are open on two opposite sides, resulting in a lower bending radius. Furthermore, the peak values are slightly higher (Table 10.1) than the designated fields. Since even slight differences in the magnetic field can cause deviations from several keV, a field value of 23 mT cannot be assumed as 20 mT. Therefore, the magnetic field in the Geant4 configuration is enlarged and now considered inhomogeneous.

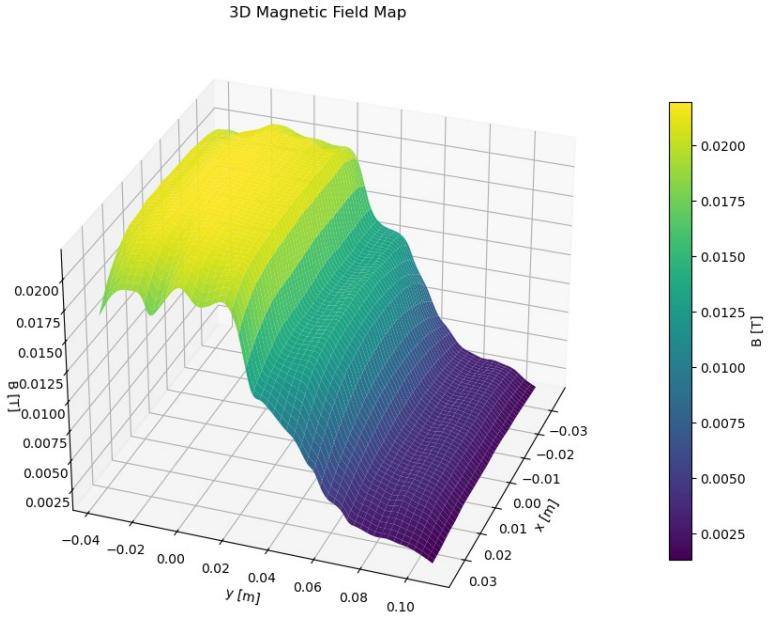

Figure 10.1.1.: Measured 20 mT magnetic field with linear interpolation for visualization. Scales are given in T and m.

Desired magnetic field (mT)	Measured magnetic field peak (mT)
20	21.9
30	33.8
40	41.7
60	68.8

Table 10.1.: Measured peak field values.

10.2. Source position and distance to the detector

The bare ^{90}Sr source is not located directly next to the small mu metal, but inside a cylindrical source box that shields the environment from emitting beta particles. The beta emitter is placed 32 mm inside the source, while the emitted electrons then pass through the 2 mm diameter opening. This implies a larger distance between the source and the detector, and hence, an increase in the interaction probability with air molecules. On the other hand, the smaller opening could improve the energy resolution due to the reduction of angular dispersion. Moreover, further adjustments also allow

for moving the source closer to the wall of the source chamber, resulting in a distance reduction of 70 mm on the experiment's side.

10.3. Modified Geant4 setup

All the adjustments above are taken into account for creating the following Geant4 setup, shown in Figure 10.3.1, which agrees with the dimensions of the experimental setup. The origin still lies at the center of the magnet, and the PMMA corresponds to the scintillator in the experiment. First and foremost, a source tube is added with the same dimensions as the experimental one. The point-like particle gun (red dot) is placed 32 mm inside the box, whose round 2 mm diameter opening is smaller than the Mu-metal cross section, reducing the angular spread down below 2°. It is assumed that the box shields perfectly; hence, all particles hitting one of the walls are killed, including their secondary particles. The pivot point, meaning the end of the 68 mm long small Mu-metal tube, is fixed along the x-axis onto −34.5 mm. Finally, there is also a change in the magnetic field area (pink part). While the old simulation just includes a small, idealistic homogeneous field, the new field is considered inhomogeneous. Its length along the x-axis is now 205 mm instead of 60 mm and encompasses the entire magnetic field chamber, expecting a stronger influence, and hence, a larger bending.
Since the magnetic field cannot be considered homogeneous anymore, the field must be computed for each position now. This implies the requirement of a field interpolation and extrapolation, based on the measured field maps. The numerical calculation script is adjusted similarly.

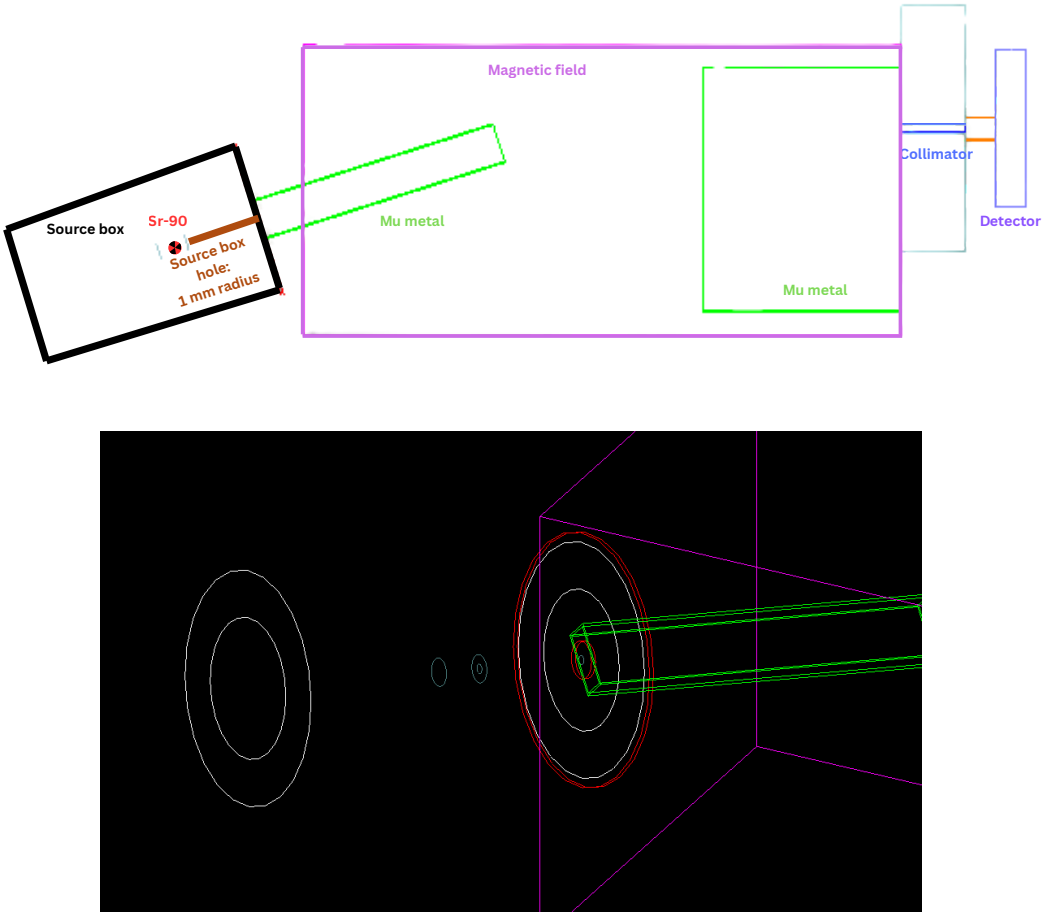

Figure 10.3.1.: Modified Geant4 setup. Top: side view. Bottom: Source box. Electrons can only exit the source box through an opening with a radius of 1 mm.

11. Scan measurements

This chapter contains scan measurements for both experiment and simulation, in which measurements are taken for different source positions. In contrast to investigating specific energies by calculating the source positions, these scan measurements do not require any trajectory calculations in advance, but are based on the experimental positions. Hence, a proper magnetic field approximation is not required.
For these measurements, the linear offset, meaning the position along the y-axis of the source with respect to the center of the collimator, is varied in steps of 5 mm. The rotary stage's angle θ is changed in steps of 10°. The corresponding bending angle φ can be calculated using

$$\varphi = \arctan\left(\frac{r\sin\theta}{l + r\cos\theta}\right) = \arctan\left(\frac{42 \cdot \sin\theta}{93 + 42 \cdot \cos\theta}\right) \tag{11.1}$$

with measured parameters $r = (42.0 \pm 0.1)\,\text{mm}$ and $l = (93.0 \pm 0.1)\,\text{mm}$ and are listed in Table 11.1. The corresponding uncertainties σ_φ are calculated via the Gaussian error propagation. The bias voltage for the PMT is set on 2 kV for all following measurements. In addition, the analysis of the experimental data is done using a bin size of 64 MCA channels. This corresponds to an amount of 128 bins. The aim of these measurements is the global investigation of the energy distribution of the electrons reaching the scintillator after passing the collimator. The comparison between experiment and simulation will help to further optimize the simulations, as it provides an initial assessment of the magnetic field estimation.

Rotary stage angle θ (°)	σ_θ (°)	Bending angle φ (°)	σ_φ (°)
0.00	0.02	0.000	0.006
-10.00	0.02	3.107	0.006
-20.00	0.02	6.189	0.006
-30.00	0.02	9.220	0.006
-40.00	0.02	12.171	0.006
-50.00	0.02	15.009	0.006
-60.00	0.02	17.696	0.005
-70.00	0.02	20.183	0.005
-80.00	0.02	22.412	0.004
-90.00	0.02	24.305	0.004
-100.00	0.02	25.762	0.003
-110.00	0.02	26.652	0.002

Table 11.1.: Rotary stage angle θ and its corresponding bending angle φ, used for the scan measurements.

11.1. Investigation of the experimental electron spectra

Before the experimental data is compared with Geant4 simulations, the experimental data is investigated in detail.

First tests with 5 mm collimator opening

First, scan measurements are performed for a 5 mm collimator opening for 100 s. The applied current to the magnet coils is 0.775 A, providing a core field of 20 mT. Figure 11.1.1 depicts the resulting net signals after subtracting the background for rotary stage angles of -40, -60, -80, and $-110°$ (-45, -65, -85, and $-105°$ for 15 mm offset due to the measurements taken). The minus sign in θ only means the orientation from the zero point, since it rotates anti-clockwise. Signals corresponding to energies between 0.6 and 1.90 MeV are detected. Each spectrum consists of only one distributed peak; no bump is observed for the background-dominated low-energy region. This indicates a good agreement with the background model. A reduction in the angle causes a shift in the spectrum toward lower energies for all linear offsets. This agrees with the expectation, since low-energy particles bend more in a magnetic field. Depending on the linear offset, the total number of observed electrons varies for different angles.

In contrast to 20 mT, increasing the core magnetic field up to 30 mT (= 1.450 A current for the magnet) results in a shift to higher energies, shown in Figure 11.1.2. There are no signals detected corresponding to electrons lower than 1 MeV. Furthermore, larger angles become more important than for a smaller field. For an offset of at least 10 mm, the most dominant distribution in terms of detected counts is achieved at a bending angle $\varphi = 25.8°$, while a bending angle of 17.7° is the most dominant for the 20 mT field.

However, in each case, the energy spread is very high, extending in the range of a few hundred keV. This implies that the majority of incoming electrons do not hit the scintillator perpendicularly, which significantly increases the energy distribution and leads to poorer energy resolution. To verify the electrons that hit the scintillator perpendicularly, the peak ratio PR is determined. A PR calculation requires that, in addition to a background measurement, each measurement series must further include a straight measurement without an applied magnetic field. Either all measurements must have the same time duration, or a scaling is necessary. At first, the investigated spectrum is fitted with a Gaussian function

$$f(x;\mu,\sigma) = \frac{1}{\sigma\sqrt{2\pi}} \exp\left(-\frac{1}{2}\frac{(x-\mu)^2}{\sigma^2}\right) . \tag{11.2}$$

Afterwards, the fitted peak amplitude A_{fit} at the energy μ is divided by the amplitude $A_{\text{straight}}(\mu)$ of the corresponding straight measurement at energy μ:

$$\text{PR} = \frac{A_{\text{fit}}(\mu)}{A_{\text{straight}}(\mu)} . \tag{11.3}$$

The straight measurement gives the entire observable beta spectrum of the source without any filtering. After switching on the magnetic field and changing the source

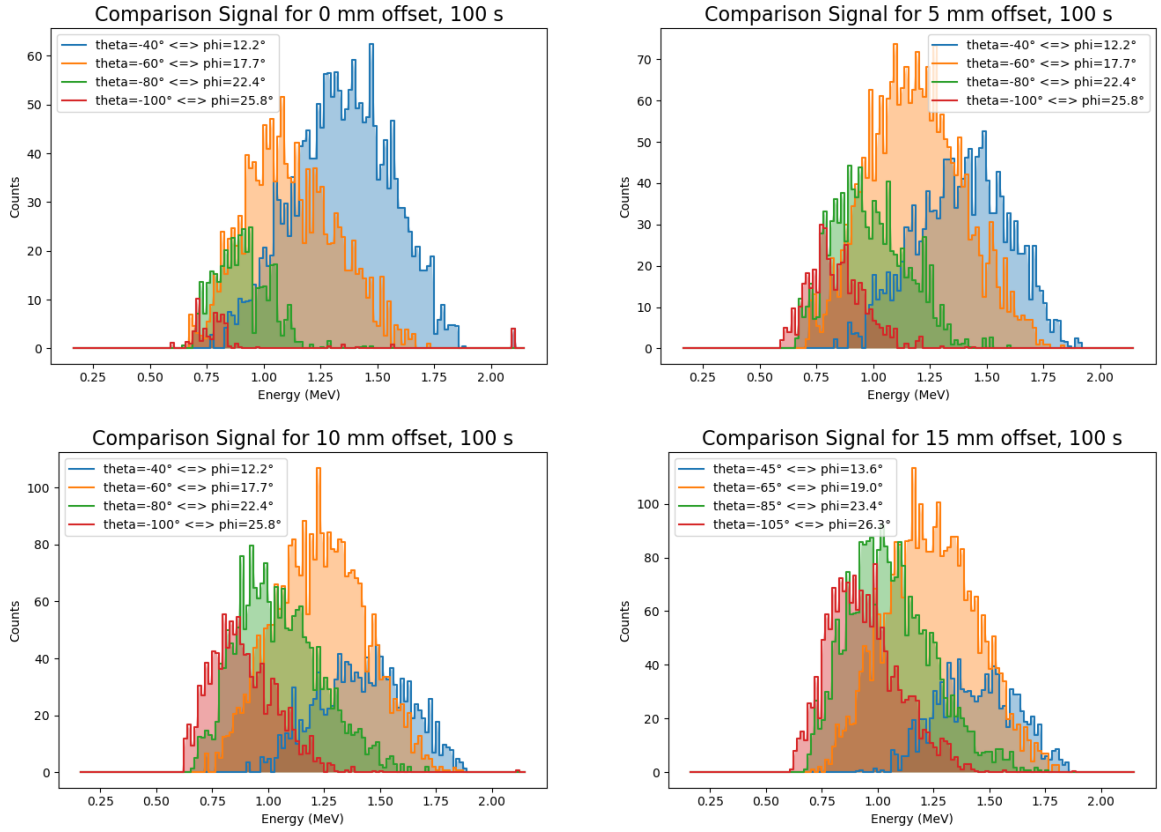

Figure 11.1.1.: Net signal comparison of electrons bent in a magnetic field with a 20 mT homogeneous region for rotary angles $\theta = -40, -60, -80$ and $-100°$ for a 5 mm collimator opening, separated for a linear offset of $0, 5, 10$ and 15 mm. The measurement time is always 100 s. For 15 mm offset, the angles are reduced by $-5°$ each. Each corresponding bending angle φ is calculated. The low-level cut corresponds to an energy cut at 0.2 MeV.

position, the electrons are distributed in such a way that only a certain proportion hits the detector, which hits the detector straight or within the angular acceptance. Hence, a Gaussian distribution is expected around the main energy μ. In the best case, the ratio should be PR = 1, meaning that electrons with energy μ hit the detector perpendicularly and are centered in the distribution. A value PR $\neq 1$ indicates that the fitted electrons with energy μ do not hit the detector perpendicularly.

Figure 11.1.3 shows the peak ratios for a 5 mm collimator opening and a 10 mm linear offset. The peak ratio decreases significantly if the angle is too low. The best peak ratio is obtained for $\theta = 70°$, which corresponds to $\varphi = 20.18°$. The peak ratio lies about 90 %.

Scan measurements for 20 mm field and 3 mm collimator

The collimator is reduced to 3 mm to reduce the energy spread by limiting the angular acceptance range. The angular acceptance Δ is the maximal angular deviation under which electrons are still able to pass the collimator. The narrower the collimator aperture, the lower Δ; an ideal Δ of $0°$ means that electrons can only traverse the

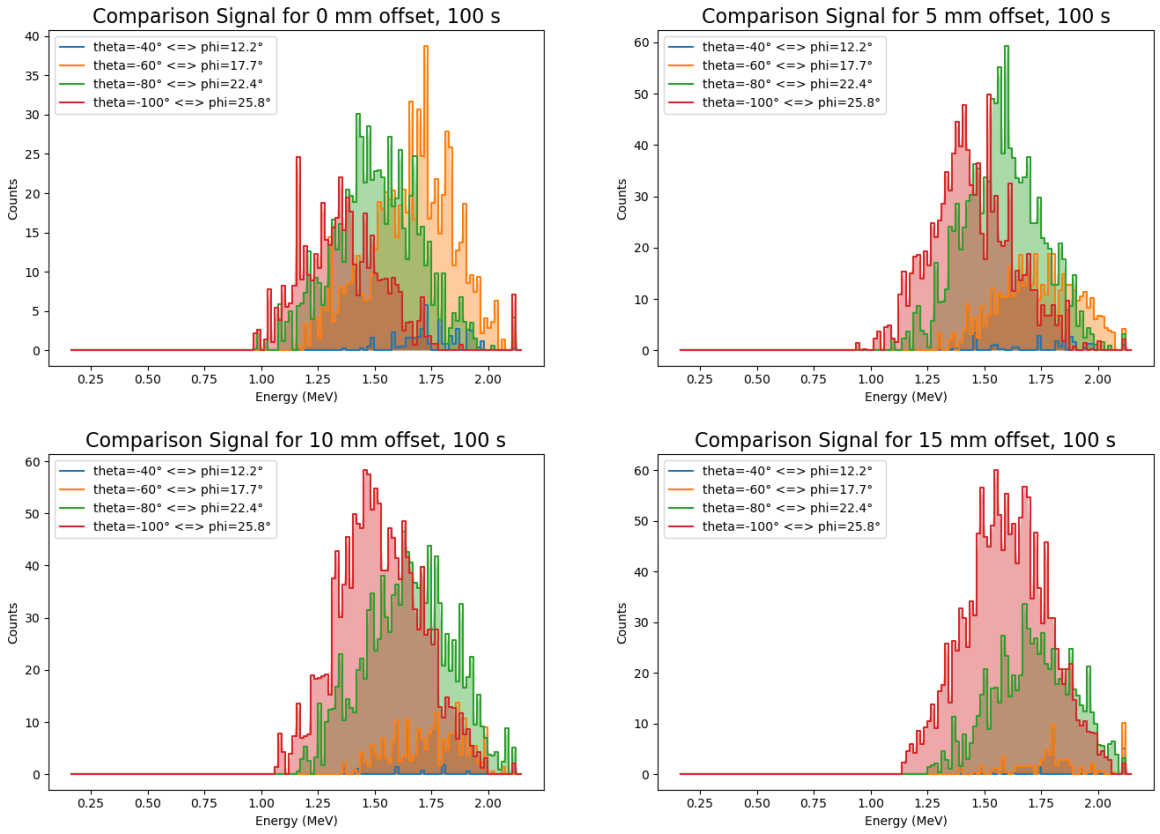

Figure 11.1.2.: Net signal comparison of electrons bent magnetic field with a 30 mT homogeneous section for rotary angles $\theta = -40, -60, -80$ and $-100°$ for a 5 mm collimator opening, separated for a linear offset of $0, 5, 10$ and 15 mm. The measurement time is always 100 s. Each corresponding bending angle φ is calculated. The low-level cut corresponds to an energy cut at 0.2 MeV.

collimator perpendicularly. The angular acceptance is

$$\Delta = \arctan\left(\frac{w_c}{l_c}\right) \quad . \tag{11.4}$$

It depends on both the collimator length l_c[1] and width w_c. A reduction of the width from 5 to 3 mm leads to a reduction of Δ of approximately 60 %, and hence, a reduction of the counts.
Measurements are taken for 20 mT with an extended duration of 600 s. The netto signal spectra for the same angles and offsets as previously are shown in Figure 11.1.4. As expected, the spectra are narrower compared to the 5 mm. While for a 5 mm collimator width (Figure 11.1.1) signals above 1.75 MeV are not recorded, the 3 mm aperture reduces the range below 1.5 MeV.

The corresponding peak ratios for a 10 mm linear offset are depicted in Figure 11.1.5. The best peak ratio are obtained for an rotary angle θ between 60° and 70°. This agrees with the peak ratio for a 5 mm collimator opening (Figure 11.1.3), but the peak ratio drops faster if the angle is changed. That is expected, since the narrower opening causes a reduction of the angular acceptance, so that electrons must traverse the collimator

[1]Not to be confused with the parameter l for the angle relation

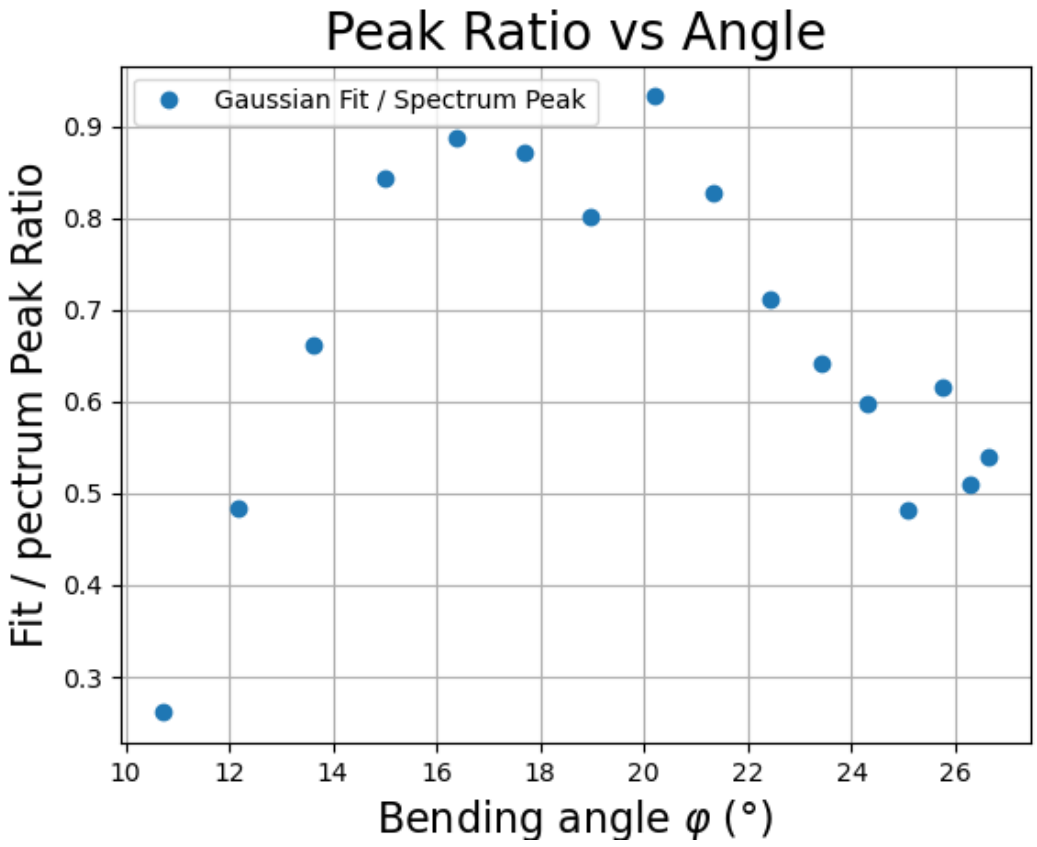

Figure 11.1.3.: Peak ratios for a 5 mm collimator opening and 10 mm linear offset as function of the rotary stage angles θ. The bin width is 64 MCA channels.

more straight.

However, there are some abnormalities. On the one hand, each spectrum consists of an obvious noise peak at the low-energy end, indicating that the background model disagrees with the recorded data. On the other hand, all main bumps are shifted by at least 250 keV to lower energies. For example, as shown in Figure 11.1.1, using the 5 mm opening with a 10 mm offset and $\theta = -60°$, the peak energy is located around 1.25 MeV, in contrast to the peak energy near 1 MeV for the 3 mm opening. Later measurements show that there was an unknown problem with the electronics. The reduction of the amplification factor solved the problem. This, however, implies that the detector calibration cannot be used for future measurements.

11.2. Comparison of experimental scan measurements with the modified Geant4 setup

The modified Geant4 setup is more complex than the Geant4 setup with the homogeneous magnetic field, but it is assumed to provide more realistic results. However, the implementation of an inhomogeneous magnetic field complicates the calculation of the electron trajectories, as both field interpolation and field extrapolation are required. The following scan measurements aim to compare experimental data with simulated

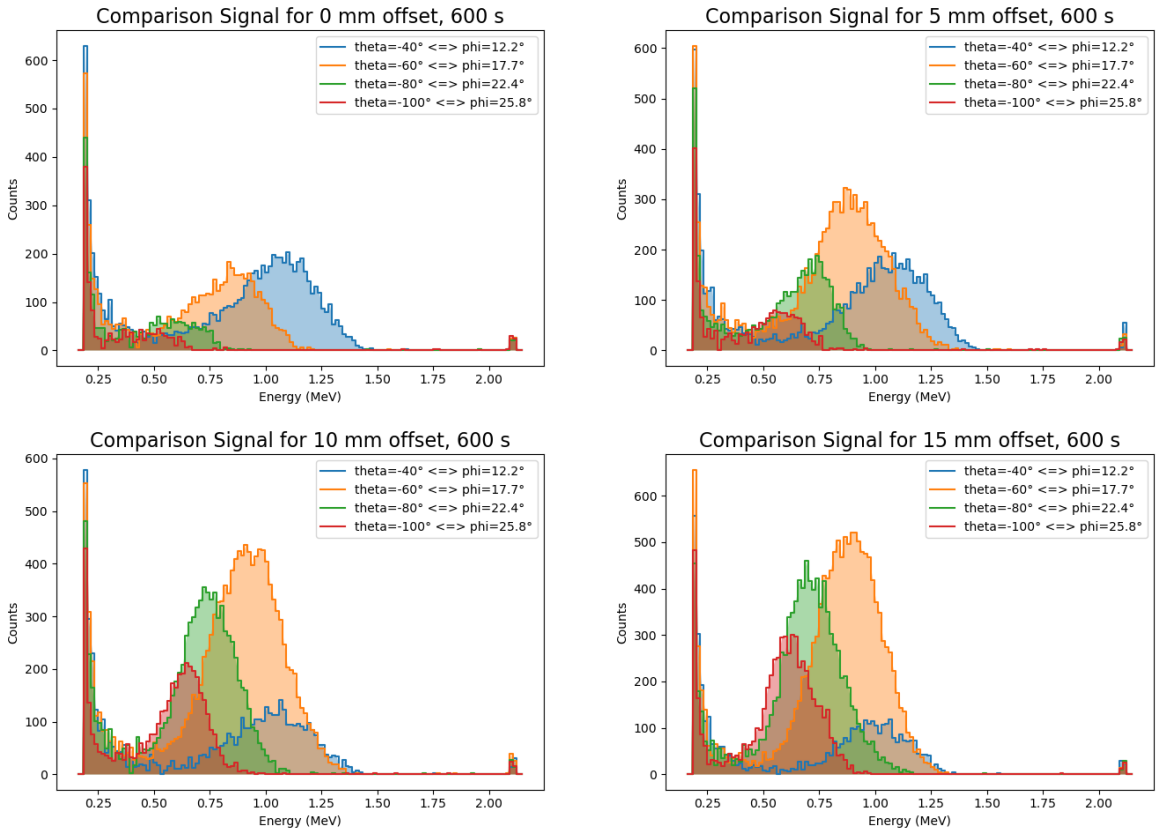

Figure 11.1.4.: Net signal comparison of electrons bent magnetic field with a 20 mT homogeneous section for rotary angles $\theta = -40, -60, -80$ and $-100°$ for a 3 mm collimator opening, separated for a linear offset of $0, 5, 10$ and 15 mm. The measurement time is always 600 s. Each corresponding bending angle φ is calculated. The low-level cut corresponds to an energy cut at 0.2 MeV.

data to analyse how well the magnetic field is approximated. It is a good starting point to check whether the magnetic field strength is either underestimated or overestimated. For the corresponding simulations, the interpolation is based on the weighted 4-Nearest-Neighbor method, which interpolates the magnetic field at a point $\vec{r'}$ by calculating the weighted average magnetic field of the four nearest data points $B_{z,\,\mathrm{i}}$. The weight w_i is considered the Euclidean distance

$$w_\mathrm{i} = \frac{1}{|\vec{r'} - \vec{r_\mathrm{i}}|} \ , \tag{11.5}$$

leading to the interpolation formula

$$B_z^{\mathrm{int}} = \begin{cases} \dfrac{\sum_{\mathrm{i}=1}^{\mathrm{K}} \left(B_{z,\mathrm{i}} \cdot \dfrac{1}{|\vec{r'} - \vec{r_\mathrm{i}}|} \right)}{\sum_{\mathrm{i}=1}^{\mathrm{K}} \left(\dfrac{1}{|\vec{r'} - \vec{r_\mathrm{i}}|} \right)} & , \text{if } \ r_\mathrm{i} \neq 0 \ \forall \ \mathrm{i} \\ B_\mathrm{i} & , \text{if } \ \vec{r_\mathrm{i}} = \vec{r'} \ . \end{cases} \tag{11.6}$$

On the other hand, the extrapolation considers a cubic radial decay

$$B_z^{\mathrm{ext}} = \frac{B_z^{\mathrm{nearest}}}{|\vec{r'} - \vec{r}|^3} \tag{11.7}$$

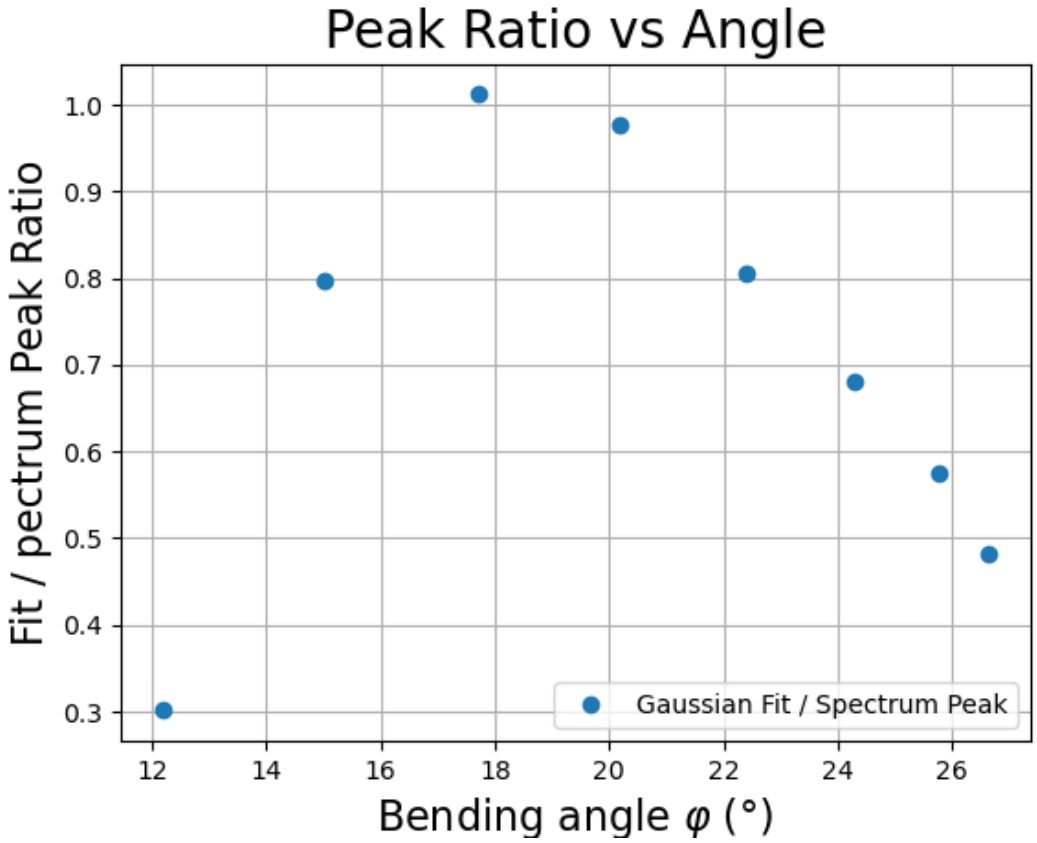

Figure 11.1.5.: Peak ratios for a 3 mm collimator opening and 10 mm linear offset as function of the rotary stage angles θ. The bin width is 64 MCA channels.

of the nearest known field value $\vec{r}$. This decay corresponds to a simplified decay of a magnetic dipole field and is chosen since the used magnet is designed as a dipole magnet, consisting of two coils and an iron yoke. Furthermore, a vacuum, defined by a pressure of 10 mbar and a temperature of 300 K, is set. The particle gun emits electrons with an angular deviation up to 2°.
Figure 11.2.1 presents some comparisons for the 20 mT field between the Geant4 simulation and experimental data from the electron monochromator. The experimental results agree with the 5 mm collimator opening, shown on the right side. The best match is for $\theta = 60°$. The experimental energy spread reduces with larger bending angles φ, while the simulated distribution becomes asymmetric. The difference in the energy spread is clearer for 3 mm opening on the right side. An angle increase does not affect the simulated spread at all.

11.3. Conclusion for the scan measurements

Scan measurements for 20 mT for different linear offsets were examined. The experimental net signal depends on the setting of the source position; both the angular alignment and the linear offset affect the number of detected signals and the energy range. Furthermore, a reduction of the collimator aperture significantly improves the energy resolution. For the Geant4 simulations, instead, a 3 mm collimator opening does not reduce the energy spread. The energy spread difference between simulation

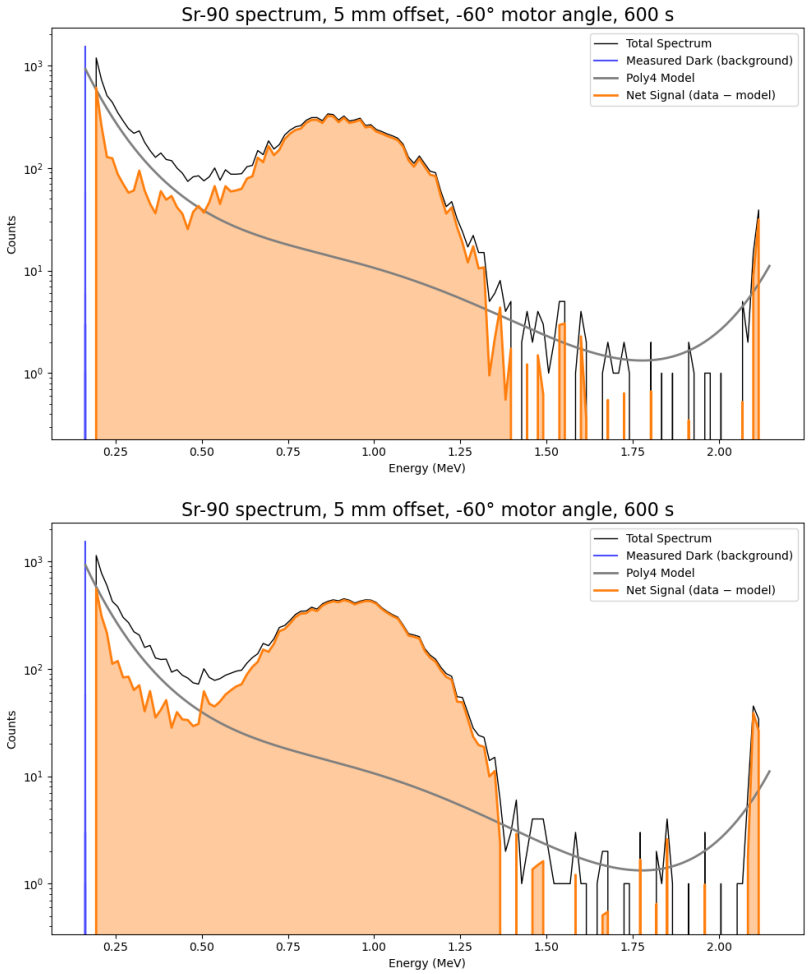

Figure 11.1.6.: Recorded spectra for 3 mm collimator opening at 20 mT. Top: $\varphi = 17.70°$ and 5 mm offset. Bottom: $\varphi = 17.70°$ and 10 mm offset. The duration for both measurements and the corresponding dark measurement is 600 s.

and experiment increases with larger angles. This implies that the simulated setup still needs to be improved.

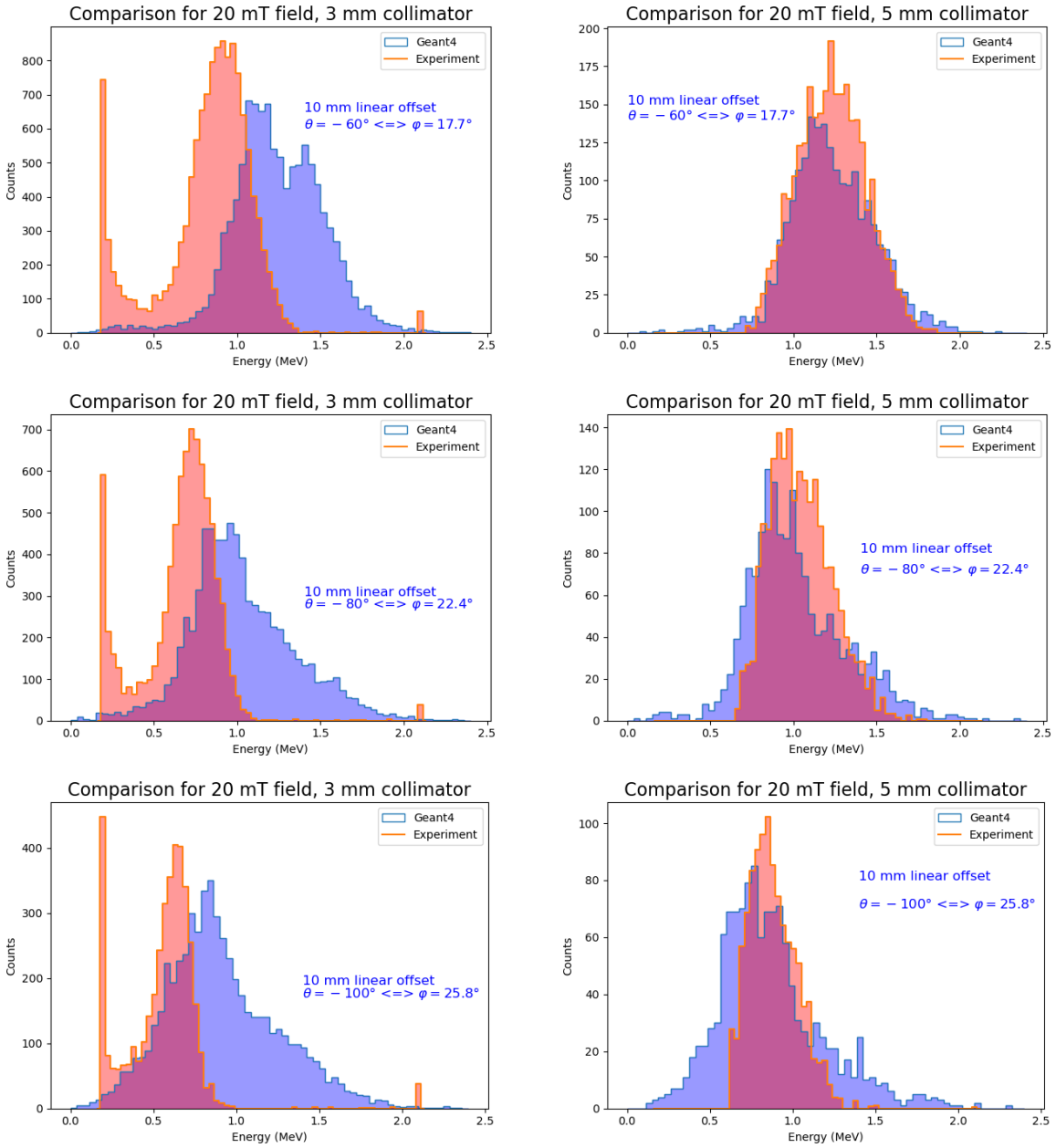

Figure 11.2.1.: Comparison of the energy spectrum at the detector between the Geant4 simulation and experimental data. The experimental data includes only the net signal.

12. Magnetic field interpolation

The magnetic field is a crucial part of the electron monochromator, since it is necessary to separate electrons with different energies. Even slight changes in a homogeneous magnetic field significantly influence the electron trajectory; hence, it is necessary to optimize the magnetic field approximation to ensure not only proper numerical calculations, but also realistic Geant4 simulations.

A field interpolation is necessary since the distance between adjacent measured points ($> 3\,\mathrm{mm}$) is significantly greater than the electron iteration length in Geant4 and the numerical calculations (a few tens µm at last). Here, we limit to two different interpolation classes: the weighted K-Nearest-Neighbor algorithm and Radial Basis Functions. Since the 4-Nearest-Neighbor is used as the default, the goal of this study is to prove the quality of the implemented function and to check if the interpolation needs to be improved.

12.1. K-Nearest Neighbor method

A simple interpolation method is the weighted K-Nearest Neighbor (K-NN) algorithm, where K represents the number of nearest points that are considered in the interpolation. It is a standard algorithm for various Machine Learning tasks, both regression and classification. The interpolation of the magnetic field $B_z\left(\vec{r'}\right)$ at point $\vec{r'} = (x'_\mathrm{i}, y'_\mathrm{i}, z'_\mathrm{i})^\mathrm{T}$ is computed by using the weighted mean formula

$$B_z\left(\vec{r'}\right) = \frac{\sum_{\mathrm{i}=1}^{\mathrm{K}} \left(w_\mathrm{i}^p \cdot B_{z,\mathrm{i}}(\vec{r_\mathrm{i}})\right)^p}{\sum_{\mathrm{i}=1}^{K} w_\mathrm{i}} \quad , \tag{12.1}$$

summing up the measured field values $B_{z,\mathrm{i}}$ at points $\vec{r_\mathrm{i}} = (x_\mathrm{i}, y_\mathrm{i}, z_\mathrm{i})^\mathrm{T}$ and their respective weights w_i^p. These weights correspond to the Minkowski distance

$$w_\mathrm{i} = \frac{1}{\left(|x' - x_\mathrm{i}|^p + |y' - y_\mathrm{i}|^p\right)^{\frac{1}{p}}} \tag{12.2}$$

and depends on the power parameter p. Setting $p = 2$ results in the known Euclidean distance

$$w_\mathrm{i} = \sqrt{(x' - x_\mathrm{i})^2 + (x' - x_\mathrm{i})^2} \; . \tag{12.3}$$

While a high p parameter penalizes large distances even more, which can be useful for clustered grids or large changes, reducing p lowers the weighting factors. Inserting equation 12.2 into 12.1, leads to

$$B_z^{\text{K-NN}} = \begin{cases} \dfrac{\sum_{\text{i}=1}^{\text{K}} \left(B_{z,\text{i}} \cdot \dfrac{1}{(|x' - x_\text{i}|^p + |x' - x_\text{i}|^p)^{\frac{1}{p}}} \right)}{\sum_{\text{i}=1}^{\text{K}} \left(\dfrac{1}{(|x' - x_\text{i}|^p + |x' - x_\text{i}|^p)^{\frac{1}{p}}} \right)} & \text{, if } \; r_\text{i} \neq 0 \; \forall \; \text{i} \\ B_\text{i} & \text{, if } \; \vec{r_\text{i}'} = \vec{r'} \; . \end{cases} \tag{12.4}$$

If the interpolated points match a known point, its value is assumed. In contrast to Radial Basis Functions, this assumption is necessary; otherwise, the interpolation will crash. Hence, the K-NN method provides a non-smooth interpolation.
Tunable parameters for the K-NN are the number of considered neighbors K and the power parameter p. Different combinations are tested and analyzed using methods of the Python library "sklearn". The measured field data is randomly split five times into 80 % training and 20 % test datasets using "KFold". After training the K-NN model (KNeighborsRegressor), the Cross-Validation Root Mean Squared Error (CV-RMSE) and the averaged goodness of fit R^2 are calculated.
Both parameters K and p are varied between 1 and 5 in integer steps. The 'best' K-NN interpolation based on CV-RMSE and R^2 for all measured fields is summarized in Figure 12.1.1. The CV-RMSE values are marked in blue, while the R^2s are colored in red. In each case, the best result is obtained using $p = 1$, the lowest possible value for a proper Minkowski metric, in a 3-KK or 4-KK interpolation. The CV-RMSE increases with the total magnetic field strength, while R^2 does not change significantly and remains at a high level. The influence of K is shown in Figure 12.1.2 and validates 3 and 4 as the optimal number of included neighbors K due to the lowest CV-RMSE values. The CV-RMSE indicates the average absolute error between known data and predicted data and depends on the $B_{z,\text{i}}$. Therefore, a linear increase is expected, which agrees with the measured field strengths in the homogeneous region, see Table 12.1. If the CV-RMSE is scaled with these values, the average relative error for the interpolated points lies between 1.5 and 2.5 %.

Magnetic field (mT)	Nearest point K	Power parameter p	CV-RMSE (mT)
10	4	1	0.18
20	3	1	0.36
30	3	1	0.53
40	4	1	0.97
60	3	1	1.6

Table 12.1.: CV-RMSE values using best K-NN for each magnetic field.

12.2. Radial basis functions

Radial basis functions (RBF) are a popular type of meshless method often used for the reconstruction of unknown data or functions in neural networks. Meshless means that the known data does not require special configuration, as the entire test data (known

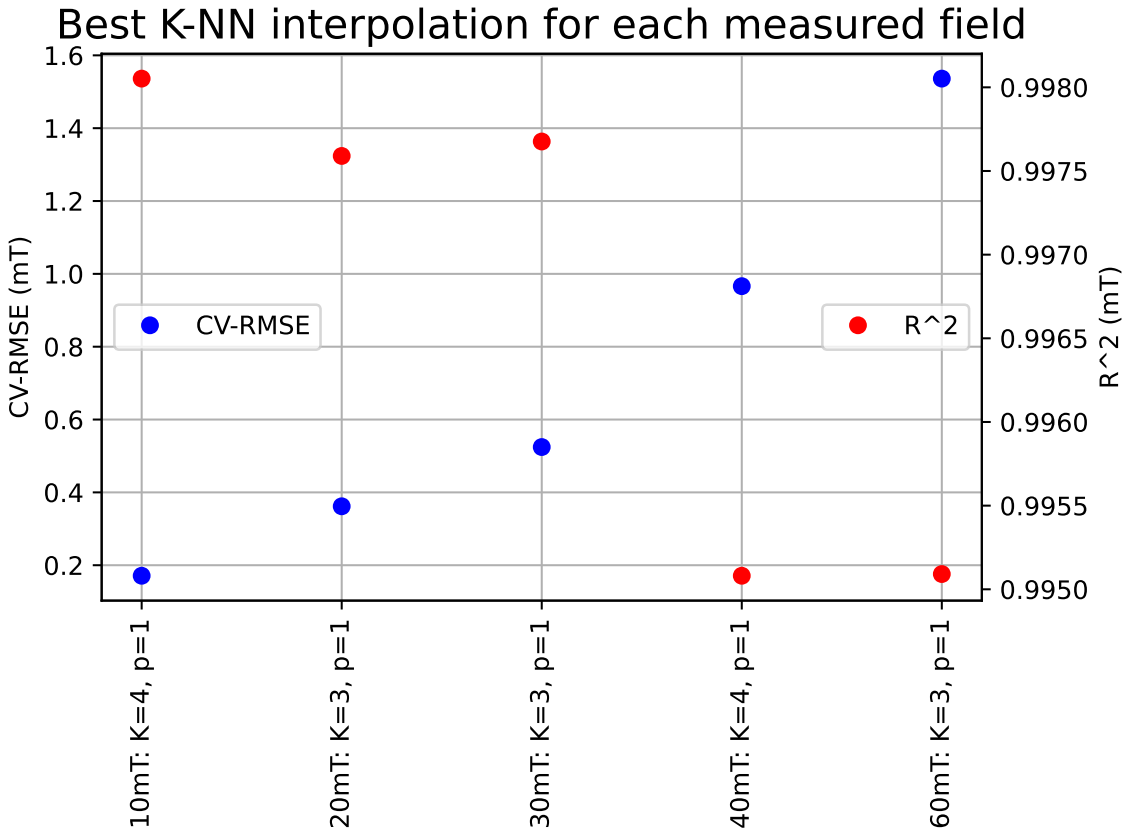

Figure 12.1.1.: CV-RMSE and R^2 for the best K-NN combinations. The parameters K and p are varied from 1 to 5 in full steps.

data) influences the interpolation by default. RBFs are further multivariate, analytic functions and therefore exactly differentiable, providing smooth and continuous results. Here, it is focused on two popular RBFs, the Multiquadratic

$$\Phi_{\text{Mult}}(\vec{x}) = \sqrt{1 + ||\vec{x}||_2^2} \tag{12.5}$$

and the Gaussian RBF

$$\Phi_{\text{Gaus}}(\vec{x}) = \exp\left(-||\vec{x}||_2^2\right), \tag{12.6}$$

where the Euclidean norm

$$||\vec{x}||_2 = \sqrt{\sum_{\text{k}=1}^{\text{n}} x_{\text{k}}^2} \tag{12.7}$$

reduces the n-dimensional feature (input) vector $\vec{x}$ to a scalar. Nowadays, a hyper-parameter ϵ is added to optimize the interpolation. The interpolation is executed by calculating the 'trial functions'

$$u(\vec{x}) = \sum_{\text{k}=1}^{n} \alpha_{\text{k}} \, \Phi(||\vec{x} - \vec{y_{\text{k}}}||_2) \, , \tag{12.8}$$

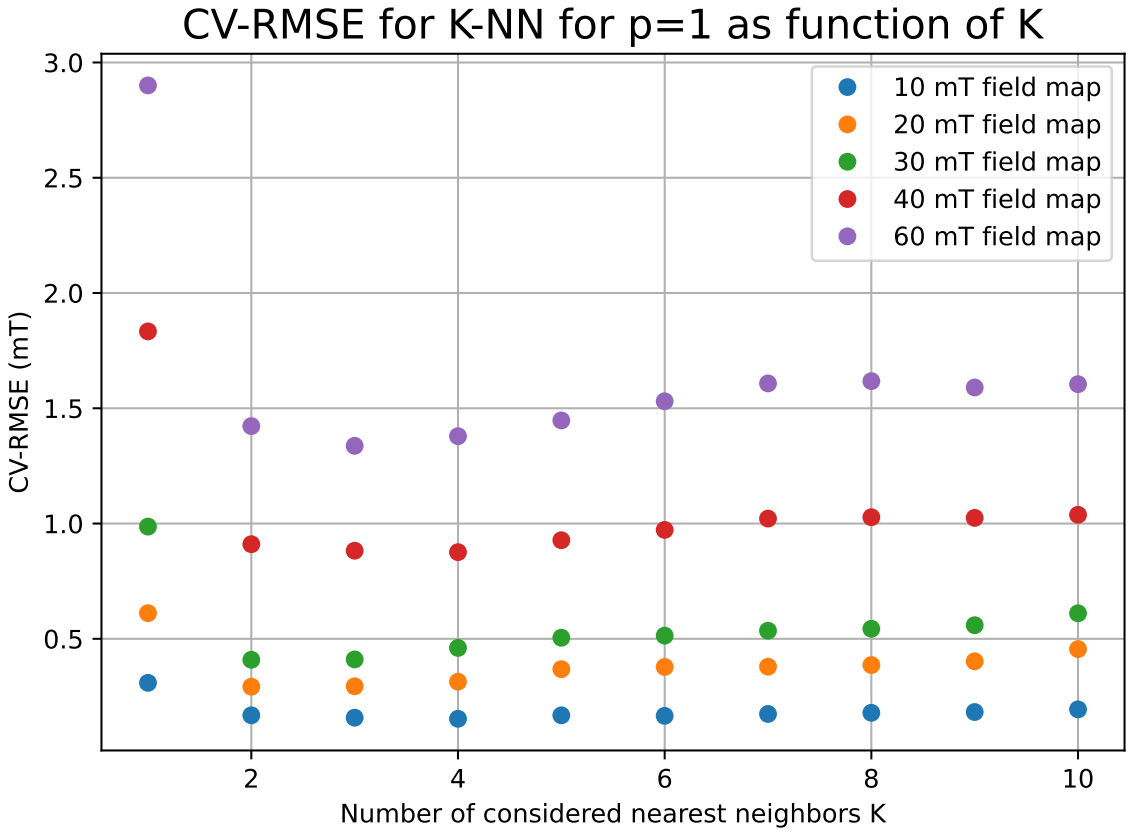

Figure 12.1.2.: CV-RMSE for $p = 1$ and different number of neighbors K.

consisting of the absolute distance between the interpolation point y and the known data points x_k. Each summand is multiplied by a scale factor α_k, which scales the functions to the actual data. [Sch07]
In the case of the magnetic field, $\vec{r}$ consists of the distance

$$\vec{r} = \vec{r'} - \vec{r_\mathrm{k}} \tag{12.9}$$

between the interpolated point $\vec{r'}$ and the measured point $\vec{r_\mathrm{k}}$. By combining this with the sharing parameter ε, the interpolation for the z component of the magnetic field B_z using the Gaussian function results in

$$B_z^{\mathrm{Gaus}} = \sum_{\mathrm{k}=1}^{n} \alpha_\mathrm{k} \exp\left(-\left(\frac{\varepsilon}{r}\right)^2\right) \ , \tag{12.10}$$

and $\Phi_\mathrm{k}\ \alpha_\mathrm{k} = B_{z,\,\mathrm{k}}$. $B_{z,\,\mathrm{k}}$ denotes the measured field at point k. For the Multiquadratic function, one obtains

$$B_z^{\mathrm{mult}} = \sum_{\mathrm{k}=1}^{n} \alpha_\mathrm{k} \sqrt{1 + \left(\frac{\varepsilon}{r}\right)^2} \ . \tag{12.11}$$

Similar to the K-NN method, the data is split up into a 80 % training and a 20 % test subset. The resulting CV-RMSE is then compared for different shaping parameters ε (50 to 1000 in steps of 50), whose results are summarized in Table 12.2. In case of the

Gaussian RBF, the best ε lies around 150. A larger or lower ε significantly increases the CV-RMSE, leading to a worse prediction, illustrated in Figure 12.2.1. Furthermore, the higher fields, especially the 60 mT one, tend to require a better determination of ε than the lower fields. The corresponding best shaping parameters are listed in Table 12.2. On the other hand, the Multiquadratic RBF interpolation also requires a sufficiently large ε, but in contrast to the Gaussian RBF, the CV-RMSE does not significantly increase for large ε within the inspected region. This can be seen in Figure 12.2.2. For 10, 20 and 30 mT, a good choice is $\varepsilon > 250$, while ε should greater than 800 for 40 and 60 mT.

Magnetic field	Gaussian RBF		Multiquadratic RBF	
(mT)	Parameter ε	CV-RMSE (mT)	Parameter ε	CV-RMSE (mT)
10	180	0.27	500	0.11
20	140	0.49	200	0.18
30	130	0.67	250	0.26
40	190	3.6	1000	0.79
60	170	4.1	1000	1.1

Table 12.2.: Best results for interpolation using Multiquadratic and Gaussian RBF for each magnetic field.

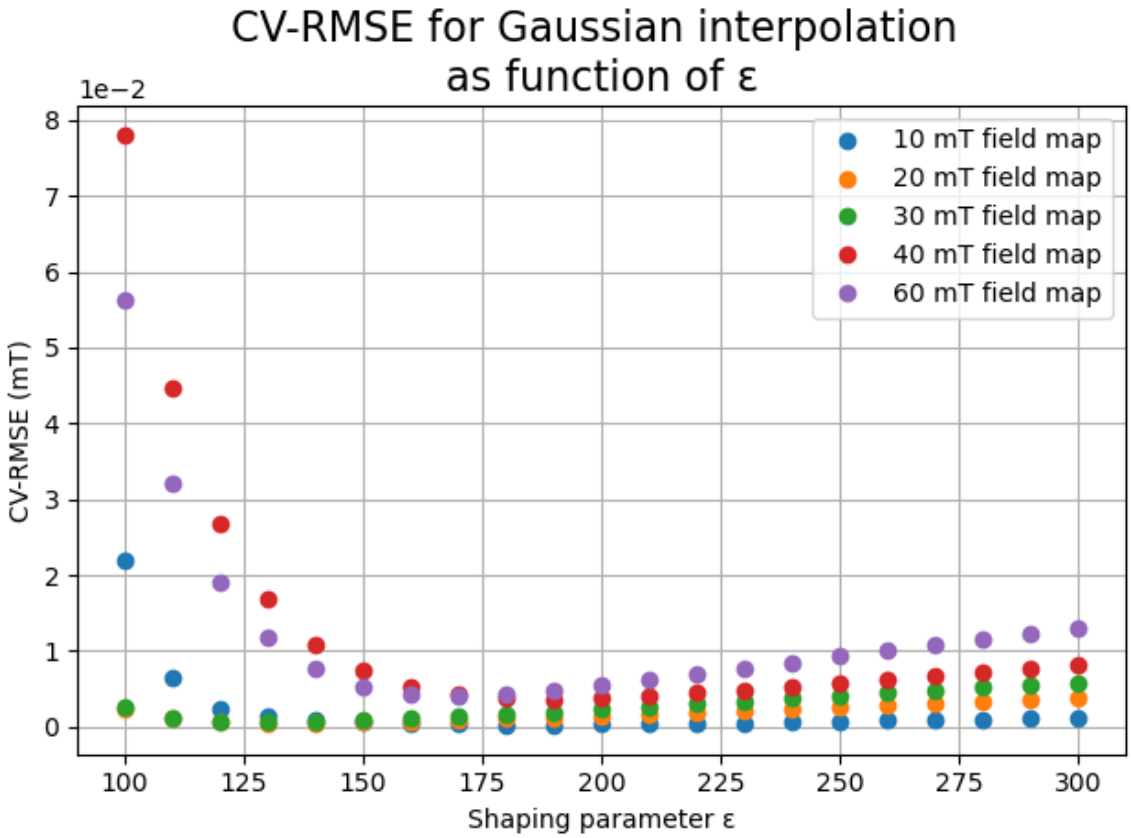

Figure 12.2.1.: CV-RMSE for different shaping parameter ε for Gaussian RBF.

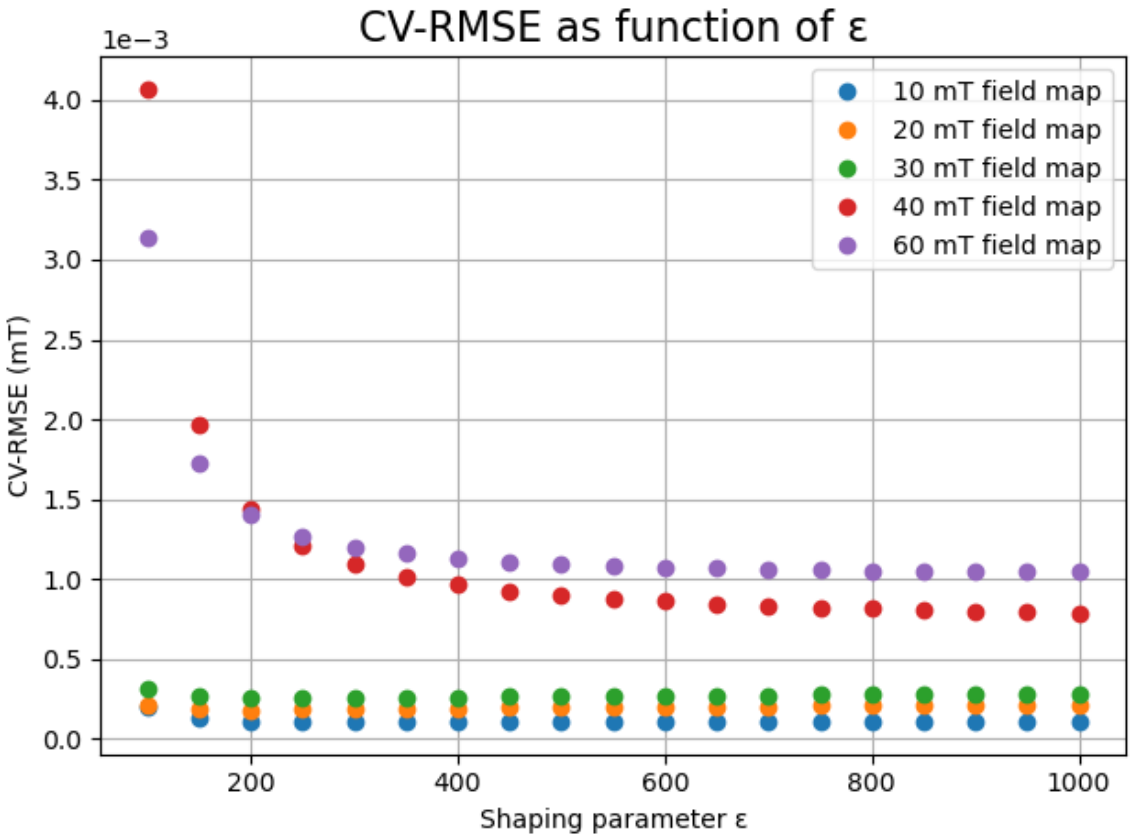

Figure 12.2.2.: CV-RMSE for different shaping parameter ε for Multiquadratic RBF.

12.3. Comparison of the interpolation methods

The Multiquadratic method yields the best interpolation as indicated by the CV-RMSE, as shown in Table 12.3. For the 20 mT field, the CV-RMSE for Gaussian RBF is 4 times higher than for the Multiquadratic, while the 4-KK is nearly 3 magnitudes larger. However, it is only an indication and can depend on the train-test split. Therefore, the entire field within the measured region is interpolated. The resulting maps are depicted in Figure 12.3.1. The interpolation is based on a 300×300 point grid, equidistantly distributed, and this time, the entire data set is used for the training. The electrons travel along the x-axis, and the linear stage along the y-axis. All interpolations match the global trend: the magnetic field starts to decrease at $x \approx 0.03$ m, corresponding to the position along the x-axis, where the vig Mu-metal region starts (35.4 mm). The 3NN field has a similar quality to the Multigaussian RBF, while the Gaussian RBF produces some irregularities around $x \approx 0.04$ m, where the field slightly increases. Hence, the Gaussian RBF interpolation is not as smooth as the other ones, and therefore not suitable for the magnet interpolation.

A further comparison between the 4NN and the Multiquadratic RBF shows no significant difference in the trajectory calculation between the two interpolations, which is shown in Figure 12.3.2. The trajectory calculations outside the measured field stayed untouched and will not affect the overall trajectory. Despite the 4NN (old method), on the left side, interpolating being slightly worse than the 3NN (CV-RMSE difference

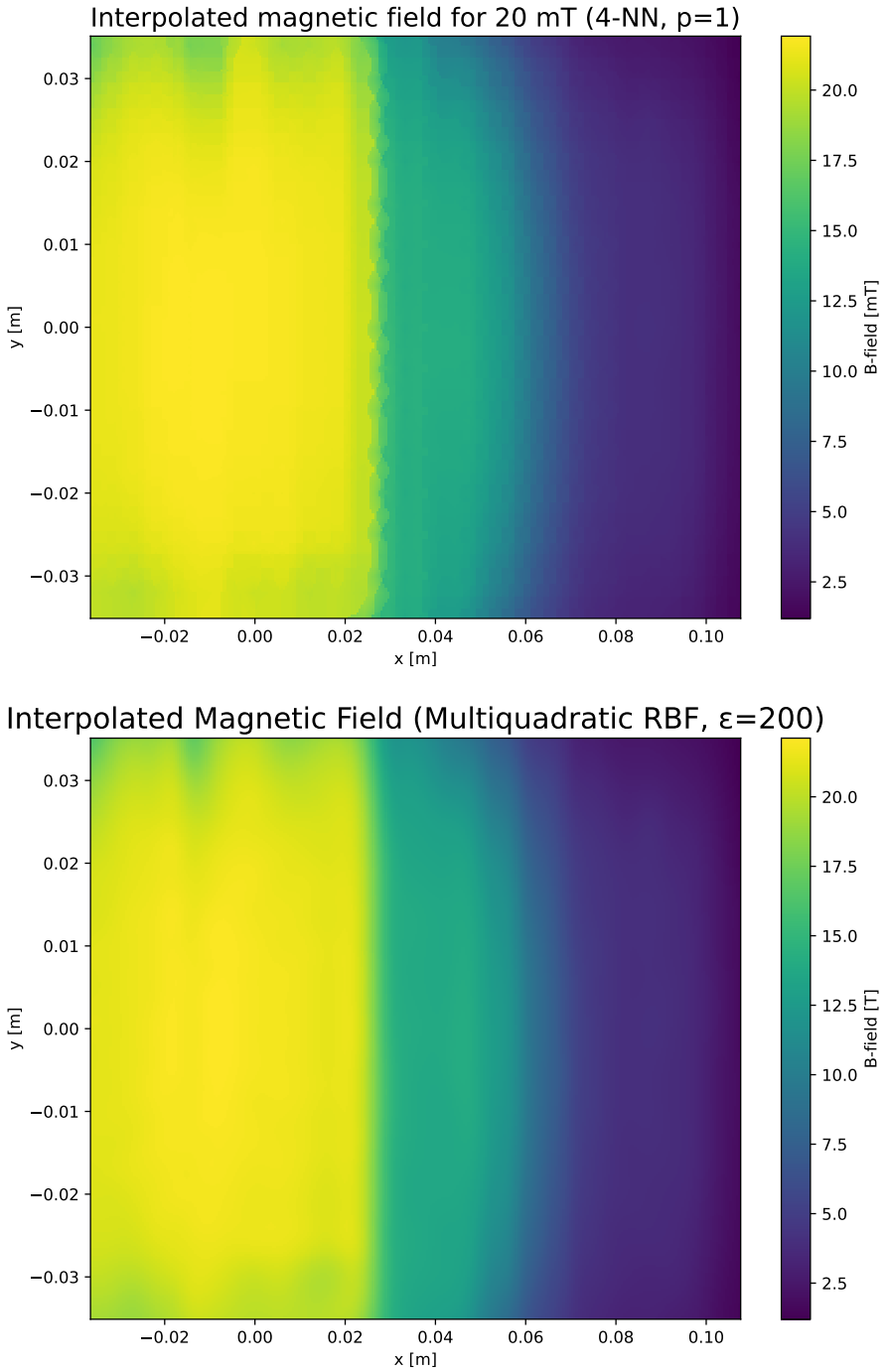

Figure 12.3.1.: Interpolated field maps for 20 mT. Top: 4-KK with $p = 1$, Gaussian RBF with $\varepsilon = 140$. Bottom: Multiquadratic RBF with $\varepsilon = 200$.

Interpolation function	CV-RMSE for corresponding field in mT				
	10 mT	20 mT	30 mT	40 mT	60 mT
4-NN method	0.18	0.36	0.53	0.97	1.6
Gaussian RBF	0.27	0.49	0.67	3.6	4.1
Multiquadratic RBF	0.11	0.18	0.26	0.79	1.1

Table 12.3.: CV-RMSE comparison between 4NN and the RBF methods for the best parameters.

less than 0.02 mT), it agrees with the Multiquadratic RBF's result. This validates the appropriate interpolation using 4NN, which does not need improvement. The next step in the magnetic field evaluation is the investigation of the extrapolation method, but this is outside of the scope of this thesis.

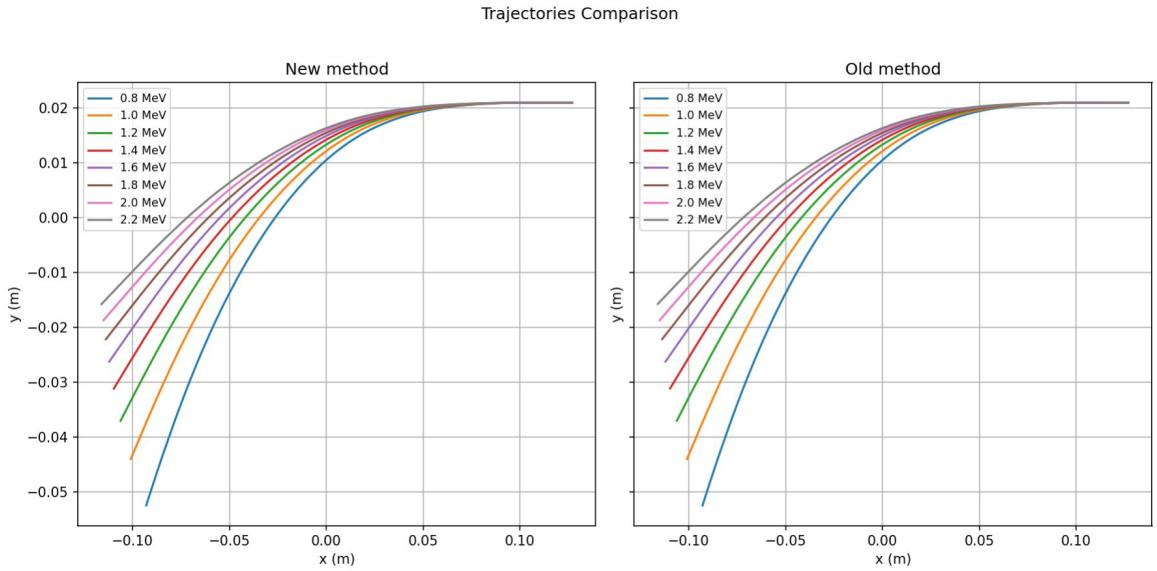

Figure 12.3.2.: Calculated electron trajectories for different electron energies. Top: 4NN (old method). Bottom: Multiquadratic RBF (new method).

13. Summary and future outlook

In the scope of this thesis, the concept of the electron monochromator for the investigation of high-energy electrons above 900 keV has been made. Geant4 simulations with a homogeneous magnetic field were used to validate the experimental setup by investigating the influence of the remaining gas in the vacuum chamber on the energy resolution of the electrons after passing the collimator. The energy resolution is not affected significantly if the vacuum is below 10 mbar. It was identified that the angular dispersion of the emitted electrons dominates the energy resolution. A multichannel analyzer was validated as a readout system for the experimental setup. Multiple detectors were tested to detect particles. An MCA-energy calibration using a combination of a BC-408 plastic scintillator and a PMT was successfully applied. The experimental setup was modified by a new source holder design, and the distance between the source and the detector could be reduced by around 60 mm, reducing the interaction of electrons with the remaining gas.
The existing Geant4 setup for the electron monochromator was tuned by a detailed investigation of the experimental setup. A geometrical adjustment is the addition of the source box, whose small collimated opening reduces the angular dispersion significantly. The magnetic field inside the chamber was measured for different magnetic field strengths to create detailed magnetic field maps. It could be shown that the initial implementation of a pure homogeneous magnetic field is incorrect, since there are measurable rest magnetic fields inside the mu metal tubes and cannot be neglected. At last, the first scan measurements were done to compare the experimental results with the Geant4 simulations.

These first tests of the electron monochromator are promising and showed that the overall concept works. Now, more detailed studies are mandatory to improve the energy resolution. For this, the interplay between the experiment and the Geant4 simulation is necessary. The magnetic field extrapolation of the inhomogeneous magnetic field regions needs to be investigated. Currently, a cubic decay $B(\vec{r'}) = \frac{B(\vec{r})}{(|\vec{r'}-\vec{r}|^3)}$ is assumed for a magnetic dipole field, based on the nearest measured magnetic field point $B(\vec{r})$. However, this model has to be modified since it does not include the effects of the mu metals. A comparison of Geant4 simulations with the experimental data can help to validate different extrapolation methods. After optimising the magnetic field approximation, it can then be used in the numerical calculations to determine the positions for measuring specific electron energies.
On the experimental electron monochromator side, the next step is to optimise the energy resolution by increasing the magnetic field and reducing the collimator aperture. Since this will reduce the statistics, the total duration of measurements has to be increased. This implies further investigations about additional influences, such as heat development at the magnet. One has to observe if a temperature increase will significantly affect the measurements. Additionally, a calibration with a GAGG scintillator is planned, whose energy resolution is assumed to be better than the resolution of the

BC-408 plastic scintillator.
In the near future, once the calibration is done and the optimal source positions and magnetic field settings are found to investigate specific electrons, the second phase of the electron monochromator experiment can start, which is the reconstruction of an electron using the distribution of its created Cherenkov photons. For this, the scintillator and PMT are replaced by PMMA multiple SiPM arrays.

A. Appendix

A.1. Energy spreads for numerical calculations

	B (mT)						
E(MeV)	20	30	40	50	60	70	80
0.6	8.2	5.3					
0.8	9.8	6.3	4.6				
1.0	11.2	7.2	5.3	4.1			
1.2	12.7	8.2	6.0	4.7	3.8		
1.4	14.1	9.1	6.6	5.2	4.3	3.6	
1.6	15.7	10.0	7.3	5.8	4.7	3.9	
1.8	16.7	10.9	7.9	6.2	5.1	4.3	3.7
2.0	15.0	11.8	8.6	6.8	5.6	4.7	4.1
2.2	13.6	12.7	9.3	7.3	6.0	5.0	4.4

Table A.1.: Pivot table of calculated energy spreads for a 5 mm collimator opening for various homogeneous field strengths. All energy resolutions are calculated by Equation 6.4 and given in %.

	B (mT)						
E(MeV)	20	30	40	50	60	70	80
0.6	4.0	2.5					
0.8	4.6	3.0	2.3				
1.0	5.4	3.5	2.6	2.0			
1.2	6.0	3.9	2.9	2.3	1.8		
1.4	6.7	4.4	3.2	2.5	2.1	1.7	
1.6	7.3	4.8	3.2	2.8	2.3	1.9	
1.8	8.0	5.2	3.8	3.1	2.5	2.1	1.8
2.0	8.7	5.6	4.2	3.3	2.7	2.3	2.0
2.2	9.3	6.1	4.5	3.5	2.9	2.5	2.1

Table A.2.: Pivot table of calculated energy spreads for a 2.5 mm collimator opening for various homogeneous magnetic fields. All energy resolutions are calculated by Equation 6.4 and given in %.

A.2. Measured magnetic field maps

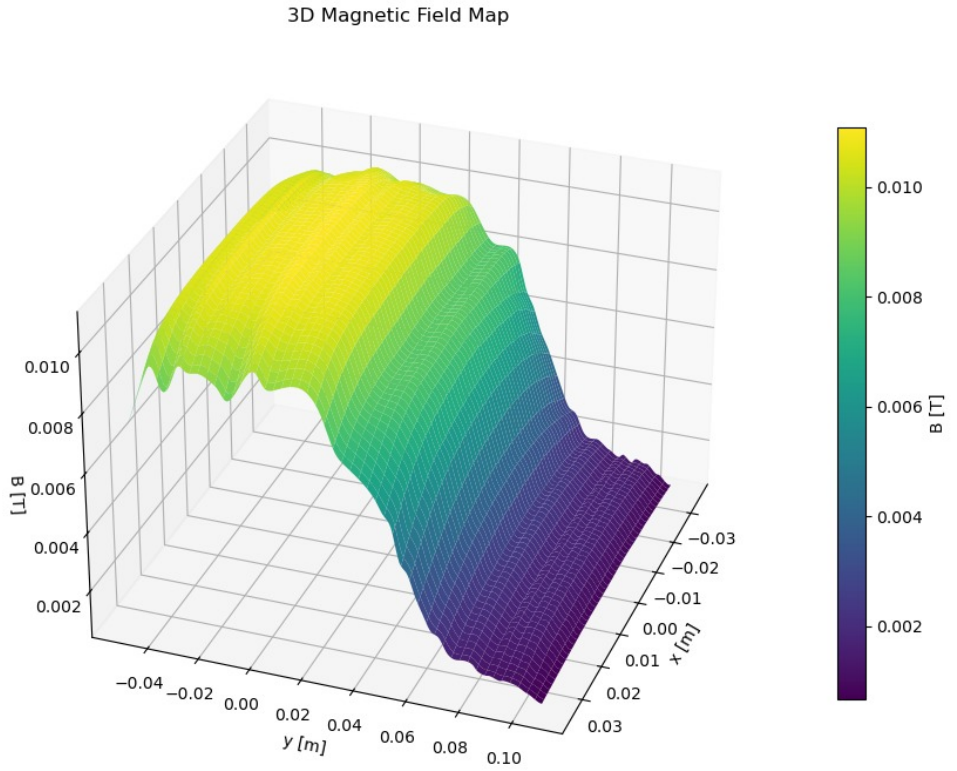

Figure A.2.1.: Approximated 10 mT magnetic field with linear interpolation for visualization. It is calculated by taking the mean value of the measured magnetic fields (20, 30, 40 and 60 mT).

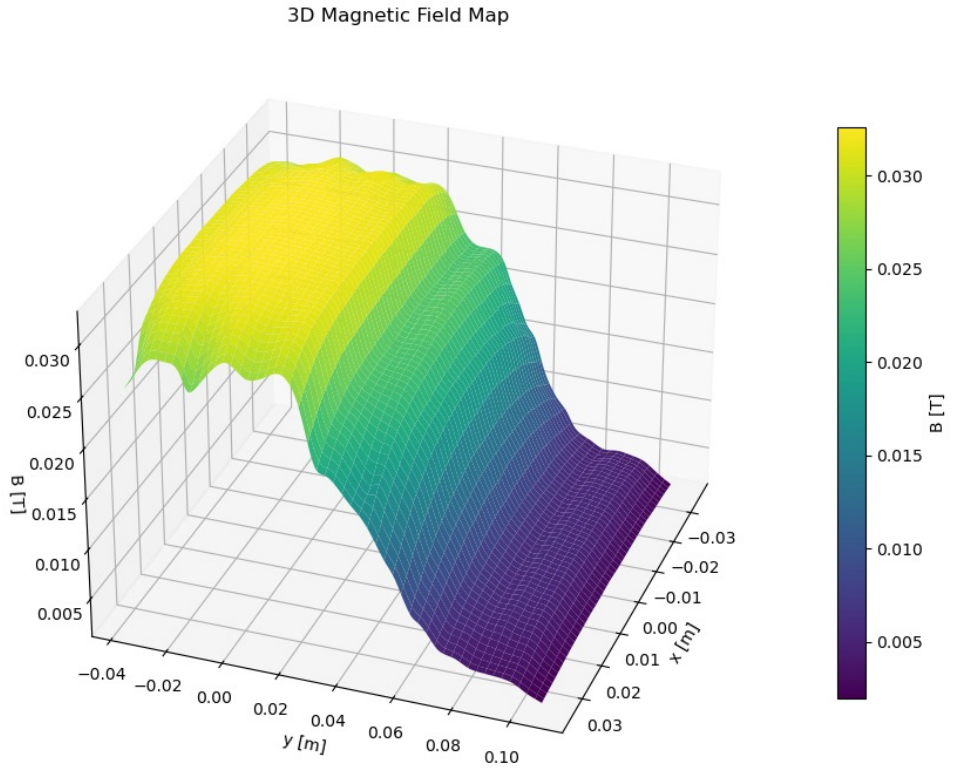

Figure A.2.2.: Measured 30 mT magnetic field with linear interpolation for visualization.

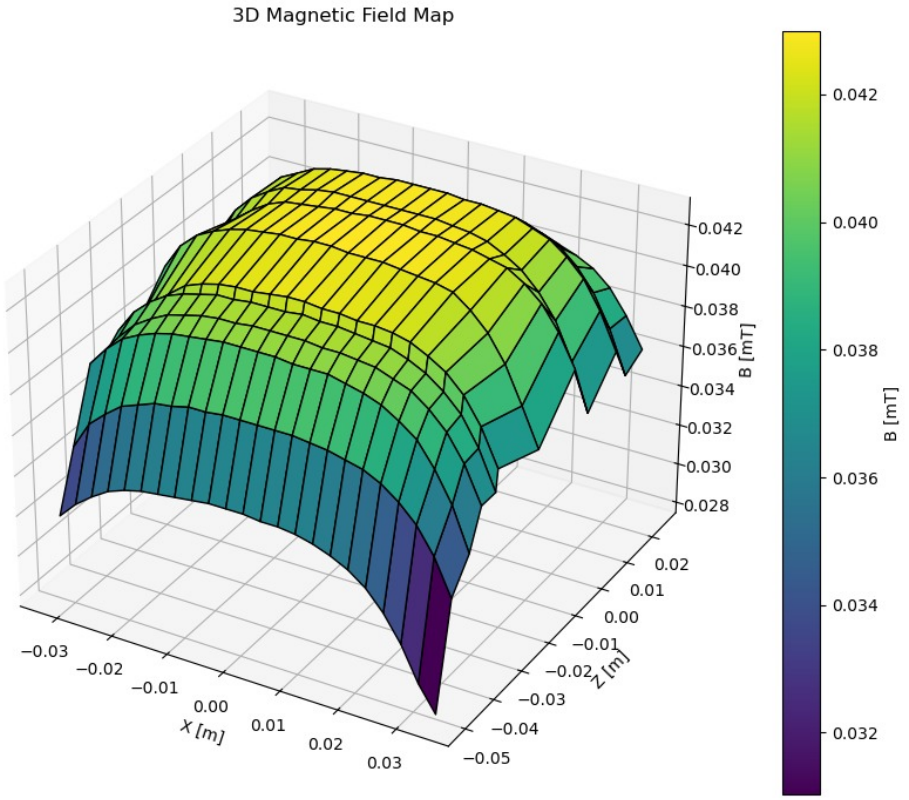

Figure A.2.3.: Measured 40 mT magnetic field with linear interpolation for visualization.

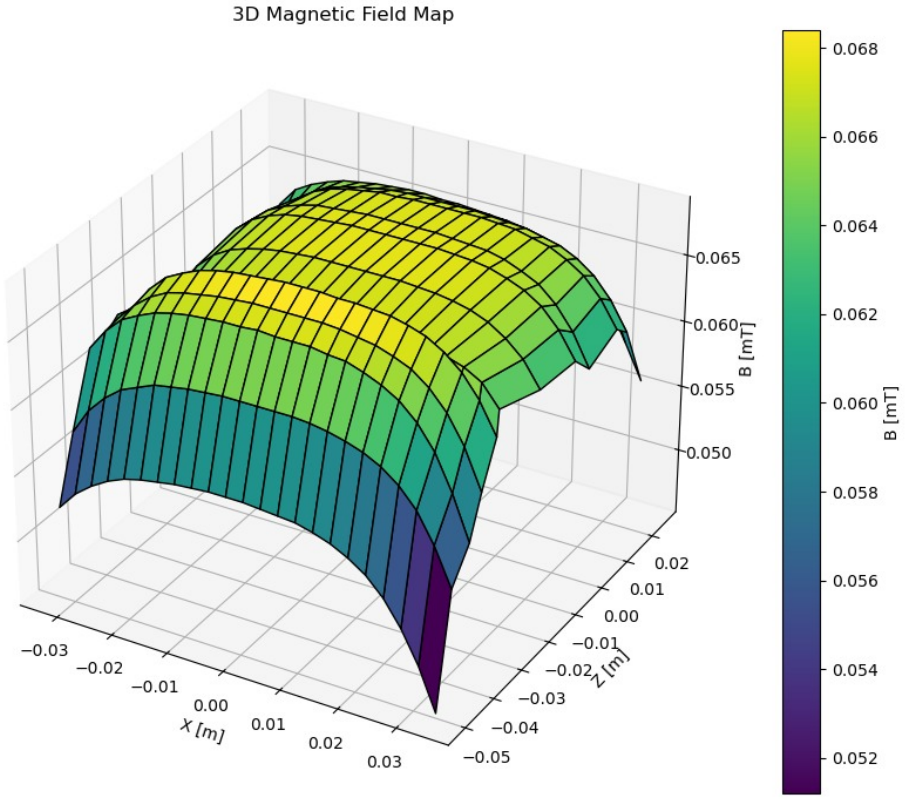

Figure A.2.4.: Measured 60 mT magnetic field with linear interpolation for visualization.

Acknowledgements

It would be disrespectful to claim that the work behind this thesis was done without any support. Therefore, I want to use this moment to thank all the people who played a part in the process of this work.
First of all, I would like to thank Prof. Dr. Ivor Fleck for allowing me to work on this exciting project and for learning about detection techniques in the medical field, as well as for his supervision and continuous support. Furthermore, I want to thank Prof. Dr. Markus Risse, who kindly agreed to be the second reviewer of my thesis.
The experimental setup would not work as good as it did without some specialists. I want to thank Dr. Ulrich Werthenbach for sharing his knowledge about analog electronics and his advice on how to modify the setup. I would also like to thank the mechanical workshop around Nik Röcher, Olaf Meyer, and Jörn Falke, who never hesitated to create adjustments for the vacuum chamber. A further thank you goes to the electronic lab under the direction of Dr. Michael Ziolkowski, whose door was always open in case of a problem regarding the electronic readout system.
It would be impossible to present all the results in the thesis without getting help during the measurements and simulations. Therefore, a big thanks to Yazeed Balasmeh, who not only introduced Geant4 to me, but who also was always able to fix my problems. I want to thank Atharva Bahekar and Darshil Vagadiya for lending me a hand with the various experimental measurements. A special thanks to Lars Maczey, Mara Fries and Devanshi Mehta for having an open ear and making the lab work much more exciting. I would like to thank the people from the engineering group under the guidance of Prof. Dr. Obermaisser. Furthermore, I am very grateful to be part of the HEP department of the University of Siegen, creating many exciting and enjoyable memories. I also want to thank all the people I can call friends.
Last but not least, I definitely want to thank my family for their continuous support in giving me the chance to study physics. Without them, it would not be possible to create this thesis.

Bibliography

[TNE74] R. W. TODD, J. M. NIGHTINGALE, and D. B. EVERETT. "A proposed g camera". In: *Nature* 251.5471 (1974), pp. 132–134. ISSN: 0028-0836. DOI: 10.1038/251132a0.

[Lar+96] JA Larameé et al. *Electron monochromator-mass spectrometer instrument for negative ion analysis of electronegative compounds*. Ed. by Mass Spectrom Rev. 1996. URL: https://pubmed.ncbi.nlm.nih.gov/27082168/.

[BT07] E. Browne and J.K. Tuli. *Nuclear Data Sheets 108,2173*. 2007. URL: https://www.nndc.bnl.gov/nudat3/decaysearchdirect.jsp?nuc=137Cs&unc=NDS.

[Sch07] R. Schaback. *A Practical Guide to Radial Basis Functions*. 2007. URL: https://www.google.com/url?sa=t&source=web&rct=j&opi=89978449&url=https://num.math.uni-goettingen.de/schaback/teaching/sc.pdf&ved=2ahUKEwj-2omDiKSQAxVkif0HHaO0MyQQFnoECB4QAQ&usg=AOvVaw0QpMuFhzGAw0rbC6Qt33T9.

[GS08] Claus Grupen and Boris A. Shwartz. *Particle detectors*. 2. ed. Cambridge monographs on particle physics, nuclear physics, and cosmology. New York, NY: Cambridge University Press, 2008. ISBN: 978-0-521-84006-4. URL: http://www.loc.gov/catdir/enhancements/fy0803/2007036197-d.html.

[KL11] F.G. Kondev and S. Lalkovski. *Nuclear Data Sheets 112, 707*. 2011. URL: https://www.nndc.bnl.gov/nudat3/decaysearchdirect.jsp?nuc=207Bi&unc=NDS.

[PBW12] T. E. Peterson, A. B. Brill, and A. H. Walenta. "High energy gamma-ray imaging using Cherenkov cone detection - A Monte Carlo study with application to a Compton camera system". In: *2012 IEEE Nuclear Science Symposium and Medical Imaging Conference Record (NSS/MIC)*. IEEE, 2012, pp. 3246–3253. ISBN: 978-1-4673-2028-3. DOI: 10.1109/NSSMIC.2012.6551741.

[BT13] E. Browne and J.K. Tuli. *Nuclear Data Sheets 114, 1849*. 2013. URL: https://www.nndc.bnl.gov/nudat3/decaysearchdirect.jsp?nuc=60Co&unc=NDS.

[Sau14] Fabio Sauli. *Gaseous radiation detectors: Fundamentals and applications*. Vol. 36. Cambridge monographs on particle physics, nuclear physics, and cosmology. Cambridge: Cambridge University Press, 2014. ISBN: 978-1-107-04301-5. DOI: 10.1017/CBO9781107337701.

[Arf+15] S. Arfaoui et al. *Characterisation of a Sr-90 based electron monochromator*. Geneva, 2015. URL: https://cds.cern.ch/record/2013995.

[Sha15] M. Shamsuzzoha Basunia. *Nuclear Data Sheets 127, 69*. 2015. URL: https://www.nndc.bnl.gov/nudat3/.

[PR16] Witold Pokorski and Alberto Ribon. *Tracking*. 2016. URL: https://www.google.com/url?sa=i&url=https%3A%2F%2Findico.cern.ch%2Fevent%2F472305%2Fcontribution%2F106%2Fattachments%2F1223729%2F1790331%2FTracking.pdf&psig=AOvVaw3AMRKwcoY90s56YL52r4OJ&ust=1756380303949000&source=images&cd=vfe&opi=89978449&ved=2ahUKEwj1vJDS8KqPAxW1BtsEHawWJ6kQjhx

[Sai16] Saint-Gobain. *BC-400,BC-404,BC-408,BC-412,BC-416: Premium Plastic Scintillators*. 2016. URL: https://www.google.com/url?sa=t&source=web&rct=j&opi=89978449&url=https://www.physics.purdue.edu/~jones105/phys56400_Fall2017/sgc-bc400-404-408-412-416-data-sheet.pdf&ved=2ahUKEwiA4sbS2qWPAxW6hf0HHawiHa8QFnoECBsQAQ&usg=AOvVaw3PpAouEajG7NIxHqUm6N07.

[Yos+17] Y. Yoshihara et al. "Development of electron-tracking Compton imaging system with 30-mm SOI pixel sensor". In: *Journal of Instrumentation* 12.01 (2017), pp. C01045–C01045. DOI: 10.1088/1748-0221/12/01/C01045.

[BM20] S.K. Basu and E.A. Mccutchan. *Nuclear Data Sheets 165, 1*. 2020. URL: https://www.nndc.bnl.gov/nudat3/decaysearchdirect.jsp?nuc=90Y&unc=NDS.

[Bay20] Reimund Bayerlein. *Coincident detection of Cherenkov photons for medical applications*. 2020. DOI: 10.25819/ubsi/4298.

[KW20] Hermann Kolanoski and Norbert Wermes. *Particle detectors: Fundamentals and applications*. New York, NY: Oxford University Press, 2020. ISBN: 978-0-19-885836-2.

[OWI20] OWIS GmbH. *Precision Linear Stages: LTM 80P*. Ed. by OWIS GmbH. 2020. URL: https://www.owis.eu/uploads/tx_aimeos/1.d/files/b/8/b824f069_pi_ltm_80p.pdf.

[SDA20] M. J. Safari, F. Abbasi Davani, and H. Afarideh. "Differentiation method for localization of Compton edge in organic scintillation detectors". In: *Radiation Physics and Engineering* 1.4 (2020), pp. 9–16. DOI: 10.22034/rpe.2020.104839. URL: http://arxiv.org/pdf/1610.09185v2.

[OWI22] OWIS GmbH. *Rotary Measuring Stages: DMT 65*. Ed. by OWIS GmbH. 2022. URL: https://www.owis.eu/uploads/tx_aimeos/1.d/files/9/a/9ae64fdf_pi_dmt_65.pdf.

[Koo23] Kaveh Kooshkjalali. *Design, Construction, and Testing of a Cherenkov Coincidence Detector for Proton Beam Therapy*. Master thesis. Siegen, 2023. URL: https://www.hep.physik.uni-siegen.de/publications/master-theses.

[Gea25] Geant4 collaboration. *Book For Application Developers*. 2025. URL: https://geant4-userdoc.web.cern.ch/UsersGuides/ForApplicationDeveloper/html/index.html.

[Lar25] Lars Maczey. *Hardware Characterisation for the Construction of a Compton Camera Prototype*. Master thesis. Siegen, 2025.

[Ber+] M.J. Berger et al. *ESTAR: Computer Program for Calculating Stopping-Power and Range Tables for Electrons*. URL: https://physics.nist.gov/PhysRefData/Star/Text/ESTAR.html.

[Com] Fast ComTec. *MCA-3 Series / P7882. Multichannel Analyzer / Dual Input Multiscaler, User Manual.*

[Fle] Ivor Fleck. *Beta spectroscopy: Manual for practical exercises*. Siegen.

[Gea] Geant4 collabration. *Geant4: Official webside*. URL: `https://geant4.web.cern.ch/about/`.

[Sie] Universität Siegen. *Liste der Strahlungsquellen und radioaktiven Stoffe / Materialien, interne Liste.*